Universidade de São Paulo
Instituto de Física

Sinais na física além do Modelo Padrão

Gabriela Lima Lichtenstein

Orientador: Prof. Dr. Gustavo Burdman

Tese de doutorado apresentada ao Instituto de Física da Universidade de São Paulo, como requisito parcial para a obtenção do título de Doutora em Ciências.

Banca Examinadora:
Prof. Dr. Gustavo Alberto Burdman - Orientador (Universidade de São Paulo)
Prof. Dr. André P. Lessa (Universidade Federal do ABC)
Prof. Dr. Oscar J. P. Eboli (Universidade de São Paulo)
Prof. Dr. Chee Sheng Fong (Universidade Federal do ABC)
Prof. Dr. Thiago Rafael Fernandez Perez (Instituto de Fisica Teorica/ Universidade Estadual de São Paulo)

São Paulo
2020

FICHA CATALOGRÁFICA
Preparada pelo Serviço de Biblioteca e Informação
do Instituto de Física da Universidade de São Paulo

Lichtenstein, Gabriela Lima

Sinais na Física Além do Modelo Padrão. São Paulo, 2020.

Tese (Doutorado) – Universidade de São Paulo. Instituto de Física. Departamento Física Matemática

Orientador: Prof. Dr. Gustavo Alberto Burdman

Área de Concentração: Fenomenologia de Física de Partículas

Unitermos: 1. Partículas elementares.; 2. LHC.; 3. Matéria escura.

USP/IF/SBI-042/2020

University of São Paulo
Physics Institute

Signals from physics beyond the standard model

Gabriela Lima Lichtenstein

Supervisor: Prof. Dr. Gustavo Burdman

Thesis submitted to the Physics Institute of the University of São Paulo in partial fulfillment of the requirements for the degree of Doctor of Science.

Examining Committee:
Prof. Dr. Gustavo Alberto Burdman - Orientador (Universidade de São Paulo)
Prof. Dr. André P. Lessa (Universidade Federal do ABC)
Prof. Dr. Oscar J. P. Eboli (Universidade de São Paulo)
Prof. Dr. Chee Sheng Fong (Universidade Federal do ABC)
Prof. Dr. Thiago Rafael Fernandez Perez (Instituto de Fisica Teorica/ Universidade Estadual de São Paulo)

São Paulo
2020

Acknowledgments

This study was financed in part by the Coordenação de Aperfeiçoamento de Pessoal de Nível Superior - Brasil (CAPES) - Finance Code 001

Firstly, I thank my supervisor, prof. Gustavo Burdman, for his support and friendship. His advice helped me grow as a scientist and a human being. Besides, I dedicate this thesis to researches and friends at Fermilab. Specifically, I am grateful to dr. Roni Harnik for his fantastic ideas, and dr. Yue Zhang for always patiently sharing his knowledge. I am also thankful for the time shared with prof Eduardo Pontón, who was an example of life perseverance. I thank the Physics institute employees, in specific Simone, Amelia, Cecilia, Marcelo, Paula, Andrea, and Eber.

I also thank my family and friends that I love. Mainly, I dedicate this thesis to Sumaia, who spent 104 years learning something new every day. There is an extensive list of people that were in my heart and influenced me through the doctorate. I thank them all to encouraged me to finish my Ph.D. successfully.. Unfortunately, I can only list some of them. First, my boyfriend Bruno, with his passion for mathematics that inspired me to continue my work. My grandmother Esthela, who is the strongest woman I met. My parents Regina and Flavio, and my brother Paul, I am grateful for their love and support. I thank my three puppies that fill my life with joy. My uncles and cousins, especially Beth, Thais, and Thiago. My companion Leo. I appreciate the sincere friendship from Claudia, Dani, Rosinha, Dilson, Ricardo, Lissa, Wilson, Pietro, Thiago, Zahra, Leila, Sam, Jessica, Carol, Cintia, Sheng, Manju, Cristiano, Pati, Tamara, Riis, Cristian, Lia, and Denise. The people that always give me support: Julieta, Vera, Roberta, and Raquel. The brazucas, who became my dear winter family. My friends and professors from Ciencias Moleculares. I thank all my dancing friends and teachers: "it ain't what you do, it's the way that you do it."

Gabriela Lichtenstein

Abstract

Evidence for new physics may come from different searches, such as collider experiments, cosmological bounds, astrophysical searches, or neutrino detectors. Several open questions motivate them, for example, the hierarchy problem (HP), the particle nature of dark matter (DM), or the inclusion of neutrino masses in the Standard Model (SM). Specifically, the HP motivates searches at the Large Hadron Collider (LHC). This question arises from the severe difference between the electroweak (EW) and the SM ultra-violet (UV) scale Λ_{UV}. The theory sensitivity is observed when calculating the Higgs mass radiative corrections, which diverge quadratically with Λ_{UV}. The presence of a light Higgs boson suggests new physics at the TeV scale or fine-tuning the SM. Although an additional symmetry can alleviate the HP, recent data from the LHC has been putting stringent bounds on theories beyond the SM. The Little Hierarchy Problem (LHP) concerns the sensitivity to the existing energy gap between the EW scale and the LHC reach scale. Hidden sectors address the LHP. Particularly, Neutral Naturalness (NN) is a class of models that presents a hidden $SU(3)$ color group, which does not interact strongly with the SM. Therefore, the light colorless top partner alleviates bounds from the LHC and presents a unique phenomenology. NN has a distinct signature of displaced vertices from colorless glueballs. In the first part of this thesis, we model the distribution of displaced vertices at the LHC from the Folded Supersymmetry scenario, which is a realization of NN. The second part of this thesis concerns DM indirect searches. Although gravitational observations confirm the existence of DM, its particle nature remains an open question. DM indirect searches look for signals of processes where it annihilates into SM particles. Several experiments constraint such models, including telescopes, neutrino, and cosmic-ray detectors. Specifically, x-ray telescopes have been searching for evidence of DM particles in the keV mass range. The most competitive ones, such as CHANDRA or XMM-NEWTON, use charged coupled device (CCD) technology for imaging and spectroscopy. There is a proposal for a new telescope in Earth orbit using an improved version of the detector called skipper CCD. It is advantageous for its extremely low electronic noise. Besides, astrophysical observations require a narrow opening angle. However, a broad field of view would increase the number of events coming from the feeble interaction between DM and light. Therefore, the new x-ray telescope with a skipper CCD and a large opening angle will uniquely search for DM candidates. In this work, we predict the signal from several DM scenarios: sterile neutrino decay, resonant x-ray scattering, axion searches, and mirror stars.

Keywords: beyond the standard model, phenomenology, colorless top partners, dark matter, indirect searches

Resumo

Evidências de nova física podem surgir de experimentos distintos. Por exemplo, na física de colisores, vínculos cosmológicos e astrofísicos ou detectores de neutrinos. Diversas questões em aberto motivam essa procura, como o problema de hierarquia (PH), a natureza da matéria escura (ME) ou na inclusão das massas dos neutrinos no modelo padrão (MP). Notadamente, o PH justifica a procura de nova física no grande colisor de hadrons ("Large Hadron Collider", LHC). Essa questão surge da rigorosa diferença entre a escala eletrofraca e ultra violeta (UV) do MP, denotada por Λ_{UV}. A sensitividade da teoria é observada ao calcular correções radiativas à massa do Higgs, as quais divergem quadraticamente com Λ_{UV}. Logo, a presença de um boson de Higgs leve indica evidência de nova física na escala TeV ou ajuste fino do MP. Apesar de uma simetria adicional aliviar esse problema, dados recentes do LHC têm imposto vínculos rígidos em teorias além do MP. O pequeno problema da hierarquia (PPH) vem da sentividade à diferença existente entre as escalas eletrofraca e a qual opera o LHC. O PPH pode ser referido por teorias com um setor escondido. Especificamente, naturalidade neutra (NN) é uma família de modelos que apresentam um grupo de cor escondido $SU(3)$ que não interage fortemente com o MP. Portanto, o parceiro do quark top sem cor pode ser leve, o qual alivia os vínculos com o LHC e apresenta uma fenomenologia única. NN tem uma assinatura distinta de vértices deslocados vindos de glueballs sem cor. Na primeira parte desta tese, nós modelamos a distribuição de vértices deslocados no LHC vindos de um cenário em Supersimetria Folded, que é uma realização de NN. A segunda parte da tese concerne procuras indireta por Matéria Escura (ME). Apesar de observações gravitacionais confirmarem sua existência de ME, não foi provada sua natureza como partícula elementar. Procuras indireta por ME incluem processos onde a ME se aniquilam em partículas do MP. Diversos experimentos restringem esses modelos, como telescopios, detectores de neutrino ou raios cósmicos. Particularmente, telescópios de raios-X têm procurado por evidências de candidatos à ME com massa na escala keV. Os mais competitivos, como CHANDRA e XMM-NEWTON, usam a tecnologia de charged coupled devices (CCD) para obter imagens e espectroscopia. Existe uma proposta de um novo telescópio na orbita da Terra com uma versão melhorada do detector chamada skipper CCD. Sua vantagem consiste em ruídos eletrônicos extremamente baixos. Além disso, observações astrofísicas requerem um ângulo de abertura estreito. Entretanto, um campo de visão amplo deve aumentar o número de eventos vindos de interações extremamente fracas entre ME e a luz. Portanto, o novo telescópio de raios-X com skipper CCD e um vasto ângulo de abertura irá procurar por ME de uma maneira única. Neste trabalho, nós estudamos os sinais vindo de diversos cenários: decaimentos de neutrinos estéreis, espalhamento ressonante de raios-X, procura por axions e estrelas de matéria espelhada.

Palavras-chave: além do modelo padrão, fenomenologia, parceiros do quark top sem cor, matéria escura, procura indireta.

Publication List

- G. Burdman, N. Fonseca, and G. Lichtenstein, "Resonances from Quiver Theories at the LHC," Phys. Rev., vol. D88, p. 116006, 2013.
- G. Burdman, G. Lichtenstein. "Displaced Vertices from Hidden Glue.", Jul 10, 2018. 18 pp. Published in JHEP 1808 (2018) 146. DOI: 10.1007/JHEP08(2018)146. arXiv:1807.03801 [hep-ph]
- G. Lichtenstein, R. Harnik and Y. Zhang, "In preparation: Evidence for dark matter from X-rays observations using skipper CCDs".

Acronyms

ATLAS	A Toroidal LHC Apparatus
CCD	Charge Couple Device
CDM	Cold Dark Matter
CM	Center of Mass
CMS	Compact Muon Solenoid
DM	Dark Matter
EM	Electromagnetic
EW	Electroweak
F-SUSY	Folded Supersymmetry
FF	Fragmentation Function
FOV	Field of View
GC	Galatic Center
HP	Hierarchy Problem
IR	Infra-red
KK	Kaluza-Klein
L, R	Left, right handed
LHC	Large Hadron Collider
LHCb	LHC-beauty
LHP	Little Hierarchy Problem
LLP	Long Lived Particles
MSSM	Minimal Supersymmetric Standard Model
NFW	Navarro–Frenk–White
NGB	Nambu Goldstones bosons
NN	Neutral Naturalness
PDF	Parton Distribution Function
QCD	Quantum Chromodynamics
SM	Standard Model
SUSY	Supersymmetry
UV	Ultra-violet
VEV	Vacuum Expected Value

Contents

1 Introduction

The standard model (SM) describes the elementary particles and their interactions. It is a quantum field theory that includes the electroweak (EW) and strong interactions. The EW sector is described by the gauge symmetry $SU(2)_L \times U(1)_Y$, which is spontaneously broken into the electromagnetic $U(1)_{EM}$ by the Higgs mechanism. Besides, the color gauge group $SU(3)_C$ describes the strong interactions, which represent the quarks and gluons propagations and interactions.

This thesis concerns the phenomenology of two different experimental searches for new physics beyond the SM. The SM was confirmed experimentally with remarkable precision. However, there are unanswered questions in high energy physics, such as the Hierarchy Problem of scales (HP) and the inclusion of Dark Matter (DM). The first one motivates the first part of the thesis; it consists of an analysis of displaced vertices from a hidden sector at the Large Hadron Collider (LHC). Meanwhile, the second part shows a study of indirect DM detection at a new X-ray telescope.

1.1 The standard model of particle physics

The standard model (SM) of particle physics describes with precision the elementary particles and their interactions. It is described as the gauge symmetries $SU(3)_C \times SU(2)_L \times U(1)_Y$. Moreover, the matter content of the SM has three fermion families among quarks and leptons. Firstly, the color group $SU(3)_C$ gives rise to the strong interactions between quarks and gluons. Meanwhile, the EW sector corresponds to the $SU(2)_L \times U(1)_Y$, which is spontaneously broken into

$U(1)_{EM}$ by the Higgs mechanism. This process dynamically generates the masses of the EW gauge bosons $W^{\pm}$ and Z^0, with a remaining non-massive photon.

1.1.1 Strong interactions

Quantum Chromodynamics (QCD) is derived from the non-abelian gauge theory with a color group $SU(3)_C$. The classical strong interaction Lagrangian describes the dynamics of quarks $q_{a,b}$ and gluons G^a_μ as:

$$\mathcal{L}_{QCD} = -\frac{1}{4}F^a_{\mu\nu}F^{\mu\nu a} + \sum_{Flavours} \bar{q}_a(i\not{D} - m)_{ab}q_b, \tag{1.1}$$

wich is sumed over the flavor indices a and b. The non-abelian tensor field $F^a_{\mu\nu}$ is defined by:

$$F^a_{\mu\nu} = \partial_\mu G^a_\nu - \partial_\nu G^a_\mu - g_S f^{abc} G^b_\mu G^c_\nu, \tag{1.2}$$

where g_S is the strong coupling and f^{abc} is the structure constant, defined by the comutator:

$$if^{abc}T^c = [T^a, T^b], \tag{1.3}$$

where the 8 $SU(3)_C$ generators $T^a = \frac{\lambda^a}{2}$ are represented by Gell-Mann matrices λ^a. Finally, the QCD Lagrangian in equation (1.1) has a covariant derivative $D_m u$, which is defined such that the theory is gauge invariant:

$$D_\mu = \partial_\mu + ig_s G^a_\mu T^a. \tag{1.4}$$

For a complete understanding, one must include gauge fixing and ghost terms to the QCD Lagrangian, which can be found in textbooks, such as references (1; 2).

Strongly charged elementary particles cannot be found free in nature; they are always confined inside hadrons. This behavior is described through radiative corrections. The running coupling $\alpha_S = 4\pi g_S^2$ is measured in a certain energy scale then evolved to higher values of energy. For instance, the strong coupling is well known at the mass of Z boson scale $\alpha_S(M_Z) = 0.1184 \pm 0.001$ (3). Next, it can be estimated to different energy scales μ through the beta funcion:

$$\beta = \frac{d\, g_S}{d\,\mathrm{Log}(\mu)}. \tag{1.5}$$

The one loop QCD corrections the beta function is given by:

$$\beta_{QCD} = -\frac{g_S^3}{4\pi}\left(\frac{11}{3}\,C_2(G) - \frac{4}{3}n_f\,C(r)\right), \tag{1.6}$$

where n_f is the number of fermions in a given a representation r. Besides, $C_2(G)$ is the Casimir operator and C(r) defined by

$$tr[T_r^a T_r^b] = C(r)\delta^{ab}. \tag{1.7}$$

For the SM SU(3) color group, $C_2(G) = 3$ and $C(r) = \frac{1}{2}$. The number of quark flavors corresponds to $n_f = 6$. Moreover, the SM lower infra-red (IR) validity is given by the strongly coupled QCD quantum corrections at low energies, where the color interactions cannot be described perturbatively. Finally, since the QCD beta function negative, the strong coupling g_s has large values at small energies and is asymptotically free for high energies. Therefore, the strong interactions justifies the confinement model of quarks inside hadrons.

1.1.2 Electroweak Interactions

The EW model describes the nature of weak interactions unified in high energies with the electromagnetic interactions. S. L. Glashow in 1961 (4), S. Weinberg in 1967 (5), and A. Salam proposes the EW model. The initial SM Lagrangian does not allow mass terms to the gauge bosons. However, they are experimentally observed at $m_W = 80.379 \pm 0.012$ GeV and $m_Z = 91.1876 \pm 0.0021$ GeV (6). The EW model dynamically generates gauge bosons masses by spontaneous symmetry breaking.

The EW model initially contains the gauge symmetry $SU(2)_L \times U(1)_Y$, where L stands for the chiral left handed representation, and Y is the hypercharge. It simply contains massless gauge bosons A_μ^a of $SU(2)$ and B_μ of $U(1)$. The flavor indices varies as $a = 1, 2, 3$, and the greek indices μ, ν = 0, 1, 2, 3, 4 indicates the time-space metric. Moreover, the model includes a potential $V(\phi^\dagger\phi)$. It describes the complex scalar field ϕ, which transforms as a doublet of $SU(2)$. Finally, the EW Lagrangian is described as:

$$\mathcal{L}_{EW} = (D^\mu\phi)^\dagger(D_\mu\phi) - \frac{1}{4}A_{\mu\nu}^a A^{a\mu\nu} - \frac{1}{4}B_{\mu\nu}B^{\mu\nu} - V(\phi^\dagger\phi). \tag{1.8}$$

The strength field of the gauge bosons corresponds to:

$$A^a_{\mu\nu} = \partial_\mu A^a_\nu - \partial_\nu A^a_\mu . + g f^{abc} A^b_\mu A^c_\nu, \tag{1.9}$$

$$B_{\mu\nu} = \partial_\mu B^a_\nu - \partial_\nu B^a_\mu, \tag{1.10}$$

where g is the coupling. The structure constant f^{abc} is defined by the commutator of the $SU(2)$ group generator t^a as in equation 1.3, which can be represented as Pauli matrices $t^a = \frac{\sigma^a}{2}$. Furthermore, the covariant derivative D^μ is defined such that the theory is gauge invariant:

$$D_\mu \phi = (\partial_\mu - \frac{ig}{3} A^a_\mu \sigma^a - i Y_\phi g' B_\mu)\phi, \tag{1.11}$$

where the couplings g and g' correspond to $SU(2)_L$ and $U(1)_Y$ respectively and Y is the correspondent hypercharge.

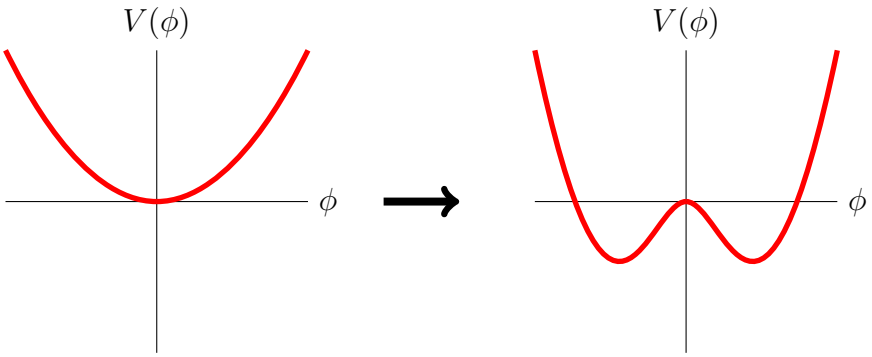

Figure 1.1: Illustration of spontaneous symmetry breaking of a generic quadratic to fourth potential .

The $SU(2)$ symmetry in the EW Lagrangian does not allow mass terms for the gauge bosons. They are going to be dynamically generated by the Higgs mechanism. First, the model includes a spontaneous symmetry breaking. In this case, the potential $V(\phi^\dagger\phi)$ in equation 1.8 is going to change from a quadratic massive potential $V(\phi^\dagger\phi) = m^2\phi^\dagger\phi$ to the quartic potential:

$$V(\phi^\dagger\phi) = -m^2(\phi^\dagger\phi) + \lambda(\phi^\dagger\phi)^2, \tag{1.12}$$

where the mass term also acquires a negative sign. Figure 1.1 illustrates the spontaneous symmetry breaking, where the radial parabula symmetry is promoted to a quartic function, maintaining only a symmetry along the vertical axis.

The gauge boson mass term arises expanding the scalar field around its vacuum expected value (VEV), which is defined by the potential's minimum:

$$\langle\phi\rangle_0 = \pm\frac{m^2}{2\lambda}. \tag{1.13}$$

One possible choice of the VEV is:

$$\langle\phi\rangle = \frac{1}{\sqrt{2}}\begin{pmatrix}0\\v\end{pmatrix}. \tag{1.14}$$

where $v \sim 246$ GeV. Considering the kinetical terms:

$$\Delta\mathcal{L}_{kin} = (D_\mu\phi)^\dagger(D^\mu\phi), \tag{1.15}$$

with the covariant derivative is given in equation 1.11. Therefore, first term of the expansion is:

$$\Delta\mathcal{L} = \frac{1}{2}(0 \quad v)(gA^a_\mu\tau^a + \frac{1}{2}g'B_\mu)(gA^{b\mu}\tau^b + \frac{1}{2}g'B^\mu)\begin{pmatrix}0\\v\end{pmatrix} \tag{1.16}$$

which includes the mass terms for both A^a_μ and B_μ.

$$\Delta\mathcal{L}_{mass} = \frac{1}{2}\frac{v^2}{4}[g^2(A^1_\mu)^2 + g^2(A^2_\mu)^2 + (-gA^3_\mu + g'B_\mu)^2]. \tag{1.17}$$

We can identify the states $A^{1,2}_\mu$ with the charged gauge bosons $W^\pm_\mu$:

$$W^\pm_\mu = \frac{1}{\sqrt{2}}(A^1_\mu \mp iA^2_\mu), \tag{1.18}$$

$$\text{with } m_W = g\frac{v}{2}. \tag{1.19}$$

In order to obtain the neutral Z^0 and photon, it is necessary to rotate A^3_μ e B_μ to the mass eigenstates:

$$\begin{pmatrix}Z^0_\mu\\A_\mu\end{pmatrix} = \begin{pmatrix}\cos\theta_W & -\sin\theta_W\\ \sin\theta_W & \cos\theta_W\end{pmatrix}\begin{pmatrix}A^3_\mu\\B_\mu\end{pmatrix}, \tag{1.20}$$

where the weak mixing angle θ_W is defined by the couplings:

$$\tan\theta = \frac{g'}{g}. \tag{1.21}$$

Finally, the theory presents the massive EW neutral boson:

$$Z_\mu^0 = \frac{1}{\sqrt{g^2+g'^2}}\,(gA_\mu^3 - g'B_\mu), \tag{1.22}$$

$$\text{with } m_Z = \sqrt{g^2+g'^2}\,\frac{v}{2}; \tag{1.23}$$

$$\tag{1.24}$$

and the ortogonal state corresponding to the non-massive photon:

$$A_\mu = \frac{1}{\sqrt{g^2+g'^2}}(g'A_\mu^3 + gB_\mu) \tag{1.25}$$

On the other hand, we only considered the first term of the scalar expansion. The next one is obtained when the four degrees of freedom of $\phi(x_\mu)$ are represented in terms of the complex fields $h(x_\mu)$ and $\theta(x_\mu)$ as:

$$\phi(x_\mu) = \frac{1}{\sqrt{2}}\begin{pmatrix} 0 \\ v + h(x_\mu) \end{pmatrix} e^{i\frac{\theta(x_\mu)}{v}}, \tag{1.26}$$

In this case, the resulting kinetical Lagrangian also generates an off diagonal interaction terms that mixes the gauge fields with a kinematical term of the form $A_\mu\,\partial^\mu\theta(x_\mu)$. However, the gauge fixing can elminate this term. Since the theory is invariant under the gauge transformations:

$$A_\mu \to A_\mu + \frac{1}{gv}\partial_\mu\alpha(x_\mu) \tag{1.27}$$

$$\theta(x_\mu) \to \theta(x_\mu) + f\alpha(x_\mu). \tag{1.28}$$

The choice of the parameters $\alpha(x_\mu)$ and $\theta(x_\mu)$ can fix the gauge and avoid the problem. For instance, the unitary gauge choice states that $\theta(x_\mu) = 0$, leading to a theory with massive EW bosons and one degree of freedom that is identified with the Higgs boson. In this case, the potential is minimized with a VEV as $v^2 = \mu^2/y$ and the Higgs mass defined as $m_H = \sqrt{2y}\,v$.

Furthermore, the fermion masses are also not allowed by the gauge symmetry. They are dynamically generated from Yukawa terms:

$$\mathcal{L}_Y = y\bar{E}_L\,\phi\,e_R + h.c., \tag{1.29}$$

where E_L is the fermion left-handed doublet and e_R is the singlet representation of the right-handed fermion. After EW symmetry breaking,

the fermion masses are obtained as:

$$m_f = \frac{y\,v}{\sqrt{2}}. \tag{1.30}$$

To sum up, the SM of particle physics is described through the EW symmetry breaking $SU(2)_L \times U(1)_Y \to U(1)_{EM}$, and the $SU(3)_C$ strong sector. It contains massless photons and gluons, three massive weak bosons Z^0, $W^{\pm}$, and the Higgs boson. The matter content of the SM includes three families of fermions, divided into quarks and leptons. Section **??** briefly discussed the strong interactions, while section **??** described the EW model, in which the Higgs mechanism generates the mass terms of the gauge bosons and fermions dynamically.

1.2 Beyond the Standard Model

Although the SM agrees precisely with the data, there are several questions it cannot answer. For instance, it does not describe the cosmological constant or includes gravitational interactions. Besides, neutrinos in the SM are not massive, though the neutrino oscillation experiments showed that they must have a mass to allow the flavor mixing (7). There is a significant number of questions that motivate theories Beyond the Standard Model (BSM) and searches for new physics. In specific, this thesis analyses signals from theories BSM motivated by two different questions. The first part concerns the study of solutions to the Little Hierarchy Problem of scales (LHP), while the second part studies Dark Matter (DM) searches.

1.2.1 The Little Hierarchy Problem

The Hierarchy Problem of scales (HP) motivates searches for new physics at TeV scales. This question arises from the sensitivity of the SM from the EW to the ultra-violet (UV). For instance, when calculating radiative corrections to the Higgs mass, it is necessary to include fermionic loops into the Higgs propagator, as shown in the first diagram of figure 1.2. This calculation results in a quadratic dependence with the UV scale Λ_{UV}:

$$\delta m_H^2 = -\sum_{fermions} \frac{N_C\, y_f}{8\pi^2}\,\Lambda_{UV}^2 + O(\mathrm{Log}\,\Lambda_{UV}), \tag{1.31}$$

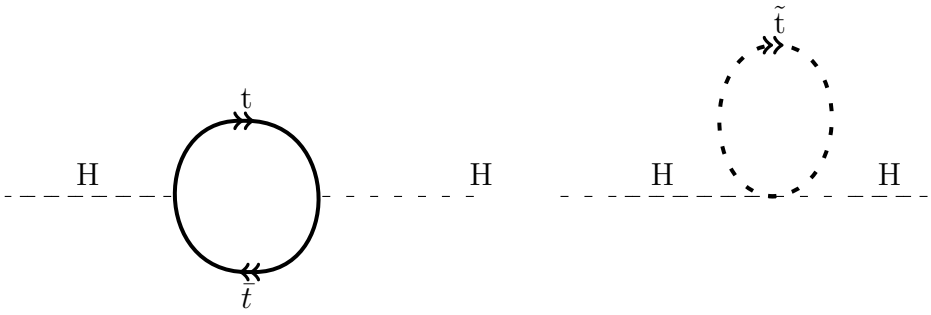

Figure 1.2: The diagram on the left corresponds to radiative corrections to the Higgs mass includes contributions with a fermionic loop to its propagator. The largest contribution comes from the top loop for its high valued Yukawa coupling. On the right, the stop diagram that cancels exactly contributions from the figure on the left, exemplifying how the MSSM solves the HP.

where N_C is the number of colors, and y_f is the Yukawa coupling of each fermion. Since the top quark Yukawa is the largest amongst the fermions, it generates the highest contribution to this calculation. Therefore, we are going to consider now the loop contribution of the top quark to the Higgs mass radiative corrections. Experimentally, the LHC has measured a light Higgs boson with $m_H = 125$ GeV. Therefore, Λ_{UV} should be naturally at the TeV scale to avoid severe fine-tuning. Since the corrections to the scalar field go quadratically to its bare mass, the theory fine-tuning is greater than any other physical parameter ever observed. The infrared (IR) difference to the UV scale may reach 1 part to 10^{34} when considering the difference between the electroweak and Planck scale. The desired new physics scale up to the TeV scale can generate fine tunning of the order 1%, meanwhile pushing the UV limit to 10 TeV drastically aggravates to 1 part of 10^4.

Although the HP motivated the LHC to operate at the TeV scale, experimental data restricted the main theories candidates to solve this question. The existing gap between the EW scale and the LHC operating energy scale may already imply fine-tuning the SM, originating the so-called Little Hierarchy Problem (LHP). For example, the Minimal Supersymmetric Standard Model (MSSM) includes a superpartner to the top quark that allows it to be natural. The new particle is a scalar top, or stop. It generates the diagram in figure 1.2, which cancels exactly the top contribution to the Higgs mass in

equation 1.31. However, bounds from the LHC put the stop mass at large scale. Figure 1.3 shows results from the CMS (Compact Muon Solenoid) collaboration of searches for the stop, which goes up to 1 TeV without any discover (8). Besides, the figure also shows that bounds on gluino masses are even higher, reaching approximately 2 TeV. Even though the direct searches for the stop may still have some light mass parameter space, the radiative corrections to the stop mass include gluino contributions, which have much more strict bounds. Therefore, these results imply in fine tunning the MSSM itself.

1.2.2 Dark Matter Searches

Dark Matter (DM) evidence comes from gravitational observations. However, it is not included in the SM, and its particle nature is yet to be proven. DM presents remarkable characteristics, such as its abundance and the fact that it interacts very feeble with light. In particular, cosmological observations indicate that only around 4% of the total energy of the universe is baryonic. Approximately 20% corresponds to Dark Matter (DM), and Dark Energy constitutes most of the universe. A detailed description of DM evidence and properties can be found in reviews and lectures, such as references (6; 9; 10).

The first reliable evidence of DM was the galaxy rotation curves. Although Fritz Zwicky suggested the name "DM" in 1933, Vera Rubin and Kent Ford's observations in 1978 of galaxy rotations validates the presence of the dark halo in the galaxy (11; 12). Another evidence comes from galaxy clusters observations, such as the Bullet Cluster (1E0657-558) (13). The gravitational potential and weak gravitational lensing provide information to calculate DM abundance and its limited self-interaction (14). However, the most compelling evidence comes from the Cold Dark Matter (CDM) assumption, the ΛCDM paradigm (15). N-body simulations demonstrate how early universe conditions lead to large scale structures today. They conclude that DM cannot be relativistic, which means it is cold or warm, depending on the mean velocity distribution. On the other hand, Modified Newtonian Dynamics (MOND) models are an alternative to DM, where transformations of the gravitational field obtain the physics. However, they are less compelling than ΛCDM models, which have more precise predictions to the Cosmic Microwave Background (CMB)

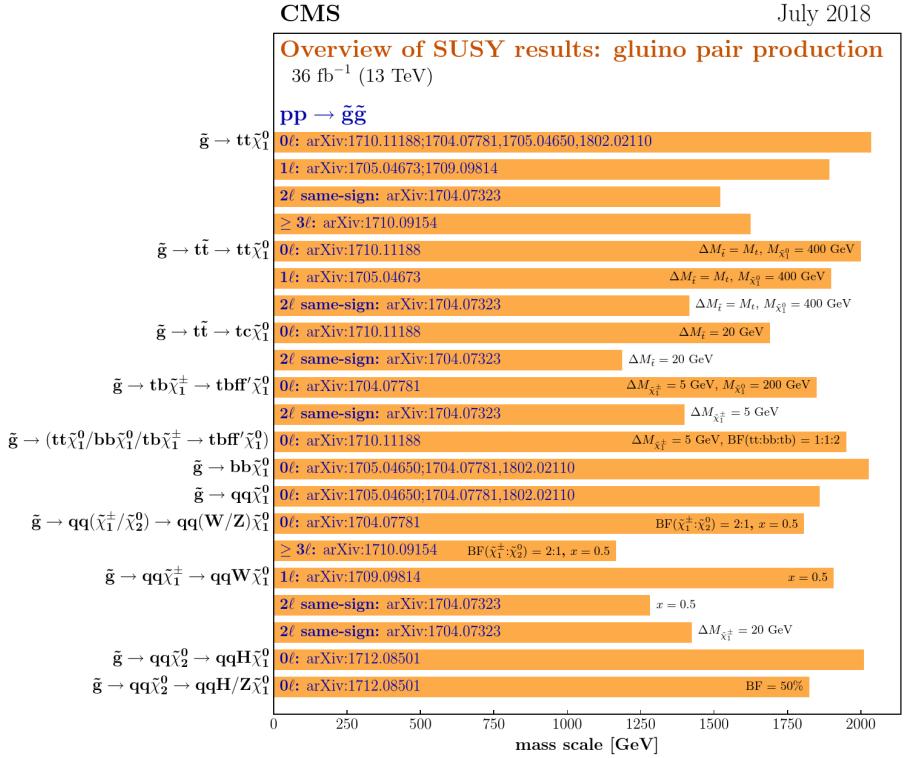

Selection of observed limits at 95% C.L. (theory uncertainties are not included). Probe **up to** the quoted mass limit for light LSPs unless stated otherwise. The quantities ΔM and x represent the absolute mass difference between the primary sparticle and the LSP, and the difference between the intermediate sparticle and the LSP relative to ΔM, respectively, unless indicated otherwise.

(a) Gluino pair production.

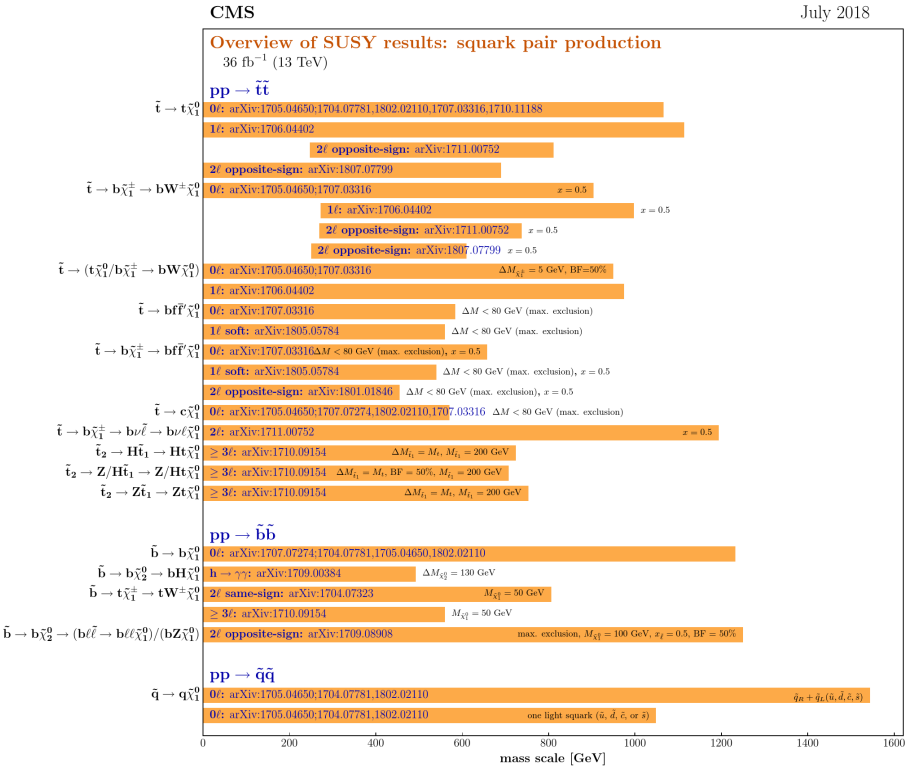

Selection of observed limits at 95% C.L. (theory uncertainties are not included). Probe **up to** the quoted mass limit for light LSPs unless stated otherwise. The quantities ΔM and x represent the absolute mass difference between the primary sparticle and the LSP, and the difference between the intermediate sparticle and the LSP relative to ΔM, respectively, unless indicated otherwise.

(b) Squark pair production.

Figure 1.3: CMS bounds on supersymmetric partners production. Limitis at 95% confidence level. (8)

spectrum and large scale structure data (10).

Cosmological observations provide the properties of Dark Matter: its abundance; it is dark or invisible; it is cold or warm; it is collisionless; it is stable, and it preserves Big Bang Nucleosynthesis (BBN). Firstly, galaxy cluster observations and the galaxy rotation curves show that DM mass density is nearly five times greater than baryonic matter. For instance, Planck Collaboration measurements of the CMB anisotropies shows that DM density $\Omega h^2 = 0.120 \pm 0.001$, and baryonic matter $\Omega_b h^2 = 0.0224 \pm 0.0001$ (16). Secondly, data on the Bullet Cluster put bounds on DM self-interaction using gravitational lensing (9). At last, DM does not severely interact with light; the constraints of its coupling with a photon is $\Gamma_\gamma \leq 1.3 \times 10^{-5}$ at 95% CL (17).

There are several theories with dark matter candidates; they cover a spectrum from 10^{-22} eV to 10 solar masses. For instance, the QCD axion lies typically in the ultralight mass spectrum, between 10^{-12} to 10^{-6} eV, while weakly interactive massive particles (WIMP) are at the GeV until TeV scale. Moreover, primordial black holes can reach ten solar masses and may constitute part of the DM abundance. Baryonic matter is partially an option since massive compact halo objects (MACHOS) can constitute at most 8% of the total dark matter density due to microlensing effect (18; 19; 20).

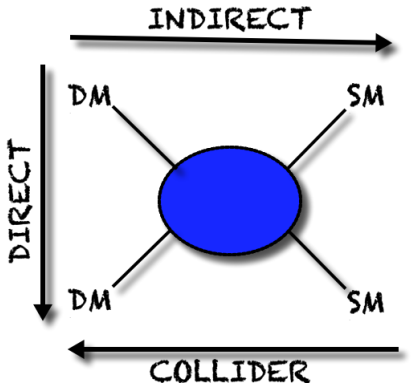

Figure 1.4: DM searches can be divided into three cathegories, represented by the diagram above. From right to left, collider experiments produces the candidates. From top to bottom, the picture shows direct detection DM-SM scattering. At last, from left to right the diagram shows indirect detection, where DM annihilates into SM products.

Numerous experiments probe DM models and search for an elementary particle that justifies its evidence. They include colliders,

neutrino detectors, telescopes, cosmic ray detectors, and cosmological probes. DM searches are divided into three categories, which are represented in Figure 1.4. First, DM can be produced from SM particles at colliders. Then, direct detection searches measure the recoil energy of a nucleus or nucleon interacting with a DM particle. Finally, indirect detection requires DM annihilation. In chapter 4, we are going to study the indirect detection of DM candidates in a new X-ray telescope.

1.3 Searches for new signals

To conclude this chapter, we give a brief description of the research presented in this thesis. It concerns the phenomenology of two different experimental searches for new physics beyond the SM. The first part concerns hidden sector theories as a solution to the LHP, where we model the displaced vertices distribution from a hidden glue at the LHC. The second part focus on DM evidence in a new X-ray telescope.

Firstly, we present the modeling of displaced vertices at the LHC from glueballs charged under a hidden color (21). Neutral Naturalness (NN) refers to a family of models candidates for solving the LHP. They present a new color group that does not interact with the SM. In this case, there are colorless top partners, which can solve the LHP and present a distinct phenomenology. In particular, the production of neutral quarks can generate colorless glueballs, which are invisible hadrons made of gluons of a hidden sector. These can decay back into the SM through highly suppressed interactions with the Higgs. Therefore, the production of colorless quark partners can generate a signal of displaced vertices at the detector, which characterizes uniquely NN models.

Secondly, we analyze distinct DM models and their signals in a new X-ray telescope. Telescopes play an essential role in indirect detection, covering a spectrum from radio to gamma rays. Specifically, X-ray telescopes can probe several DM models with light candidates, typically at the keV scale. The most competitive X-ray telescopes, such as CHANDRA (22) and XMM-NEWTON (23) uses the charged coupled device (CCD) technology for imaging and spectroscopy. A new experiment is proposed using an improved version of this tech-

nology called skipper CCDs (24). It would put a different perspective into DM indirect searches because of its low electronic noise and broad opening angle. The second part of the thesis is an analysis of possible distinct signals from diverse DM scenarios in the new X-ray telescope (25).

This thesis is organized as follows. The first part concerns the model of displaced vertices from a hidden glue in a NN realization called Folded Supersymmetry (F-SUSY). In the second part, we analyze the effect of several DM models in the new X-ray telescope. Chapter 2 describes the NN theoretical aspects, particularly developing an F-SUSY scenario. Next, chapter 3 contains the phenomenology of displaced vertices from colorless glueballs at the LHC. The second part of the thesis is located in chapter 4, where we discuss the advantages of a new X-ray telescope and analyze different scenarios that would produce a significant signal at the detector.

2
Theories with a hidden glue

The first part of the thesis concerns to model the distribution of displaced vertices in theories with a hidden glue (21). We are going to consider the production of top-quark partners from a specific Neutral Naturalness (NN) scenario called Folded Supersymmetry (F-SUSY) (26). The NN models are proposed as a solution to the Little Hierarchy Problem (LHP). They are a class of theories that extend the SM with a new color gauge group and a parity Z_2 symmetry. Each NN realization uses different mechanisms to protect the Higgs mass against radiative corrections. For instance, the F-SUSY scenario includes the presence of colorless top partners, named folded stops or f-stops. They are charged under the new color group, and they escape the strict bounds with the LHC because they are not charged under the SM color.

F-SUSY is a NN model UV completed with Supersymmetry (SUSY) in five dimensions. The daughter model is obtained by breaking SUSY by boundary conditions in a Scherk–Schwarz mechanism (27; 28). The final spectrum is composed of the SM particles plus colorless partners, which have different spin numbers similar to the MSSM. A pair of f-stops can be electrowekly produced at the LHC. In this case, they would annihilate each other into hidden gluons, which hadronizes to colorless long-lived glueballs. Their decay to the SM can happen while still inside the detector, culminating in highly displaced vertices. This chapter contains a theoretical introduction to hidden sectors, developing more specific details in the F-SUSY scenario. Meanwhile, the hidden glue phenomenology is presented in the next chapter.

2.1 Hidden sector

Theories with a hidden sector are presented as a solution to the LHP. They are a class of models that extend the SM with an extra confining group. The new symmetry must protect the Higgs mass against radiative corrections and present a distinct phenomenology, escaping the LHC bounds. We chose to perform this calculation in the Neutral Naturalness (NN) realization named Folded Supersymmetry (F-SUSY). However, the results can be extended to different hidden glue scenarios.

The hidden glue includes numerous theories, among them NN and Hidden Valley models. A generic Hidden Valley (29) scenario includes a non-abelian SU(N) group that does not interact with the SM. On the other hand, NN is a family of models characterized by adding to the SM a copy of the strong group $SU(3)_C$ and a parity Z_2 symmetry that interchanges the hidden and the SM color. The new confining group would have the same properties of QCD, though it does not interact strongly with the SM. Therefore, its spectrum cannot be strongly produced at the LHC, which allows this scenario to escape the experimental bounds. In this case, the LHC can produce relatively light colorless top-quark partners through EW interactions. Several models can describe an NN scenario. The most explored in the literature is the Twin Higgs model (30). This scenario also includes interesting applications in dark matter models (31; 32; 33) while respecting cosmological bounds (34).

In the Twin Higgs scenario, the Higgs is described as a pseudo-Nambu Goldstone boson (pNGB) (30). First, we describe the potential with a global $SU(4)$ as:

$$V(H) = -m^2 H^\dagger H + \lambda (H^\dagger H)^2. \tag{2.1}$$

Similar to the EW symmetry breaking in the SM, the field H acquires a VEV at the potential's minimum $\langle |H| \rangle = m^2/2\lambda = f$, breaking the $SU(4) \to SU(3)$, which generates 7 NGBs. Then, we gauge the subgroup $SU(2)_A \times SU(2)_B$ and describe the field H with two doublets $H = (H_A, H_B)$. Later, we will identify the A and B charges respectively to the SM and hidden symmetry. Finally, the gauge contribution

to the Higgs mass model is:

$$\Delta V(H) = \frac{9g_A^2\Lambda^2}{64\pi^2}H_A^\dagger H_A + \frac{9g_B^2\Lambda^2}{64\pi^2}H_B^\dagger H_B = \frac{9g^2\Lambda^2}{64\pi^2}H^\dagger H, \qquad (2.2)$$

where $g_{A,B}$ is the gauge coupling of each sector. There is also a Z_2 parity that imposes the couplings universality $g = g_A = g_B$, which allows the two sectors to be written as one, which is proportional to $H \dagger H$. Furthermore, the hidden EW bosons masses are generated from the symmetry breaking, $SU(2)_B \times U(1)_B \to U(1)$ through the f VEV. While the SM Higgs is left uneaten, which is identified with the $SU(2)_A$ doublet H_A. To sum up, there are two different scales, where f is the Twin Higgs VEV, and v is the EW VEV. The physics is sensitive to these scales. For instance, the fermion Yukawa coupling and the Higgs decay to the invisible depend on the ratio $\frac{f}{v}$. If $f = v$, the fermionic twin partners would be as light as the SM fermions, and the Higgs decays to the invisible sector could reach up to 50% of its total width. Therefore, for a valid phenomenological model, the Z_2 symmetry must be softly broken, such that $f > v$ (35).

Corrections to the SM Higgs mass now have a contribution from the hidden sector. They can cancel the quadratic divergences, leaving only a logarithm dependence to the top masses in both A and B sectors. Therefore, if the hidden symmetry breaking occurs near the SM EW scale, and the model is valid until just above the LHC operating scale. For example, if $f \sim 800$ GeV, the model UV scale is estimated at $\Lambda \sim 4\pi f \sim 10$ TeV, and the fine-tuning is estimated at 11% (30). Furthermore, different realizations of the TH model are possible, such as the Mirror (30) and fraternal Twin Higgs (36). The former has a dark sector composed of an exact SM copy. Meanwhile, the fraternal scenario contains only the third fermion generation, which is the minimal matter content to avoid HP.

NN models also include the models: Orbifold Higgs (36), Quirky Little Higgs models(37), Minimal NN (38) and Hyperbolic Higgs (39) . First, Orbifold Higgs (36) is a generalization of the Twin Higgs model, where the Higgs is a pNGB in an orbifolded gauge theory. Quirky Little Higgs (37) are derived from Little Higgs models, they can also be presented in compact extradimensional theories. The EW symmetry $SU(2)\times U(1)$ is extended. The global symmetry is broken to $[SU(2) \times U(1)]^2$, describing the SM, and its partners. In the Minimal

NN (38) model, the hidden sector presents vector-like quarks and no gauge fields. It describes the Higgs as a pNGB embedded either on a compact extra dimension or deconstructed scenario (40). At last, the Hyperbolic Higgs (39) is a model UV completed by a supersymmetric theory. The scalar top partner can be entirely neutral to the SM. The portal between the SM and the hidden sector is given by interactions through the Higgs boson, presenting a distinct LHC phenomenology.

2.2 Folded Supersymmetry

In this work, we are going to specifically develop the hidden glue phenomenology in the F-SUSY scenario (26), which is one particular case of NN. This model presents a hidden sector derived from a UV completion with a supersymmetric theory with a compact extra dimension. It is obtained after SUSY breaking by boundary conditions in the Scherck-Schwarz mechanism. The UV supersymmetric theory has the same matter content of an $N = 2$ SUSY, which corresponds to twice the number of flavor indices of quarks and squarks. After SUSY breaking, the boundary conditions are chosen, such that half of the spectrum zero modes are eliminated in the low energy theory. It results in accidental SUSY, which presents only SM particles and hidden partners with different spin and color. The F-SUSY model enjoys of bifold protection. It solves the HP in a similar way of the MSSM since the model preserves characteristics from the SUSY at the UV. However, the scalar top partners can be relatively light because they are charged only under the hidden $SU(3)$. Moreover, quantum corrections imply that the UV SUSY must be restored above the LHC operating scale, approximately at 10 TeV.

2.2.1 Bifold Protection

The F-SUSY model enjoys bifold protection, which is obtained when breaking the UV SUSY theory by boundary conditions. This mechanism will be fully explained in the next section. First, we introduce the bifold protection with a toy model. It will illustrate how to obtain the accidental supersymmetric spectrum. Firstly, the simplified model assumes a theory with global U(N), containing a scalar singlet S that couples with quarks Q in the fundamental representation of U(N) with

the potential:

$$W = \lambda S \bar{Q}_i Q_i, \tag{2.3}$$

where $i = 1 \dots N$ is the flavor indices. In this case, the singlet mass squared m_S^2 is not protected against divergencies from radiative corrections, similar to the HP. Therefore, this problem can be avoided when assuming this model to be supersymmetric. In this case, W is promoted to a superpotential and Q to a chiral superfield. It represents both quarks (q) and their scalar partners' squarks ($\tilde{\text{q}}$). However, the goal of this toy model is to obtain a non-supersymmetric theory and still maintain the singlet mass protected.

The first step in a bifold protection mechanism is to duplicate the number of flavors, resulting in the global symmetry U(2N). Therefore, the spectrum contains the initial quarks and superpartners, denoted by $(q_i, \tilde{q_i})$, with $i = 1, \dots, N$; plus a complete copy of the same set $(q_j, \tilde{q_j})$, with $j = N+1, \dots, 2N$. Moreover, we impose a parity symmetry composed by Z_{2R} and $Z_{2\Gamma}$. The Z_{2R} transformation depends on the spin of each field. Its eigenvalues are ± 1, being odd for fermions and even for bosons. Meanwhile, the $Z_{2\Gamma}$ parity is described by a diagonal matrix:

$$\Gamma_m = \begin{bmatrix} -1 & & & & & \\ & \ddots & & & & \\ & & -1 & & & \\ & & & +1 & & \\ & & & & \ddots & \\ & & & & & -1 \end{bmatrix}. \tag{2.4}$$

Besides, the theory is invariant under the transformations:

$$S \to S, \tag{2.5}$$

$$Q_i \to \Gamma_m Q_i, \tag{2.6}$$

$$\bar{Q}_i \to \Gamma_m^* \bar{Q}_i. \tag{2.7}$$

Therefore, this parity transformation will transform the $2N$ quark flavors with a negative eigenvalue -1 for the first N components, and positive eigenvalue $+1$ for the $N+1$ until $2N$ positions. For instance,

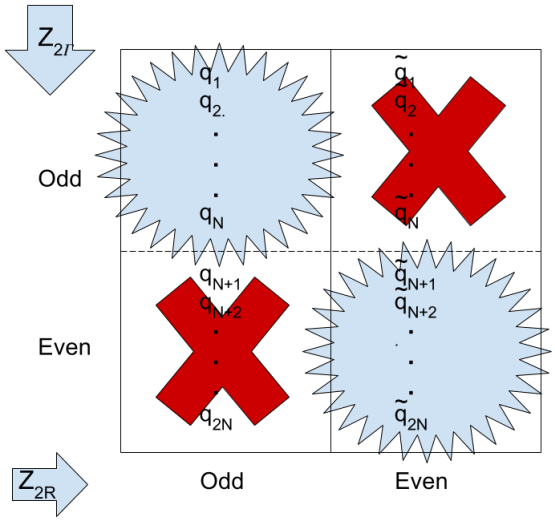

Figure 2.1: Scheme showing the accidentally supersymmetric spectrum. First, the theory presents two sets of quarks and squarks, represented in the table above. The parity under $Z_{2\Gamma}$ is written in the vertical line, at left to the table. While the Z_{2R} parity is just below it. We project out the odd states under the product $Z_{2\Gamma} \times Z_{2R}$, represented by the red cross. Only the even states are kept, which are surrounded by the blue balloon. We observe that despite the final spectrum is similar to SUSY, the flavor numbers of the partners are different, resulting in the accidental SUSY.

this can be visualized in the matrix form of the second line:

$$\begin{bmatrix} q_1 \\ \dots \\ q_N \\ q_{N+1} \\ \dots \\ q_{2N} \end{bmatrix} \rightarrow \Gamma_m = \begin{bmatrix} -1 & & & & & \\ & \ddots & & & & \\ & & -1 & & & \\ & & & +1 & & \\ & & & & \ddots & \\ & & & & & -1 \end{bmatrix} \cdot \begin{bmatrix} q_1 \\ \dots \\ q_N \\ q_{N+1} \\ \dots \\ q_{2N} \end{bmatrix} = \begin{bmatrix} -q_1 \\ \dots \\ -q_N \\ +q_{N+1} \\ \dots \\ +q_{2N} \end{bmatrix} \tag{2.8}$$

Figure 2.1 illustrates how the bifold mechanism achieves an accidentally supersymmetric spectrum. Half of the entire spectrum is eliminated when projecting the $U(2N)$ chiral states over the full parity $Z_{2R} \times Z_{2\Gamma}$. The first N fermionic fields are odd under each of the discrete symmetries. Therefore, they are invariant under the product of both parities. Although the second half of the fermion spectrum is also odd under Z_{2R}, it is even under Z_2, therefore, odd under the

total symmetry. Thus the remaining set of fermions is projected out because it not invariant under $Z_{2R} \times Z_{2\Gamma}$. Analogously, the second half of the bosonic fields will remain in the spectrum, and the first half is projected out. As result, we obtain the accidental SUSY composed of fermions $(q_1, \ldots, q_N)$ and scalars $(\tilde{q}_{N+1}, \ldots, \tilde{q}_{2N})$. The quarks and squarks are not superpartners because the flavor indices do not match. However, they still protect the singlet m_S^2.

Summing up, the bifold protection guaranties that m_S has no quadratic divergences from a fermionic loop at low energies. We assumed a supersymmetric U(2N) theory, describing the superpotential in equation 2.3. It represents the interaction of the singlet S with the chiral Q. Then we impose the $Z_{2R} \times Z_{2\Gamma}$ parity and project out the odd states under the product, generating the accidental SUSY.

Finally, the singlet is protected in one loop by a non-supersymmetric theory. However, the singlet mass is not protected at two loops, and quadratic divergences reappear. Besides, the radiative correction to the squarks masses squared is quadratically divergent with the UV cut-off scale. Therefore we must restore SUSY at Λ_{UV} not too far above the TeV scale. When analyzing this effect in NN models, typically $\Lambda_{UV} = 5$ to 15 TeV is enough to escape the LHC bounds without fine tunning the theory. The next section describes the F-SUSY model, using an analogous the bifold protection method.

2.2.2 The Scherk–Schwarz mechanism

F-SUSY extends the SM with a new color group. The hidden sector spectrum is similar to the supersymmetric partners of the SM, though they are charged under the additional $SU(3)$ instead of the usual strong interaction. The model is obtained from SUSY in a compact extra dimension, which is broken by boundary conditions in the Scherk–Schwarz mechanism (27; 28).

Firstly, we describe the compactification of the extra dimension in the five-dimensional space $(\vec{x}, y)$. The fifth y dimension is described in an orbifold of symmetry S/Z_2. The orbifold topology is obtained by reducing a circle of symmetry S with a Z_2 parity. Figure 2.2 shows the compactification process. The circle with radius R is reduced to a segment of length $L = \pi R$. Besides, the Z_2 parity identifies every point of the upper hemisphere with its opposite on the lower part. The

orbifold is characterized by two fixed points at $y = 0$ and $y = \pi R$, and the periodicity $f(y) = f(y + \pi R)$. Each superfield is described in the 5D Lagrangian. When integrating out the extra dimension, we impose the periodicity and the field equation of motion. The resulting wave functions correspond to tower of Kaluza-Klein (KK) modes, where each state mass increases with $1/R$ (41; 42).

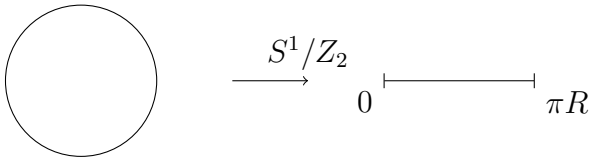

Figure 2.2: The orbifolding mechanism. The circle symmetry S is reduced to a segment by a parity Z_2 symmetry. The Z_2 identifies every point of the upper hemisphere with the opposite one in the lower one. The final orbifold is a segment of size πR with two fixed points at the edges.

The F-SUSY models can be UV completed with an extradimensional supersymmetric theory. The minimum N=1 extradimensional matter content in 5D corresponds to the N=2 spectrum in four dimensions. Therefore, we are going to describe the N=1 five-dimensional physics as an N=2 four-dimensional spectrum in each of the orbifold's points. The appendix A presents details on SUSY and the N=2 matter content. For now, it suffices to remind that the supersymmetric algebra is an extension of the Poincaré group. It is described by charged operators Q_S and $Q_S^\dagger$ that interchange the fermionic or bosonic degrees of freedom. For example, the MSSM spectrum can be constructed from a single N=1 Q charge. However, it is possible to extend the theory up to the N=4. Moreover, the N=1 SUSY has a global $U(1)_R$ connecting each state to its superpartners. Meanwhile, the N=2 case extends the global symmetry to $SU(2)_R$, and the matter content can be represented as a doublet. Figure 2.3 shows the UV theory matter content with N=2 SUSY in the bulk and N=1 in the fixed points. Furthermore, the positions of the orbifold are connected by a $SU(2)_R$ rotation.

The Scherk-Schwarz mechanism breaks SUSY by choosing different N=1 SUSY in the two fixed points. Besides, the $SU(2)_R$ parameter is chosen to break SUSY fully, and the boundary conditions select the desired spectrum in a similar way to the previous bifold example. The spectrum selection depends on the wave function transformation

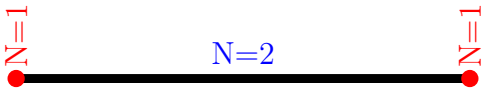

Figure 2.3: The supersymmetric theory with an extra dimension has the same matter content of N=2 SUSY. The spectrum in the orbifold's bulk corresponds to an N=2 theory. However, boundary conditions are chosen such that each fixed point will be a different N=1, which will break SUSY.

properties under reflections about the fixed points $y = 0$ and $y = \pi R$, which respectively correspond to the parity Z and Z'. Each of these transformations will act on the parity character of each particle wave-function $\Phi(y)$:

$$Z[\Phi(y)] = Z\Phi(-y), \tag{2.9}$$

$$Z'[\Phi(y - \pi R)] = Z'\Phi(-y + \pi R). \tag{2.10}$$

We choose the $SU(2)_R$ and different SUSY theories in each fixed point to break the SUSY. Therefore, the zero-mode states that are odd under the product $Z \times Z'$ will be projected out, analogously to the previous example in figure 2.1.

As argued before, instead of describing the N=1 SUSY in 5D, we will use the 4D N=2 language, which describes the same matter content. The super quark hypermultiplet $\hat{\mathrm{Q}}$ is composed of fermions q, q^c, and bosons superpartners $\tilde{q}$, $\tilde{q}^c$. It can be decomposed as $\hat{\mathrm{Q}}= (Q, Q^c)$ eingenstates of Z, where the chiral superfields $Q = (q, \tilde{q})$ and $Q^c = (q^c, \tilde{q}^c)$. Meanwhile, eingenstates of Z' are written as $Q' = (q', \tilde{q}')$ and $Q'^c = (q'^c, \tilde{q}^{c\prime})$. Both decompositions of the hypermultiplet $\hat{\mathrm{Q}}$ are linked by a general $SU(2)_R$ rotation:

$$\begin{bmatrix} q' \\ (q'^c)^\dagger \end{bmatrix} = e^{i\alpha\sigma_2} \begin{bmatrix} q \\ (q^c)^\dagger \end{bmatrix}. \tag{2.11}$$

The angle choice $\alpha = \pi/2$ corresponds to the maximum twist (43), which selects the symmetry where quarks and scalar partners zero modes have different flavor indices.

To sum up, the F-SUSY can be obtained through the UV completion. The high energy model is supersymmetric in an extra dimension with a $SU(2N)$ gauge group. The Scherk–Schwarz mechanism breaks the SUSY by choosing different boundary conditions for each field in the orbifold's fixed points. The minimal daughter theory must have an

extended color group $SU(3)_{SM} \times SU(3)_{hidden} \times Z_2$ and an accidentally supersymmetric spectrum of quarks and colorless f-squarks. However, a more complex F-SUSY model can be built. For example, it can be obtained by the symmetry breaking $SU(6) \to SU(3) \times SU(3) \times U(1)$ using suitable boundary conditions (26).

2.2.3 Folded Supersymmetry as an extension of the SM

A realistic F-SUSY model can be built as an extension of the SM. The final theory contains the extended color sector $SU(3)_A \times SU(3)_B \times Z_2$. Assuming that the SM color comes from the A group $SU(3)_{SM} \equiv SU(3)_A$ and the hidden color from the extra group $SU(3)_B$, the final spectrum must contain the SM quarks q_A, u_A and colorless squarks $\tilde{q}_B$, $\tilde{u}_B$. The same boundary condition assures the presence of hidden gluons after SUSY breaking. The most straightforward gauge theory is $[SU(3)_A \times SU(3)_B \times Z_2^{AB}] \times SU(2)_L \times U(1)_Y$, describing the SM symmetry plus the extended color sector and a parity Z_2^{AB} interchanging the vector superfields of the two $SU(3)$ gauge groups. We will only discuss the color extension because the EW gauge sector will not change under the Z_2^{AB} parity. As discussed in the previous section, the theory is UV completed with a supersymmetric model in a compact extra dimension. The SUSY is broken by boundary conditions, which select only half of the spectrum, which contains the SM quarks and the colorless f-squark.

The bulk hypermultiplets are composed of chiral superfields, which contain quarks and their scalar partners:

$$\hat{\mathrm{Q}}_{iA}(3,1,2,1/6), \quad \hat{\mathrm{Q}}_{iB}(1,3,2,1/6) \tag{2.12}$$

$$\hat{\mathrm{U}}_{iA}(\bar{3},1,1,-2/3), \quad \hat{\mathrm{U}}_{iB}(1,\bar{3},1,-2//3) \tag{2.13}$$

$$\hat{\mathrm{D}}_{iA}(\bar{3},1,1,1/3), \quad \hat{\mathrm{Q}}_{iB}(1,\bar{3},1,1/3), \tag{2.14}$$

where the index $i = 1,2,3$ is for the 3 generations, and all the particles are charged under the minimal F-SUSY symmetry $[SU(3)_A \times SU(3)_B \times Z_2^{AB}] \times SU(2)_L \times U(1)_Y$. Besides, the leptons will arise from :

$$\hat{\mathrm{L}}_{iA}(1,1,2,-1/2), \quad \hat{\mathrm{L}}_{iB}(1,1,2,-1/2) \tag{2.15}$$

$$\hat{\mathrm{E}}_{iA}(1,1,1,1), \quad \hat{\mathrm{E}}_{iB}(1,1,1,1) \tag{2.16}$$

The choice of boundary conditions must be made to obtain the acidental SUSY spectrum. The $N = 1$ superfields $\hat{\mathrm{Q}}_{iA}$ are decomposed

as (Q_{iA}, Q^c_{iA}) or (Q'_{iA}, Q'^c_{iA}). The boundary conditions are chosen, such that Q_{iA} is even, and Q^c_{iA} is odd under the $Z \times Z'$ transformation. In addition, Q'_{iA} is even and Q'^c_{iA} is odd under Z'. These conditions effectively project out the scalar zero modes, leaving only the fermions. An analogous process occurs to $\hat{\mathrm{U}}_{iA}$, $\hat{\mathrm{D}}_{iA}$, $\hat{\mathrm{L}}_{iA}$ and $\hat{\mathrm{E}}_{iA}$. On the other hand, superfields $\hat{\mathrm{Q}}_{iB}$ present different boundary conditions such that Q_{iB} is even, and Q^c_{iB} is odd under Z. Besides, Q'_{iB} is odd and Q'^c_{iB} is even under Z'. This project out the fermions zero modes, and only scalars remain. This conditions are also chosen for the fields $\hat{\mathrm{U}}_{iB}$, $\hat{\mathrm{D}}_{iB}$, $\hat{\mathrm{L}}_{iB}$ and $\hat{\mathrm{E}}_{iB}$.

Furthermore, the minimal F-SUSY model solves the LHP, with a Yukawa potential similar to the MSSM. In the UV completion, the Higgs is extended to two doublets H_U and H_D. Considering the Yukawa superpotential between the Higgs superfield H_U and the third generation quarks takes the form:

$$W = \delta(y)\lambda_t[Q_{3A}H_U U_{3A} + Q_{3B}H_U U_{3B}], \tag{2.17}$$

where δ is the Dirac distribution function, which localizes the Higgs in $y = 0$. The Higgs $H_U = (h_u, \tilde{h}_u)$ transforms with the Z parity such that only h_u remains in the theory. The superpotential in equation 2.17 is invariant under Z_2^{AB}. On the other hand, the two Higgs doublets are localized at $y = 0$, and the boundary condition at $y = \pi R$ does not respect the Z_2^{AB}. This localization guarantees the cancellation of quadratic divergences at one loop. The low energy potential after SUSY breaking is given by:

$$\mathcal{L}_Y = (\lambda_t h_u q_A u_A + h.c.) + \lambda_t^2|\tilde{\mathrm{q}}_B h_u|^2 + \lambda_t^2|\tilde{\mathrm{u}}_B h_u|^2. \tag{2.18}$$

This potential has the same form as the Yukawa terms in the MSSM, which ensures that the Higgs mass does not present quadratic divergencies in radiative corrections at one loop. However, the top partners cannot be strongly produced since they are charged under the hidden color, escaping the strict bounds with the LHC.

However, the F-SUSY model is valid up to a relatively low Λ_{UV} scale. Although the Higgs enjoys bifold protection at one loop, the scalar masses of stops are not protected and diverge at one loop. Thus, the Higgs mass is not protected at two loops, and the radiative cor-

rections to the Higgs mass squared is:

$$\delta m_H^2 = -\frac{3\lambda_t}{4\pi^2}\tilde{m}_t^2 \mathrm{Log}\frac{1}{R\tilde{m}_t}, \tag{2.19}$$

where the top coupling $\lambda_t \sim 1$, $\tilde{m}_t$ is the folded stop mass and R is the size of the orbifod. The UV cutoff Λ_{UV} can be estimated as $1/R$. The fine tuning considering the Higgs mass sensitivity to the top contributions can be calculated as

$$FT = \frac{m_H^2}{2\delta m_H^2} 100\% \tag{2.20}$$

which implies that Λ_{UV} should be from 5 to 15 TeV. For instance, for $\tilde{m}_t = 800$ GeV and $\Lambda_{UV} = 5$ TeV the fine tuning is estimated as 9%, and for $\tilde{m}_t = 500$ GeV and $\Lambda_{UV} = 15$ TeV the fine tuning is 12%. Therefore, the UV-cutoff of this theory must be relatively low, and SUSY must be restored at 5 to 10 TeV scale.

2.2.4 F-squark masses

In the next chapter, we are going to study the f-squark production at the LHC. We have argued that the f-squarks cannot interact strongly with the SM, which allows them to be relatively light. However, they can be electroweakly produced, generating a distinct signal at the collider of highly displaced vertices. At last, to understand the f-squark phenomenology, we first show in this section how to estimate their masses.

In the MSSM. squark masses are zero if SUSY is exact. However, in the compact extra dimension, each fermionic field generates a KK tower of excited states. When breaking SUSY by the Scherk–Schwarz mechanism, the f-squarks gain soft masses generated by loop contributions from a sum over KK modes. However, only propagators passing through both fixed points $y = 0$ and $y = \pi R$ contribute to m_Q^2. We can use the result from references (44) and (45), which considered SUSY breaking in extradimension theories. The f-squark masses are

estimated at 1 loop as:

$$
\begin{aligned}
m_Q^2 &= K\frac{1}{4\pi^4}\left(\frac{4}{3}g_3^2+\frac{3}{4}g_2^2+\frac{1}{36}g_1^2\right)\frac{1}{R^2} \\
m_U^2 &= K\frac{1}{4\pi^4}\left(\frac{4}{3}g_3^2+\frac{4}{9}g_1^2\right)\frac{1}{R^2} \\
m_D^2 &= K\frac{1}{4\pi^4}\left(\frac{4}{3}g_3^2+\frac{1}{9}g_1^2\right)\frac{1}{R^2} \\
m_L^2 &= K\frac{1}{4\pi^4}\left(\frac{3}{4}g_2^2+\frac{1}{4}g_1^2\right)\frac{1}{R^2} \\
m_E^2 &= K\frac{1}{4\pi^4}g_1^2\frac{1}{R^2},
\end{aligned}
\tag{2.21}
$$

where K is a dimensionless constant $K \simeq 2.1$, R is the radius of the orbifold and g_3, g_2 and g_1 are the couplings of $SU(3)$, $SU(2)_L$ and $U(1)_Y$. The soft masses are finite and inversely proportional to the extra dimension length R as $m_Q^2 \propto \frac{1}{R}$. Therefore, we may estimate these masses to range from the GeV scale until $\lesssim 5$ TeV. Moreover, the third generation has corrections to the squark masses from the Yukawa potential. The first and second-generation have much smaller Yukawa couplings, so their contribution will not affect the mass calculations. This contribution is calculated in reference (26), which demonstrates that the third generation masses must include:

$$
\begin{aligned}
m_{3Q}^2 &= K\frac{y_t^2}{8\pi^4}\frac{1}{R^2}, \\
m_{3U}^2 &= K\frac{y_t^2}{4\pi^4}\frac{1}{R^2}
\end{aligned}
\tag{2.22}
$$

3

Distribution of Displaced Vertices from hidden glue

Hidden sectors were presented as a solution to the LHP. Theories with a hidden glue protect the Higgs mass against radiative corrections while escaping bounds with LHC. The hidden glue collider phenomenology is extensive, including processes such as Higgs portals or excited Z' states (46; 29). In particular, we are going to study the electroweak (EW) production of f-squarks (26). The f-squarks can either be produced in a charged or neutral current channel. The first has a resonant $W\gamma$ signal, putting bounds on f-squarks masses. While displaced vertices or a significant fraction of missing energy characterize the production through neutral currents. If a pair of f-squarks is produced, they will annihilate promptly into folded gluons, which in turn hadronize to hidden glueballs. These are pure glue objects, which do not leave a trace at the detector since they are charged under the hidden confining group. However, the hidden glueballs can decay back into the SM through a higher-dimension operator involving the Higgs. Then the lifetime can be estimated, potentially resulting in highly displaced vertices. We will model the FF that provides information on the average multiplicity of glueballs. Using this, we calculate the distribution of displaced vertices (21) at the LHC. Although we performed this calculation in the Folded Supersymmetry (F-SUSY) model, this signature characterizes different hidden glue scenarios (46), and the result can be extended to other hidden sector models.

3.1 F-squark production at the LHC

In the F-SUSY scenario, the f-squarks are charged under the SM EW gauge group. In this case, they can be directly produced at the LHC from charged $W^{\pm}$ or neutral Z, γ currents. In QCD, if a pair of heavy quarks are produced, then the string between them would break when approaching the confinement scale, allowing new pairs of quarks to be formed. Each of them hadronizes and produce each a jet signal in the detector. However, the hidden sector does not present the soft hadronization mechanism because there are no hidden light f-squarks with masses comparable with its confining IR scale Λ_{IR}, which is of order few GeV, as will be discussed in section 3.1.2. Therefore, f-squark production can form bound states that have an extremely short lifetime compared to the collider time. Therefore, f-squarks can promptly produce the lightest states of hidden mesons or glueballs, which are invisible to the detector. However, they can decay to the SM, generating different signals. The charged current f-squark production generates $W\gamma$ resonance, while the other channel has the signature of highly displaced vertices or large fraction missing energy (47).

First, let us consider the production of a $\tilde{u}$ and a $\tilde{d}$ through an s-channel W. The hidden sector dynamics will be similar to QCD, although they are independent of each other. To differentiate it from the SM color sector, we use the name quirky dynamics (48). A quirky string bounds the pair and forms an excited state, similar to QCD. This new state softly radiates and promptly hadronizes to a scalar meson. It cannot decay into hidden glueballs because its ground state is electrically charged. The hidden meson promptly decays to W (49), forming a $W\gamma$ resonance signature. The current limit from ATLAS searches at 8 TeV(50) restrain the f-squark masses at 320, 445, 465 GeV assuming the production of 1, 2, and 3 f-squark generations respectively (51). Besides, reference (52) shows the sensitivity to f-squarks masses at the LHC Run 2. Although $W\gamma$ new resonances are a significant search, it is evidence for numerous other scenarios in BSM physics. Meanwhile, the neutral currents production of a pair of f-squarks potentially culminates in highly displaced vertices, which characterizes uniquely hidden sector models.

The diagram in figure 3.1 shows the neutral current production of

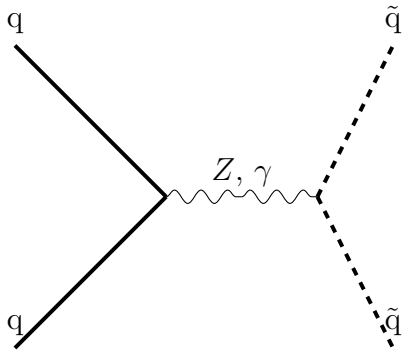

Figure 3.1: Feynman diagram of two SM quarks producing a pair of f-squarks through neutrally charged currents.

f-squarks from SM quarks $q + q \rightarrow (Z \text{ or } \gamma) \rightarrow \tilde{q}\,\tilde{\bar{q}}$. The partonic cross section can be convoluted with a parton distribution function (PDF) to obtain the process from the initial proton collision $p + p \rightarrow (Z \text{ or } \gamma) \rightarrow \tilde{q}\,\tilde{\bar{q}}$. Figure 3.2 shows the resulting cross-section, which is calculated using FeynRules and Madgraph with the center of mass energy at 13 TeV. In section 2.2.4, we estimated the f-squark masses and concluded that the left ones are heavier than the right-handed f-squarks. In the cross section calculation, we have included only the light right-handed squarks, which have approximately the same mass:

$$m_{\tilde{u_R}} = m_{\tilde{d_R}} = m_{\tilde{c_R}} = m_{\tilde{s_R}} = m_{\tilde{b_R}}. \tag{3.1}$$

We excluded the heavier states right handed f-stop and all the left handed squarkes. The latter have the contribution from $SU(2)_L$, as shown in the equation describing $m_{\tilde{q}_L}$ in the set of equations in 2.22. While the third familiy has the additional contribution from its Yukawa interaction, shown in the two equations in 2.23.

The pair of f-squarks cannot go far apart from each other because the QCD' splitting is exponentially suppressed by $e^{-m_q^2/\Lambda_{IR}^2}$. Therefore, the only possibility for them is to go back into a bound state called squirkonium. The squirkonium would softly radiate photons and hidden gluons until the f-squarks annihilate each other into a pair of hard hidden gluons, which hadronizes to folded glueballs. This process would happen promptly in collider time. According to reference

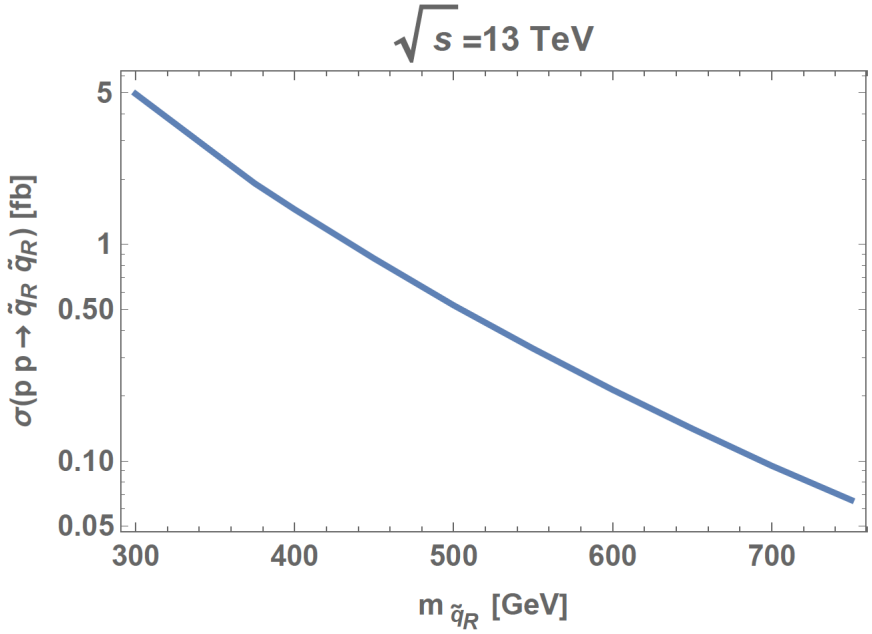

Figure 3.2: Cross Section of a pair of f-squarks production at the LHC at 13 TeV center of mass energy.

(47), the time scale for photon radiation is given by:

$$t_{Rad} \sim \frac{3}{8\pi\,\alpha_F}\frac{m_{\tilde{q}}^3}{\Lambda_{IR}^4}, \tag{3.2}$$

which is order 10^{-18} seconds for a strong hidden coupling of $\alpha_F \sim 0.08$, $\Lambda_{IR} \sim 5$ GeV and $m_{\tilde{q}} \sim 800$ GeV. Therefore, we are going to consider the production of a pair of f-squarks to decay promptly to hard hidden gluons, which in turn will hadronize to folded glueballs.

3.1.1 Glueball lifetime

Glueballs are pure glue objects predicted by QCD. However, they were never observed experimentally because of the presence of light quarks, which hadronize to different states that mix with the glueballs. In F-SUSY, the f-squarks are too heavy for this contamination to take place, allowing the existence of pure glueballs. After the production of f-squarks at the collider, the lightest state for the hidden gluons to hadronize are a 0^{++} glueballs, which are invisible to the detector. However, they can decay back into the SM (46) through a dimension-6 operator mediated by the Higgs. If this process occurs while still inside the detector, it generates highly displaced vertices. We are

going to calculate the glueball lifetime to estimate the typical decay length in an F-SUSY scenario. The hidden glueballs decay to the SM also includes d=4 operators involving gauge bosons and $0^{\pm+}$ and $2^{\pm+}$ states. However, the electroweak bosons decays are significant only if the colorless top partners are lighter than the SM top quarks. A full study of the hidden glueballs states and decays can be found in reference (53).

Glueballs decay back into SM particles through the SM-like Higgs doublet H portal (46; 54). In QCD, the visible gluons couple to the Higgs through a top loop. Analogously, the hidden gluons can also couple to H through a top partner loop, as long as $m_{\tilde{t}} >> m_H$. This interaction is described by the effective dimension six operator:

$$\delta\mathcal{L}^{(6)} = \frac{\alpha_F}{3\pi}\frac{y^2}{M^2}|H|^2\tilde{G}_{\mu\nu}\tilde{G}^{\mu\nu} \tag{3.3}$$

$$= \frac{\alpha_F}{3\pi}\frac{y^2}{M^2}vh\tilde{G}_{\mu\nu}\tilde{G}^{\mu\nu}, \tag{3.4}$$

where H is the SM Higgs doublet, $\tilde{G}_{\mu\nu}$ is the hidden gluon field strength and α_F the folded coupling, which is estimated in 3.1.2. The second line represents the VEV v and the Higgs field h after EW symmetry breaking $H \to (0,\ (v+h)/\sqrt{2})^T$. The coupling $\frac{y^2}{M^2}$ is model dependent, which can be calculated for different NN models (46).

The coefficient $\frac{y^2}{M^2}$ in the F-SUSY scenario is analougous to the MSSM calculation in reference (55). Considering a theory with two scalar top partners $\tilde{t_L}$, $\tilde{t_R}$ with masses $m_{\tilde{t}_{L,R}}$:

$$\mathcal{L}_{\tilde{t}} = |\tilde{t_L}|^2(m^2_{\tilde{t_L}} + y_t^2|H|^2) + |\tilde{t_R}|^2(m^2_{\tilde{t_R}} + y_t^2|H|^2), \tag{3.5}$$

where y_t is the SM top Yukawa coupling. The contribution to the higher dimensional operator hGG in equation 3.4 arises by integrating out the scalar top partner. This results in

$$\frac{y^2}{M^2} = \frac{1}{16\,v^2}\left(\frac{m_t^2}{m^2_{\tilde{t}_L}} + \frac{m_t^2}{m^2_{\tilde{t}_R}}\right), \tag{3.6}$$

where m_t and v are the SM top mass and EW symmetry breaking VEV.

The hidden glueball G lifetime estimated from the decay width to

a SM product X_{SM} is:

$$\Gamma(G \to X_{SM}) \approx \left(\frac{1}{12\pi^2} \frac{y^2}{M^2} \frac{v}{m_h^2 - M_{\tilde{G}}^2} \right)^2 \times \times (4\pi\alpha_F F_G)^2 \, \Gamma_{h \to X_{SM}}(M_{\tilde{G}}^2), \tag{3.7}$$

where $\Gamma_{h \to X_{SM}}(M_{\tilde{G}}^2)$ is the SM Higgs decay width to the same final product, which corresponds to that of an off-shell Higgs evaluated replacing the Higgs mass with the glueball mass $m_h \to M_{\tilde{G}}$. The hadronic matrix element creating the glueball from the gluon operator is parametrized in terms of its decay constant:

$$F_G = \langle 0 | Tr \, [\tilde{G}_{\mu\nu} \tilde{G}^{\mu\nu}] | \tilde{G} \rangle \tag{3.8}$$

We take QCD lattice calculation (56) as an estimative for F_G:

$$4\pi\alpha_F \, F_{\tilde{G} = f_0 r_0^{-3} \approx 2.3 M_{\tilde{G}^3,}} \tag{3.9}$$

where $f_0 = 167 \pm 16$, and r_0 can be expressed in terms of the glueball mass $M_{\tilde{G}} = a_0 r_0^{-1}$, with $a_0 = 4.16 \pm 0.12$.

The colorless glueball decay width is proportional to high powers of the glueball mass $M_{\tilde{G}}$ and the f-squark right mass $m_{\tilde{q}_R}$:

$$\Gamma(\tilde{G} \to X_{SM}) \propto \frac{M_{\tilde{G}}^7}{v^2 \, m_{\tilde{q}_R}^4}. \tag{3.10}$$

Since the Higgs decay width back to the SM depends simply on $M_{\tilde{G}}$, then the hidden glueball lifetime will be particularly sensitive to its mass.

Finally, the signal from the production of f-squarks can be of displaced vertices or missing energy depending on the glueball lifetime. The decay length $L = c/\tau = c\Gamma$ with $M_G = 12 - 60$ GeV is estimated to cover a large range from microns to kilometers (46). However, the hidden glueball lifetime is extremely sensitive to its mass, which varies with the confining IR scale. In the next section, we estimate the hidden sector strong coupling, which is necessary to calculate the glueball mass in terms of other parameters of the F-SUSY scenario.

3.1.2 Hidden confining scale

The strong folded coupling may be calculated from contributions to the beta function of a non-Abelian field theory with scalar fields:

$$\beta_F(N_S) = -\frac{g_F^3}{(4\pi)^2}\left(\frac{11}{3}C_2 - \frac{N_S}{3}C_r\right), \tag{3.11}$$

where $g_F = \sqrt{\alpha_F\, 4\pi}$ is the folded coupling, N_S is the number of scalars, the Casimir for SU(3) are $C_2 = 3$ and $C_r = 1/2$. We calculate the running coupling constant through the beta function:

$$\mu\frac{\partial g_F}{\partial \mu} = \beta_F(g_F). \tag{3.12}$$

In chapter 2, we argued that the bifold mechanism does not protect the Higgs mass at two-loop. Thus SUSY must be restored not to far above the TeV scale, typically $\Lambda_{UV} \sim 10$ TeV. Therefore, the running of the strong coupling in equation 3.11 must coincide with the SM strong coupling at the UV cutoff:

$$\alpha_F(\Lambda_{UV}) = \alpha_{SM}(\Lambda_{UV}) \tag{3.13}$$

Therefore, we use this boundary condition at the UV to calculate the evolultion of the hidden constant α_F.

Moreover, equation (3.11) depends on the number of scalars existing at the energy scale evaluated. For an energy scale at Λ_{UV}, there must be $N_S = 12$ because of the six f-squarks, considering right and left helicity. Half of them are integrated out below the left-handed f-squark mass. Finally, at a scale below the right-handed scalar mass, there is only the hidden gluons contribution. We estimated the f-squark masses in section 2.2.4, which shows that the contribution to the left-handed $m_{\tilde{q}_L}$ coming from the $SU(2)_L$ sector difference is approximate:

$$m^2_{\tilde{q}_L} \simeq m^2_{\tilde{q}_R} + K\frac{1}{4\pi^4}\frac{3}{4}g_2^2\Lambda_{UV}, \tag{3.14}$$

where g_2 is the EW coupling.

Therefore, using the scalar beta function in equation (3.11) and the running equation 3.12, we estimate the folded strong coupling $g_{F1}(\mu)$ at a scale μ up to the Λ_{UV}:

$$g^2_{F1}(\mu) = \frac{g_F^2(UV)}{1 + 32\pi^2\, g_F^2(UV)\beta_F(12)\ \mathrm{Log}(\frac{\Lambda_{UV}}{\mu})} \tag{3.15}$$

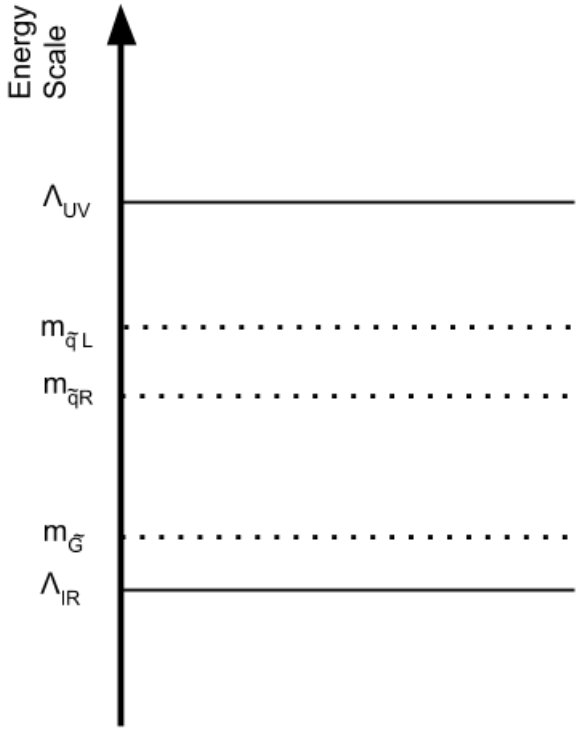

Figure 3.3: The F-SUSY spectrum in terms of the energy scale. The folded coupling is determined by the scalar beta function with the boundary condition at the UV from equations 3.11 and 3.13; where Λ_{UV} is typically 5 to 10 TeV. The f-squarks mass are calculated at one loop, and the difference $m_{\tilde{q}_L} - m_{\tilde{q}_R} \sim O(100)$ GeV from equation 3.14. Besides, bounds on $W\gamma$ shows that $m_{\tilde{q}_R} >$ 320 - 465 GeV (57). Moreover, the mass Glueball is determined by the the confinement scale Λ_{IR}, which is estimated from the folded coupling.

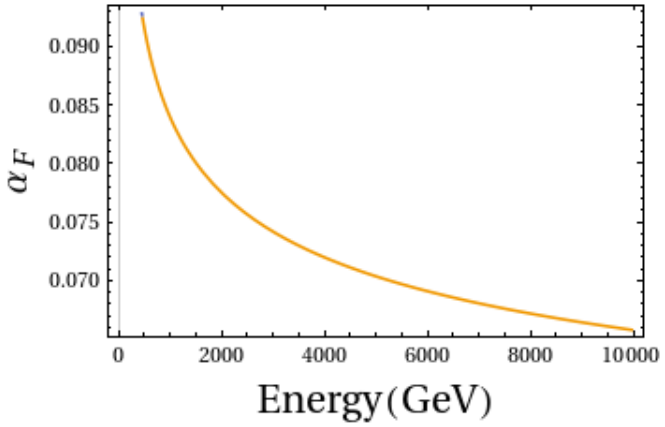

Figure 3.4: Strong folded coupling α_F as a function of energy scale

However, for energies between f-squarks masses $m_{\tilde{q}_L}$ and $m_{\tilde{q}_R}$, one must integrate out half of squarks contributions and obtain the running coupling constant:

$$g_{F2}^2(\mu) = \frac{g_{F1}^2(m_{\tilde{q}_L})}{1 + 32\pi^2\, g_{F1}^2(m_{\tilde{q}_L})\beta_F(6)\,\mathrm{Log}(\frac{m_{\tilde{q}_L}}{\mu})}. \tag{3.16}$$

At last, for energies below the right-handed f-squarks masses $m_{\tilde{q}_R}$ the contribution of all f-fsquarks are integrated out resulting in the running coupling constant:

$$g_{F3}^2(\mu) = \frac{g_{F2}^2(m_{\tilde{q}_R})}{1 + 32\pi^2\, g_{F2}^2(m_{\tilde{q}_R})\beta_F(0)\,\mathrm{Log}(\frac{m_{\tilde{q}_R}}{\mu})} \tag{3.17}$$

In conclusion, the running of the strong folded coupling g is represented in Figure 3.4.

The lightest state is the scalar glueball 0^{++}, and its mass scales between $4.7\Lambda_{IR} < M_G < 11\Lambda_{IR}$ (58). Figure 3.5 represents it in terms of the mass of the f-squark $m_{\tilde{q}}$ and the UV scale Λ_{UV}. As discussed before, the strong coupling boundary condition depends on the UV scale, while the number of scalars varies with the mass of the right handed f-squark. Fixing those two parameters, we can estimate the IR confinement scale matching the 0-loop and 1-loop beta function (59):

$$\Lambda_{IR} = m_{\tilde{q}}\, exp\left(-\frac{6\pi}{(11 \times 3 - n_S)\alpha_F(\mu)}\right) \tag{3.18}$$

where the n_S is the number of fermions in the theory and the hidden

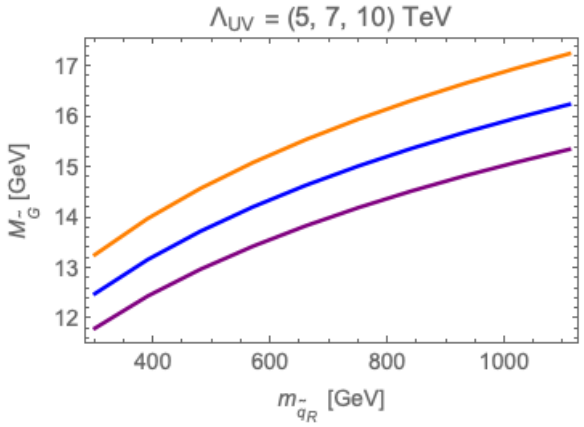

Figure 3.5: glueball mass in terms of f-squark mass for $\Lambda_{UV} = 5$, 7, and 10 TeV.

strong coupling at a given energy scale μ is $\alpha_F(\mu) = \frac{g_F^2(\mu)}{4\pi}$, as estimated in the Figure 3.4.

To sum up, the last section showed that it is possible to observe displaced vertices inside the LHC detectors. However, the glueball lifetime is extremely sensitive to its mass, thus leading to a wide range of possible values of decay length from microns to km. Moreover, figure 3.5 shows that it is possible to have relatively light glueballs in an F-SUSY scenario. It was calculated for right-handed f-squark mass above 500 GeV, restoring SUSY above LHC operating scale. We are now going to study in more detail the hadronization process from folded gluons to glueballs in order to estimate the distribution of displaced vertices at the LHC.

3.2 Hadronization of hidden gluons

We now model the hadronization process of glueballs from hidden glue. The FF describes the mechanism of a parton to result in a hadron. The production cross-section convoluted with the FF estimates the number of glueballs produced per gluon. Finally, in section 3.3, we use this function and the glueball lifetime to calculate the average number of displaced vertices through the length of the LHC detectors.

3.2.1 Fragmentation Function

Partons are elements that compose hadrons. They are never observed free because of confinement from strong interactions. The Fragmentation Function (FF) gives the process of a parton to form a hadron

in a given energy scale (60; 61; 3). It is analogous to the distribution functions (PDF), which gives them a process to occur with an initial parton inside a hadron. There is also the hadronization string model, where each parton forms a gluon string. Its tension produces a pair of lighter particles, originating havier bound states. We are going to model the hidden gluon to the glueball process as a FF distribution.

Suppose a parton k, with energy E_k is produced at the collider. The function describing a forming hadron h with energy E_h is given by the FF $D_k^h(z)$, where the variable z is defined by

$$z \equiv \frac{E_h}{E_k}, \tag{3.19}$$

with $0 \leq z \leq 1$. This function must be normalized so the total fragmenting into any available energy is one:

$$\int_{z_{min}}^{1} z\, D_k^h(z) dz = 1, \tag{3.20}$$

where $z_{min} = m_h/E_k$ is kinematically defined by the hadron's lowest momentum.

Furthermore, the FF convoluted with the differential cross-section describes the entire process of two elements A and B generating a hadron h plus any other product X:

$$\frac{d\sigma}{dE_h}(AB \to hX) = \sum_k \int \frac{d\sigma}{dE_k}(AB \to kX) \times \times D_k^h\left(\frac{E_h}{E_k}\right) \frac{dE_k}{E_k}, \tag{3.21}$$

which is summed over every parton k and integrated in the energy E_k. Finally, the average number of hadrons h produced can also be calculated by integrating the FF:

$$\langle n_k^h \rangle = \int_{z_{min}}^{1} D_k^h(z) dz, \tag{3.22}$$

where $\langle n_k^h \rangle$ is the average multiplicity of the hadron h.

In standard QCD, the FF is obtained from experimental data at a given energy scale. To predict them at higher energies, they are

evolved using Dokshitzer Gribov Lipatov Altarelli Parisi (DGLAP) equations:

$$\frac{dD_k^h(z,t)}{dt} = \frac{\alpha(t)}{2\pi}\int_0^1 \frac{dw}{w} D_k^h(z/w)P(w), \tag{3.23}$$

where the variable t is defined by $t \equiv \mathrm{Log}(\mu^2)$, μ is the energy scale at which the function is evaluated, and the strong coupling $\alpha(t)$ was calculated in section 3.1.2. The splitting function $P(w)$ characterizes each parton contribution to the FF (62). The process of the hadronization of folded gluons into glueballs will only need the gluon splitting function P_{gg} (1).

3.2.2 Gluon splitting function

Splitting functions describe how the energy is divided through partons. For instance, the formation of hidden glueballs from a hidden glue uses the gluon fragmentation function to distribute the initial state energy into an average N glueball. Splitting functions cannot be directly measured at the collider, and they usually contain a collinear singularity factor. However, recent studies show a different prospect from the analysis of jet substructures (63). In this work, we are going to use the usual QCD gluon splitting function to describe the fragmentation of hidden gluons to glueballs. This section will illustrate the aspects of the gluon splitting function needed to model the FF. However, a more in-depth analysis can be made, which will be introduced in the appendix B.

The gluon splitting function can be expanded perturbatively in terms of the strong coupling $\alpha(t)$. In this work we will only use leading order terms $\frac{\alpha(t)}{2\pi}P_{gg}^{(0)}$ (64), which is described by:

$$P_{gg}^0(z) = 6\left(\frac{1-z}{z} + \frac{z}{[1-z]_+} + z(1-z) + \frac{11}{12}\delta(1-z)\right). \tag{3.24}$$

The term $\frac{z}{[1-z]_+}$ in the above equation is taken in the limit to the right of z going to 1. The Dirac delta function $\delta(1-z)$ corresponds to the value of the following term at $z = 1$. The gluon splitting function must be carefully treated numerically since it diverges at $z = 0$ and $z = 1$. It can be properly calculated in terms of moments using the

Mellin transformation (MT),

$$f(z,t) = \int_0^1 dx\, x^{z-1} f(x,t). \tag{3.25}$$

To transform the gluon splitting function it sufices to use the transformations given in the table 3.1 (64).

f(z)	MT of f(z)
$\delta(1-z)$	1
z^ρ	$\frac{1}{x+\rho}$

Table 3.1: Mellin transforms of functions f(z)

Therefore, the gluon splitting function in Mellin space is given by:

$$P_{gg}(x) = 2 \times 3 \times \left(\frac{11}{12} + \frac{1}{x(x-1)} + \frac{1}{(x+1)(x+2)} - S_1(x) \right), \tag{3.26}$$

where $S_1(x)$ is the harmonic sum:

$$S_1(x) = \sum_{k=1}^{x} \frac{1}{k}. \tag{3.27}$$

However, the sum $S_1(x)$ clearly diverges for large values of x. Reference (65) presents a numerical approach to treat harmonic sums by expanding $S_1(x)$ is in terms of $S_r(x,r)$:

$$S_1(x,r) = S_r(n+r) - \sum_{k=1}^{r} \frac{1}{k+x}, \tag{3.28}$$

where S_r is defined as:

$$S_r(x) = \gamma_E + \Psi(x+1), \tag{3.29}$$

$$\Psi(x) = \mathrm{Log}(x) - \frac{1}{2x} - \frac{1}{12x^2}, \tag{3.30}$$

where γ_E is the Euler gamma constant. The constant r is chosen to be a large number such that $\frac{1}{|x+r|}$ is small even for low values of x.

The second approximation is taken for small values of x, where the gluon splitting function is no longer valid. In this case we can use the leading Log expansion of the gluon splitting function (3; 64) is:

$$P_{gg}(x) = -\frac{1}{4} \left(x - 1 - \sqrt{(x-1)^2\, 24 \frac{\alpha(t)}{\pi}} \right). \tag{3.31}$$

The limit for small x is typically taken at

$$\alpha(t)\,\mathrm{Log}^2(1/x) \approx 1 \tag{3.32}$$

The FF far from z=1 is approximated in a Taylor expansion according to reference (64). The FF in a low x behaviour is:

$$D(x) \propto \frac{1}{x} exp\left[-\frac{1}{2\sigma^2}(\xi - \xi_p)^2\right], \tag{3.33}$$

where x is the Mellin transform variable, and the parameters σ, ξ and ξ_p are defined as:

$$\xi = \mathrm{Log}\,\frac{1}{x}, \tag{3.34}$$

$$\xi_p = \frac{4\pi}{4\,b(N_S)\alpha_F}, \tag{3.35}$$

$$\sigma^2 = \frac{4\pi}{24\,b(N_S)}\sqrt{\frac{2\pi}{3\alpha_F^3}}. \tag{3.36}$$

The coupling α_F in the F-SUSY scenario is estimated in section 3.1.2 . We estimate the low x approximation to be valid for values $0 < x < 0.15$. For a more precise calculation, it is necessary to include higher orders of the Log expansion from the gluon splitting function, and resummation over the strong coupling α_S (66). However, we are going to use only the leading Log expansion in equation 3.31.

3.2.3 Glueball Fragmentation Function

The FF $D_k^h(z)$ are often parameterized as:

$$D(z) = N(1-z)^\beta, \tag{3.37}$$

where N is the normalization. Each process is characterized by choosing the parameter β that agrees with experimental data at a given energy. To calculate the FF in different energies, we can use the DGLAP evolution in equation 3.23.

The hidden gluon to glueball FF is challenging to model, since we do not have measurements to find the boundary condition of the DGLAP evolution. Therefore, we assume an initial condition at an energy scale μ_0. The most plausible hypothesis is to model it as a pion

produced from a valence quark due to similarities of QCD sum rules (67). This function is described at $\sqrt{s} = 30$ GeV as a linear function in $(1-z)$ (68), aka $\beta = 1$. Imposing the normalization condition 3.20, the hidden glue at $\mu_0 = 30$ GeV is modeled as:

$$D_V(z) = 6(1-z). \tag{3.38}$$

We implemented two strategies to model the hidden glue FF. The first one we performed the DGLAP evolution in Mellin space, which is detailed in Appendix B. However, there were many numerical issues, and the final average multiplicity was not increasing with energy. Meanwhile, the second strategy used the results for the asymptotic average multiplicity as a function of the energy (64). In this case, the average multiplicity is calculated using the gluon splitting function in the Mellin space, where the singularities in terms of low x, or $z \to 1$ have been resumed. To calculate the FF of hidden gluons to glueballs we use the initial condition in equation 3.38 with $\beta_0 = 1$. The integral of this initial input gives the average number from equation 3.22 of $N_0 = 2.5$ glueballs per gluon. The FF evolution for higher energies is made through the asymptotic average number resulting from the final DGLAP evolution in an energy $t = \mathrm{Log}(\mu)$:

$$\langle N(t) \rangle = N_0 \, Exp \left\{ \frac{1}{b(N_S)} \sqrt{\frac{6}{\pi \alpha_F}} + \left(\frac{1}{4} + \frac{5 N_S}{54 \pi b(N_S)} \right) \mathrm{Log}\, \alpha_F \right\}. \tag{3.39}$$

We estimate the value of β in the new energy scale by comparing the average number calculated in 3.39 with the one in equation 3.22.

Finally, figure 3.6 is the estimated FF of hidden glue to glueballs. The calculation was performed supposing the low z matching point at $z_M = 0.1$, the glueball mass fixed at $M_{\tilde{\mathrm{G}}} = 15, 20, 30$ GeV and $\Lambda_{UV} = 7$ TeV. The different colors red, blue, orange, and violet corresponds respectively to the hidden gluon energy at 300, 500, 700, and 900 GeV. We also used other matching points and showed that the final result does not change drastically (21).

3.3 Distribution of displaced vertices at the LHC

We showed that the production of f-squarks in the LHC could generate highly displaced vertices. The pair of particles would promptly

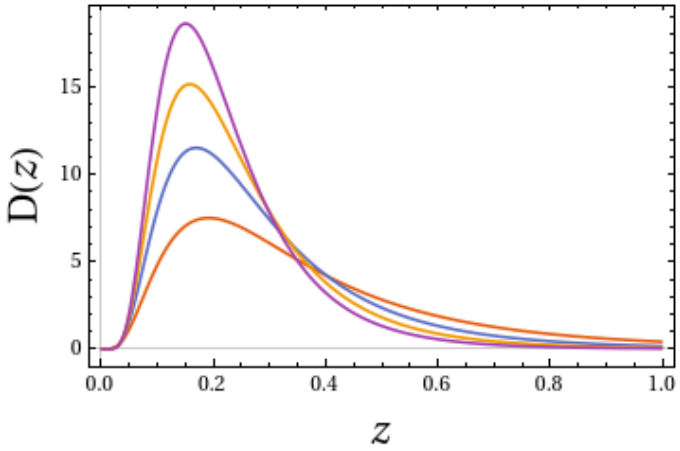

(a) $M_G = 15$ GeV.

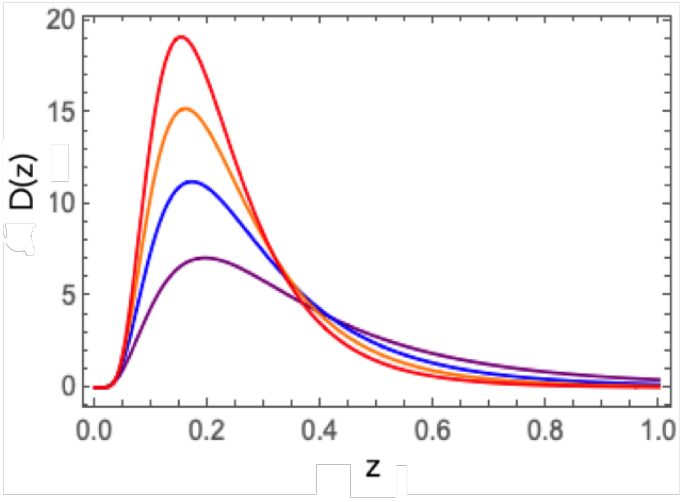

(b) $M_G = 20$ GeV.

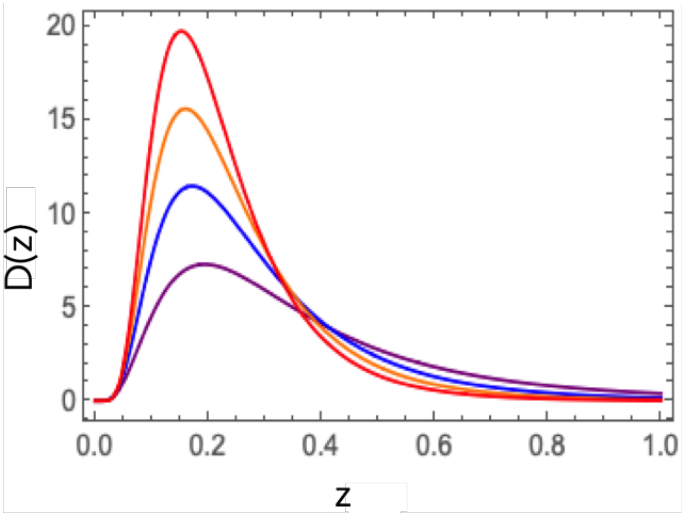

(c) $M_G = 30$ GeV.

Figure 3.6: FF of hidden gluons to glueballs supposing the low z matching point at $z_M = 0.1$, the glueball mass at $M_{\tilde{G}} = 15$, 20, and 30 GeV and $\Lambda_{UV} = 7$ TeV. The different colors red, blue, organge, and violet respectively correspond to the hidden gluon energy at 300, 500, 700, and 900 GeV.

annihilate each other into dark gluons, which hadronizes to invisible glueballs. We estimated the FF, which gives the average multiplicity of glueballs per gluon. Although these objects are invisible to the detector, they can decay to the SM through high order operators involving the Higgs. We now convolute the multiplicity and lifetime of the glueball to estimate the distribution of displaced vertices.

To estimate the possible signals in the detector, we calculate the average number of decays up to a certain position L from the initial vertex. This is obtained by integrating the FF $D(z, \mu)$ at an energy scale μ with the probability of decay at the distance L.

$$N_{DV}(L) = \int dz D(z, s)(1 - e^{-\frac{L}{L_G}}), \tag{3.40}$$

where the mean life τ_G gives the decay length L_G as:

$$L_G = c\tau_G \frac{z}{z_{min}}. \tag{3.41}$$

The glueball lifetime is the inverse of the decay width $\tau = 1/\Gamma$, which is calculated from equation 3.10.

Figure 3.7 shows the results of the multiplicity of events from the interaction point to a given position L from the primary collision point. The hidden glueball decay width in equation 3.10 already shows that the results are susceptible to its mass, which is proportional to M_G^7. We performed this calculation varying the glueball mass as $M_{\tilde{G}} = 15$, 20 and 30 GeV. The right-handed f-squarks masses define the hard f-gluon energy, which is fixed at 300, 500, and 700 GeV, where the horizontal lines are the total multiplicity. To compare the decay length with the dimensions of the LHC detectors, we also drew the vertical dashed lines marking the ATLAS layers. The full detector is approximately 10 m long, and the dashed lines correspond to the length of each sector: inner tracker, electronic and hadronic calorimeter, and the muon system.

We observed that the decay width in equation 3.10 is extremely sensitive to the glueball mass. It also is sensitive to the f-squark mass, which dictates the gluon energy. This sensitivity is also present in the results of figure 3.7. The first case to analyze is the results of a light glueball with $M_{\tilde{G}} = 15$ GeV. The light f-squark can produce signals located up to the muon system. However, when increasing the

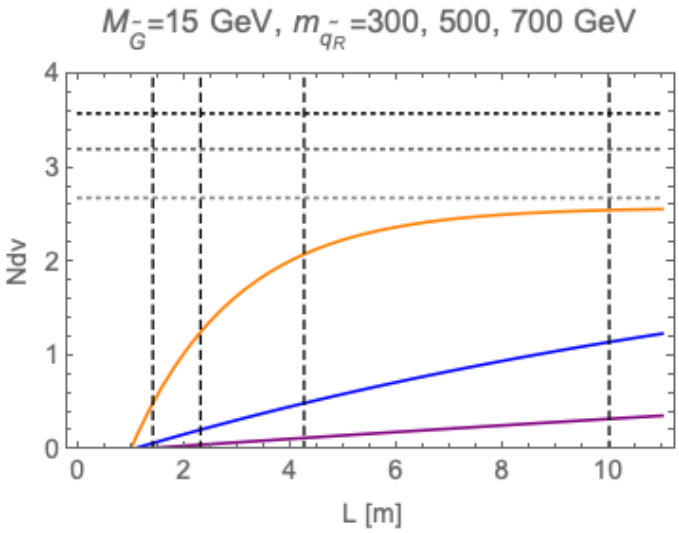

(a) $M_G = 15$ GeV.

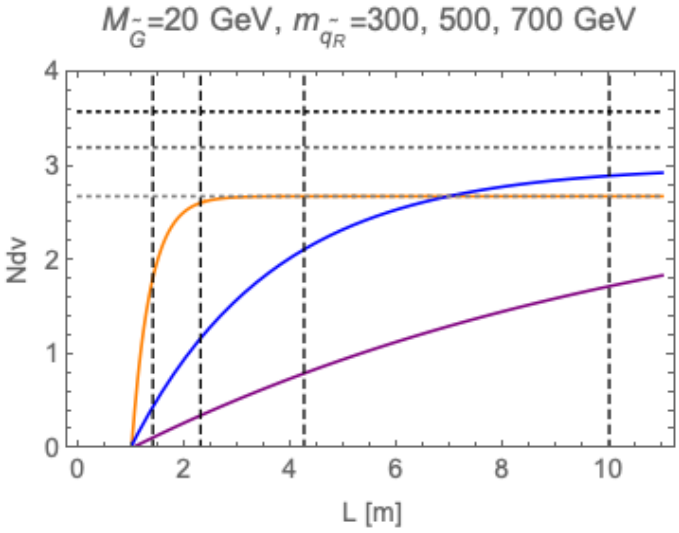

(b) $M_G = 20$ GeV.

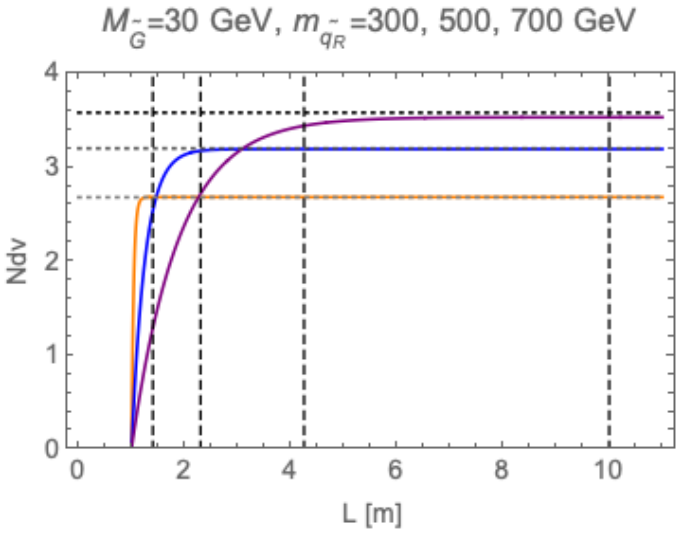

(c) $M_G = 30$ GeV.

Figure 3.7: The average multiplicity of displaced vertices from the collision point to the position L. Each plot fixes the glueball at $M_{\tilde{G}} = 15$, 20, and 30 GeV, and $\Lambda_{UV} = 7$ TeV. The different colors orange, blue and violet correspond respectively to the hidden gluon energy at 300, 500, and 700 GeV. The horizontal lines are the average multiplicity, an the vertical dashed lines marking the ATLAS layers.

f-squark mass, it is most likely to decay at distances more significant than the detector length, showing a large fraction of missing energy. For an increasing mass of the glueball, the situation is much different. The second plot considers $M_{\tilde{G}} = 20$ GeV, where there may be traces from the electromagnetic (EM) calorimeter to the muon chambers. Although the heavy 700 GeV right-handed f-squark is most likely to decay in the last section, we observe that 2/3 of the events are inside the detector for a lighter f-squark, divided almost equally between the calorimeters and the muon system. Most of the events are inside the detector for $M_{\tilde{G}} = 30$ GeV, including a large fraction inside the EM calorimeter, showing the possibility of detecting vertices anywhere in the detector multiple times.

Therefore, it is necessary to search for displaced vertices in all segments of the detectors. The plots in figure 3.7 show that the system is susceptible to relatively small changes in the glueball mass. Only 5 to 10 GeV differences imply a distinct multiplicity of the events in each sector of the detector. We observed that the more massive glueball states of 20 and 30 GeV are more likely to have a unique signature, while the lightest may culminate in searches identified with a large fraction of missing energy.

3.4 Discussions

The search for long-lived particles (LLP) is a recurrent discussion among theorists and experimentalists (69). Despite the challenging analysis, there are searches for hadronic LLP in ATLAS, CMS, and LHCb. They are mostly motivated by SUSY and Hidden Valley models. First, ATLAS presented a data analysis for two hidden objects decaying in the hadronic calorimeter (70; 71), and decays within the muon system or inner detector (72). There are also decays in association with large missing energy (73; 74). Second, CMS searches for displaced jets includes both Run 1 and 2 (75; 76; 77), and the analysis in multijet events (78). At last, LHCb searches include one and two all-hadronic displaced vertices (79; 80).

However, theories with an EW production of the hidden sector escape current bounds from the LHC. The cross-section in figure 3.2 is under one fb, while the analysis made in the LHC considers larger

values, which are comparable with QCD production. Therefore, the results for the future High Luminosity LHC are promising for the search of displaced vertices from the hidden glue. Although the results were obtained in the F-SUSY scenario, the FF is model-independent and can be applied for different hidden glue scenarios. For example, the Quirky Little Higgs model scenario is very similar to F-SUSY.

To sum up, figure 3.7 shows the final distribution of displaced vertices. We have modeled the FF to obtain the multiplicity of hidden glueballs from an f-squark EW production. The hidden glueball lifetime is very sensitive to its mass. Thus the signature in the collider may vary from missing energy to multiple vertices at any sector of the detector. Future searches must include multiple displaced vertices on each side of the detector, and analysis through the whole detector.

4

Dark matter indirect searches with a skipper CCD telescope on a satellite

The second part of the thesis concerns dark matter (DM) indirect searches. Although gravitational observations have proven the existence of DM, there is no evidence of its particle nature. Several experiments are searching for candidates of DM, including collider searches, direct, and indirect detection. The later probes processes where the DM candidates generate SM particles. For instance, indirect detection includes cosmic rays experiments, neutrino detectors, and astronomical observations. Especially, X-ray band telescopes can detect rare signals at the keV energy scale. The most competitive X-ray telescopes, such as CHANDRA and XMM-NEWTON, use charge-coupled devices (CCD) for imaging and spectroscopy. CCDs are used in industry and science. They are composed of silicon semiconductors that are capable of capturing precise pixel size photon signaling (81; 82; 83; 84). However, this technology has a significant electronic noise of an average $2\,e^-$ root-mean-squared (rms) per pixel. The skipper CCD can lower it to $0.068\,e^-$ rms per pixel by improving the CCDs with a multiple readout technique, allowing it to measure a single electron signal in the silicon band. The skipper CCD is the most sensitive electromagnetic (EM) calorimeter that can operate at temperatures order of 100 K. Furthermore, astrophysical observations require telescopes with a narrow opening angle. However, since DM interactions with light are extremely weak, it is compelling to launch a new telescope with a large field of view (FOV) to analyze a large volume and increase the number of events. In this chapter, we describe an ongoing project where we

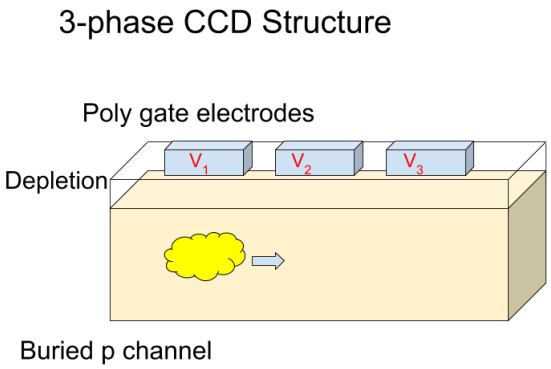

Figure 4.1: The CCD structure is composed of a small depletion region (white), gate electrodes (blue), and the buried p channel (yellow). When the incoming photon reaches the depletion, it deposes its energy due to the photoelectric effect. Then, the charges are confined under the gate, in the buried p channel, as represented by the yellow cloud in the picture. The electron package is stored in a pixel, which is defined by the gate electrodes. Each electrode varies the voltage V (red) to move the package to the next gate in the series until reaching a readout at the end of the pixel line.

study different DM models and their potential signals in a new skipper CCD telescope with a broad FOV on a satellite.

4.1 X-ray telescopes

Photon emission lines coming from DM annihilation can probe the particle nature of Dark Matter indirectly. DM indirect searches include experiments such as neutrino detectors, cosmic rays, and astronomical observations. Notably, the X-ray telescopes put bounds on new light particles while detecting photons in an energy band of 100 eV to 100 keV. The X-ray telescopes were first sent to space in 1962. They are essential to study stars, galaxies, quasars, and other kinds of cosmic objects (85). However, indirect DM detection requires exact measurements because the interactions with light are feeble, and the X-ray presents an extensive background. Charged Coupled Devices (CCD) are capable of distinguishing such rare signatures due to its precision and low energy resolution. The most competitive X-ray telescopes, such as Chandra and XMM-Newton, use CCDs for both imaging and spectroscopy (22; 23).

The CCD is a solid-state electronic device developed in 1970 (81; 82; 83; 84) with applications in the industry, particle physics detection

and astronomy. The detector is based on a semiconductor silicon substrate. The signal is generated because of the photoelectric effect. The incident photon produces electron-hole pairs proportionally to its energy, which is on average of one electron-hole pair for each 3.7 eV absorbed. Figure 4.1 represents the CCD structure in three layers: gate, depletion, and buried p channel. The depletion corresponds to the active region where most of the photon absorption occurs. It is a silicon structure between the poly gate electrodes and the buried channels. The gate structure on the surface of the detector defines the pixel boundaries. After the photoelectric effect, the gates apply an electric field to store the charges on a volume in the p silicon buried channel, as represented by a yellow cloud in figure 4.1. At last, a chain of series gates varies the voltage in order to move the electron package from one gate to another until reaching the end of the line, where a single readout channel is located. Furthermore, thermal fluctuations may also promote the number of electrons in the silicon conduction band, called dark current. Therefore, the CCDs must operate in low temperatures.

The photon signal in the CCD can generate digital imaging or spectroscopy with small pixel size and excellent precision. Optical imaging usually uses two-dimensional CCDs with pixel sizes -20μm $\times 20\mu$m and area of the order of 1 cm^2. Figure 4.2 is a scheme of the pixel two dimensional CCD detector, where photons can be detected in the pixel-sized precision. For example, the Chandra telescope has 10 CCD detectors for both imaging and spectroscopy (86). It operates at the temperature of 144K to 183K, with 1024 by 1024 pixels of 23.985 μm. The effective area is of 110 cm^2 at 0.5 keV; 600 cm^2 at 1.5 keV; and 40 cm^2 at 8.0 keV. The effective area for Chandra depends on the geometric mirror area, reflectivity, the detector quantum efficiency, and diffraction grating efficiency. The minimum row readout time is 2.8 ms and the system noise of 2 e$^-$ rms per pixel. On the other hand, CCDs have high electronic noise, which can be severely suppressed using the improved version of this technology called skipper CCD (24).

The first proposition of a skipper CCD (87; 88) included the multiple readout technique, using a floating output gate, which reduces low-frequency readout noise. However, this detector generated spurious charges (89). The operating skipper CCD (24) couples the floating

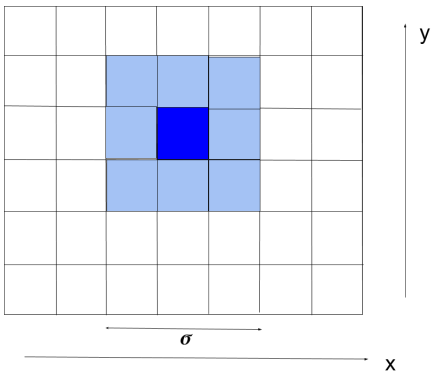

Figure 4.2: The CCD is a two-dimensional detector divided into a large number of precise pixels. The signal generated in a single pixel can be located with its decreasing intensity width represented by the shades of blue in the picture.

gate output stage to a small-capacitance sense node and isolate both from noise sources. It is capable of measuring electric charges in a single pixel in multiple, independent, and non-destructive events, as shown in figure 4.3 from reference (24). The skipper CCD accuracy allows it to measure individually one to thousands of electrons, counting optical and near-infrared photons. It is the most sensitive EM calorimeter that operates at temperatures as low as 140K. The skipper CCD properties are listed in table 4.1 from references (24; 90). Furthermore, the fabrication process does not require major modifications in the usual CCD to obtain the non-destructive readout. Therefore, it can be implemented at a low cost in existing CCD manufacturing.

Characteristic	Value	Unit
Format	4126×866	pixels
Pixel Scale	15	μm
Thickness	200	μm
Operating Temperature	140	Kelvin
Number of amplifiers	4	
Readout time (1 sample)	10	μs/pix/amp
Readout Noise (1 sample)	0.068	e^-rms/pix

Table 4.1: Skipper CCD properties listed from (24; 90)

In this work, we analyze the possibility of using a skipper CCD as an experiment for indirect detection of Dark Matter. The skipper CCD is a competitive device compared with other telescopes. It is advantageous because of its low electronic noise of 0.068 e^-rms/pix, while usual CCD detectors have a few e^-rms/pix. Besides, most oper-

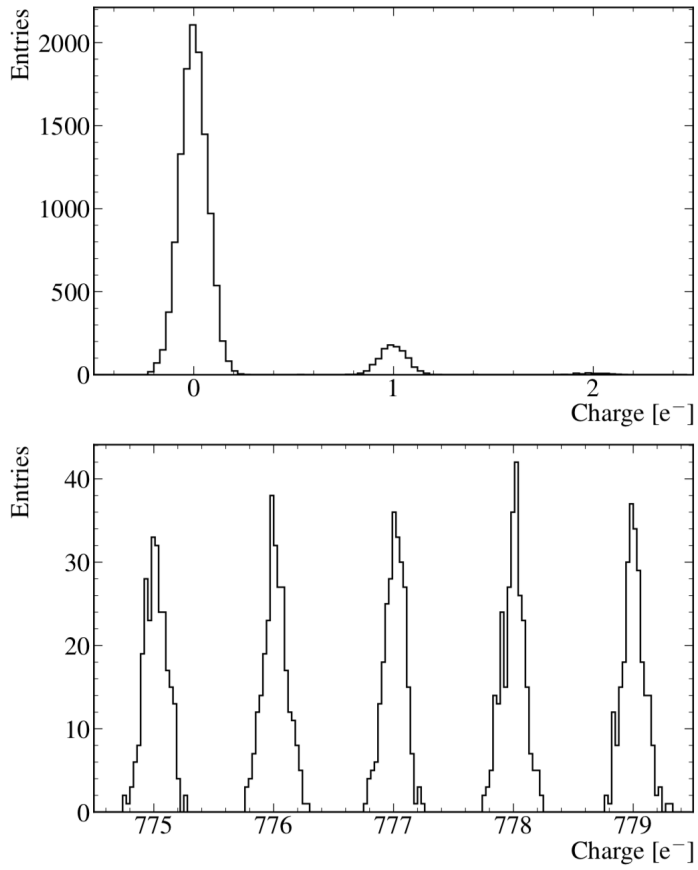

Figure 4.3: Measurements of single electron charges in a skipper CCD, with 4000 samples per pixel, and bin width of 0.03 e−. The plot on the top is a low-light level illumination, the peak at 0 e^- has rms noise of 0.068 e^- rms/ pix. The graphic below is a high-light level illumination, where the peak at 777 e^- has the noise of 0.086 e^- rms/ pix. The Gaussian fits have $\chi^2 = 22.6/22$ and $\chi^2 = 19.5/21$, respectively. The two measurements demonstrate integer electron peaks distinctly resolved, and the single-electron sensitivity over a large dynamical range. Plot from reference (24).

ating X-ray telescopes have a narrow FOV. They usually give the FOV as the aperture angle of each two-dimensional direction, of the order of $((10-30)' \times (10-30)')$, which is useful for astronomical research. However, for indirect DM searches, it is useful to analyze a large volume of space since the interactions with the SM are feeble. Therefore, it is compelling to launch a new experiment with a significant angle aperture, typically of the order o $20^o \times 20^o$.

Table 4.2 compares the proposal of a satellite with a skipper CCD with the most competitive operating X-ray telescopes: XMM-Newton (23; 91; 92), Chandra (22), Suzaku (93) and Swift (94). The table lists the energy band, noise, FOV, and energy resolution. It shows that the skipper CCD would have a much lower electronic noise and larger FOV, while its other characteristics are similar to the other experiments. Its calibration curve lies over 0.1 keV to 15 keV, including X-rays and optical photons. Telescopes based on CCD cameras have high values of energy resolution; for example, XMM-Newton EPIC camera full width at half maximum $FWHM \approx 100$ eV for 2 keV. However, the skipper CCD would have a threshold at 3 eV and $\Delta E \lesssim 10$ eV. Therefore, it would have a much more improved energy resolution of the order $E/\Delta E \sim 1000$. Reference (95) claims that SXS microcalorimeter in ASTRO-H also has low energy resolution $FWHM < 7$ eV, though its FOV is narrow, about $3' \times 3'$.

Experiment	En. Band (keV)	Noise (e^-rms/pix)	FOV	En. Resolution ($\frac{E}{\Delta E}$)
Skipper CCD	0.1-15	0.068	$20^o \times 20^o$	~ 1000
Chandra	0.1 -10	2	$30' \times 30'$	9-35
Newton	0.1-15	5	$33' \times 33'$	20-50
Swift	0.2-10	1	$23.6' \times 23.6'$	42
Suzaku	3- 79	2.5	$17' \times 17'$	20 - 100

Table 4.2: Comparison between skipper CCD proposal and the most competitive operating X-ray telescopes. The FOV is usually given for a two dimensional area, which is order of $17' \times 17'$ wide in a common X-ray telescope. However, the new experiment would have a broad opening angle, in the order or $20^o \times 20^o$.

Cosmological bounds severely suppress the interaction of DM particles with an EM field. However, the new telescope would have low electronic noise and large FOV, which should significantly increase the number of events over the vast X-ray background. It is compelling to launch a new telescope in Earth orbit, which should be relatively low

cost and scientifically significant. In the next section, we compute the signal of X-ray photons arriving at this detector using various DM models, in order to estimate their sensitivity to new physics.

4.2 X-ray signatures from DM models

Indirect searches using the new skipper X-ray telescope around Earth can probe several DM models. Dark Matter indirect detection can be studied in detail in lectures such as (96). We propose to calculate the incoming X-ray flux in different scenarios: sterile neutrino decays, resonant scattering, scattering with nuclei from the Earth, axion searches using the Earth magnetic field, and searches for mirror stars. We estimate the new detector sensitivity to new physics over the galactic X-ray background.

The first scenario we analyze is motivated by the XMM-Newton and Chandra observations of the Perseus cluster, and the Andromeda galaxy shows a 3σ excess around 3.5 keV (97; 98) and from the Galactic Center (GC) (99). One possible explanation for this excess is keV-range relic neutrino decays (100; 101). In this scenario, sterile neutrinos formed in the early universe can form part of DM, depending on the production model (102; 101). In this case, the 7 keV sterile neutrino would decay into an active neutrino and a photon, generating the excess in the spectrum. However, the significance of the signal is not strong enough to prove the DM particle existence. It is necessary to increase the energy resolution of the detector (103), which can be achieved with a skipper CCD. Furthermore, the large opening angle would increase the number of events. Our results show that it is necessary to expose the telescope to the GC for only five minutes to obtain a significant signal over the background.

In the second scenario, we suppose that DM particles interact in an effective Lagrangian containing an EM dipole (104). In this case, a fermionic neutral field χ_1 interacts with X-rays through a resonant excited state χ_2. The signal generated can be either an absorption line or an excess, where the incoming photon energy probes roughly the mass squared difference between the two fermions. The same interaction is also present in the third scenario of scatterings with nuclei from the Earth. In this case, the incoming DM flux contains

the fermionic χ_1 field, which scatters with a nucleus inside the planet resulting in the excited state χ_2, which in its terms decays back to $\gamma\chi_1$. The final decay must occur outside the atmosphere since most of the X-rays are absorbed by matter. Therefore, the telescope can also be sensitive to signals captured by pointing towards Earth.

The fourth scenario includes axion searches, and it also requires the detector to point to Earth. Axion like particles may be converted to X-ray photons in the presence of a magnetic field (105). It is possible to use the Earth magnetic field to capture this effect (106). Although the strength is weak, a large opening angle telescope pointing to the planet would integrate a large volume, which may increase the detector sensitivity. At last, the final scenario considers mirror stars, which were proposed in a hidden sector scenario (107; 108). They would have an SM nugget and dark mirror particles in the surrounding. These new objects can be probed through X-ray emissions coming from the mixing between the SM photon and dark photons.

In order to estimate the sensitivity to new physics in the telescope, we first calculate the incoming X-ray flux ϕ at a given photon energy E_γ:

$$\frac{d\phi}{dE_\gamma} = \frac{\frac{dN_\gamma}{dE_\gamma}}{\text{Area}_{\text{detector}} \times \text{exposure time}}, \tag{4.1}$$

The count of photons N_γ is obtained assuming the detector is pointing to a certain source at a distance d, as shown in figure 4.4. Suppose this flux is coming from a differential volume dV located at the telescope line of sight $\vec{l}$ with a certain DM number density n_χ. Therefore, N_γ should be proportional to n_χ divided by the superficial area that the line of sight covers, multiplied by the probability of interaction P_{int} and integrated over all possible $\vec{l}$:

$$N_\gamma = \int_0^\infty l^2 dl \int_{FOV} d\Omega \, n_\chi P_{int}, \tag{4.2}$$

where the FOV is restricted by the opening angle and $d\Omega = 2\pi d(\cos(\theta))$. The physics of this process determines the probability P_{int}, which is calculated from the cross section, or the decay rates of each scenario. The telescope sensitivity will also depend on its energy resolution, besides the extensive X-ray background. If the incoming flux can overcome these two restrictions, then the model can be probed with this experiment.

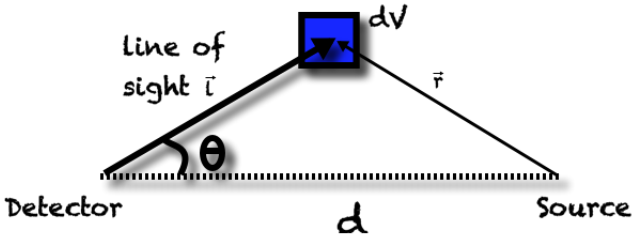

Figure 4.4: Scheme of the telescope reach pointing to a source at a distance d. We calculate the incoming photons flux produced at a differential volume dV, which is delimited by the detector line of sight $\vec{l}$ with an opening angle θ.

4.3 Sterile neutrinos and the 3.5 keV line

Neutrino physics can play an essential role in DM models. One possible candidate extends the SM electroweak sector with additional massive right-handed or sterile neutrinos (100). Sterile neutrinos, as a candidate of DM, must obey cosmological bounds. Particularly large scale structure simulations determine that the relic neutrino mass should be between (0.1 - 1.0) keV to form warm dark matter. Other mechanisms may be obtained in cold and hot scenarios (100; 101) The sterile neutrino couple directly to left-handed or active neutrinos. The most efficient production mechanism is via neutrino oscillations. Meanwhile, they can decay to three active neutrinos or generating a photon and active neutrino. The radiative decay mode is much more relevant experimentally, producing a quasi-monochromatic photon line at an energy corresponding to half the sterile neutrino mass. The mass mixing term between the sterile and active neutrino generates a parameter θ_ν, which controls most of its phenomenology. For instance, the decay width of $\nu_S \to \nu + \gamma$ is proportional to $\sin^2(2\theta_\nu)$.

Since early universe models predict the relic neutrinos to be in the keV range, its decay to X-rays could explain the XMM-Newton observations of the Perseus cluster and the Andromeda galaxy (97; 98) and from the GC (99), which has $> 3\sigma$ excess around 3.5 keV. On reference (109), Figueroa Feliciano et al. propose an experiment similar

to the skipper CCD on a satellite: a telescope with and large FOV on a Rocket. In this case, the X-ray detector is a microcalorimeter that operates at low temperatures at 50 mK. They show that a 7 keV neutrino decay would generate a signal in the detector after an exposure time of 300 s. We have reproduced this calculation for a skipper CCD in a satellite and confirmed a similar exposure time of approximately five minutes to have a significant effect.

To predict the total flux arriving at the telescope, we may first suppose an infinitesimal volume containing a dark matter density mass ρ at a distance defined by the line of sight $\vec{l}$ as illustrated in figure 4.4. The flux is calculated generically in equations 4.1 and 4.2 for a DM number density n_χ and a probability of interaction P_{int}. In this scenario, we assume the number density is:

$$n_\chi = \frac{\rho}{m_s}, \tag{4.3}$$

where ρ is the DM halo mass density profile and $m_s = 7$ keV, the mass of the sterile neutrino. Moreover, the probability of interaction P_{int} depends on the decay rate Γ, which is limited because the DM candidate must have a considerable lifetime in order to preserve cosmological bounds from the early universe.

The decay rate depends on the mixing angle θ_ν between the active and sterile states, as shown in reference (110).

$$\Gamma = \frac{9\alpha G_F^2 m_s^5 \sin^2 2\theta_\nu}{1024\pi^4} = (1.38 \times 10^{-29} s^{-1}) \left(\frac{\sin^2 2\theta_\nu}{10^{-7}}\right) \left(\frac{m_s}{1 \text{ keV}}\right)^5. \tag{4.4}$$

According to the reference (110) observations fix the mixing angle

$$10^{-11} \leq \sin^2(2\theta_\nu) \leq 10^{-10}. \tag{4.5}$$

. For a $m_s = 7$ keV sterile neutrino, its lifetime will be order of $\tau \sim 10^{27}$ to 10^{28}.

Therefore, using equations 4.1, 4.2, and 4.3, the total incoming flux ϕ is given by:

$$\phi = \frac{\Gamma}{m_s} \frac{1}{4\pi} \int_{FOV} \int_0^\infty \rho(r(l,\theta)) dl d\Omega, \tag{4.6}$$

where we used the decay rate Γ from equation 4.4. The density profile depends on r, which is the distance from the differential volume to the

GC. We can observe in figure 4.4 that its dependece with the line of sight is:

$$r^2 = l^2 + d^2 - 2ld\cos(\theta) \tag{4.7}$$

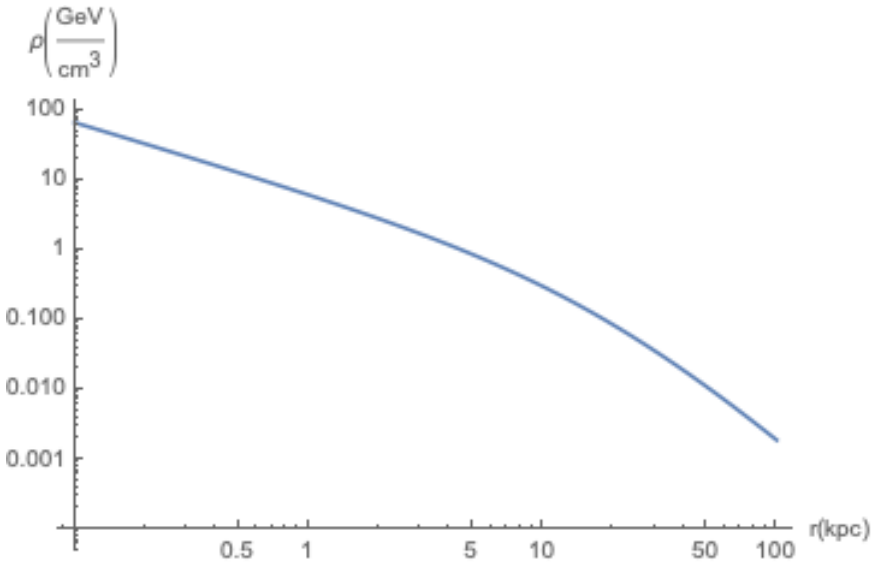

Figure 4.5: NFW profile of DM distribution through the galactic halo.

Finally, we integrate this flux over the full space using a DM density profile of the galactic halo, for example, the Navarro–Frenk–White profile (NFW) (111). Figure 4.5 illustrates this profile, which is modeled as:

$$\rho_{NFW}(r, r_S, \rho) = \frac{\rho}{(\frac{r}{r_S})(1+\frac{r}{r_S})^2}, \tag{4.8}$$

where $r_S = 20$ kpc is a scale radius determined from simulations in (112; 113).

Figure 4.7 shows the flux of incoming photons in a telescope depending on the pointing direction defined by the angle α, where $\alpha = \pi/2$ means that it is pointing towards the GC. Although the GC is a powerful source, it has a significant background. Figure 4.8 shows the background composed of all X-ray flux from non-DM origin; it includes emissions from low mass X-ray binaries; cosmic X-ray; thermal components from the galactic diffuse background and ionized neutral atoms from the interstellar medium. Reference (109) estimates

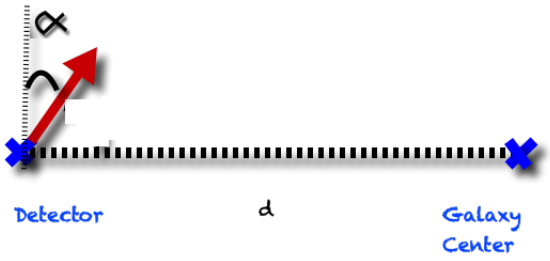

Figure 4.6: Definition of the pointing angle α

the background using results from Suzaku observations of the Galactic Ridge and GC to estimate the contribution from diffuse thermal emission (114); ASCA observations to contribute with the cosmic X-ray background from unresolved extragalactic sources (115); and the ROSAT All-Sky Survey – Bright Source Catalogue (92) to estimate the contribution from point sources in the field.

For an energy of 3.5 keV, the background flux is approximately $\phi_B = 4.6$ cm^{-2}s^{-1}keV^{-1} as shown in figure 4.8. Therefore, we estimate the time necessary to accumulate data until achieving five sigma significance

$$S = \frac{N_\gamma}{\sqrt{N_B}}, \tag{4.9}$$

where the new physics number of events is

$$N_\gamma = \phi_\gamma \Delta A \Delta t, \tag{4.10}$$

and the background number of events is

$$N_B = \phi_B E_\gamma \Delta A \Delta t. \tag{4.11}$$

We may estimate the time using the CCD treshold energy

$$E_\gamma = 0.003 \text{ keV}, \tag{4.12}$$

and the flux coming from DM decay $\phi_\gamma = 0.033 s^{-1}$ per unit of detector area. Therefore, the exposure time for a 5σ signal is of 307 seconds, approximately 5 minutes.

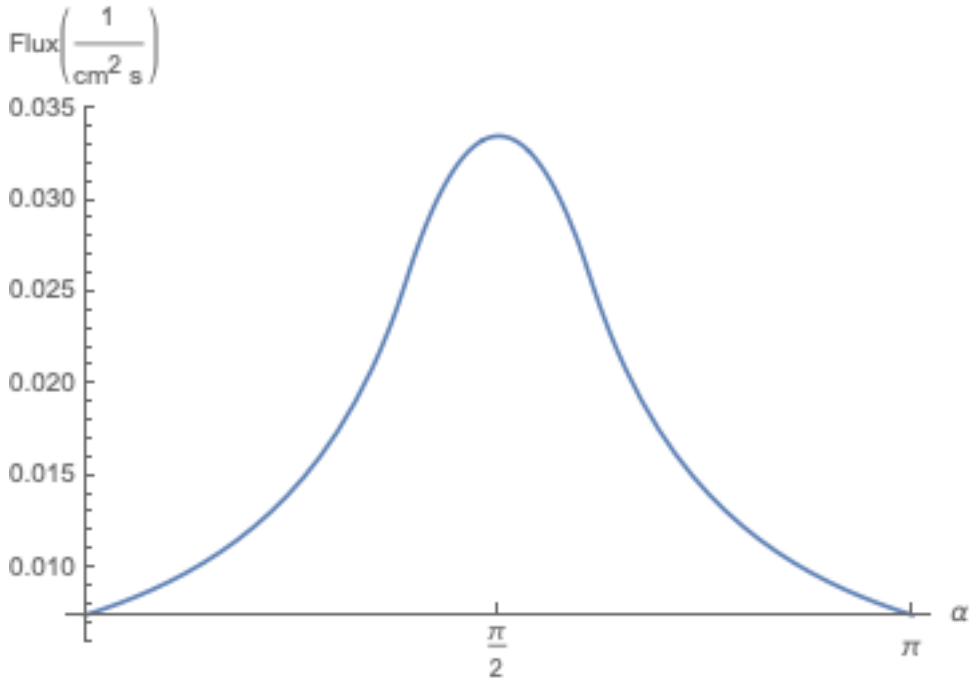

Figure 4.7: Flux of incoming photons with $m_s = 7$ keV depending on the pointing angle α, where $\alpha = \frac{\pi}{2}$ when the satellite is pointing directly to the GC.

In conclusion, the new telescope is sensitive enough to probe the excess in the 3.5 keV line from the XMM-Newton observations of the Perseus cluster and the Andromeda galaxy. A sterile neutrino decay could explain this effect. We also supposed that the number density is supposed to be the DM NFW profile. In this case, the new skipper CCD satellite with a $\theta = 20^o$ opening angle would only need five minutes to have a significant signal when pointing directly to the GC. Therefore, this experiment will improve the sensitivity to x-ray probing the hypothesis that DM can be composed of 7 keV sterile neutrinos.

4.4 Eletromagnetic dipole effective Lagrangian

One of the most remarkable characteristic of Dark Matter is its feeble interaction with light. Cosmological observations put strict bounds on the coupling of DM candidates and photons. However, it is possible to have a model that generates a dipole interaction through a higher-order operator suppressed by a significant energy scale. In particular, we have consider a model where the DM candidate (χ_1) has a nearby

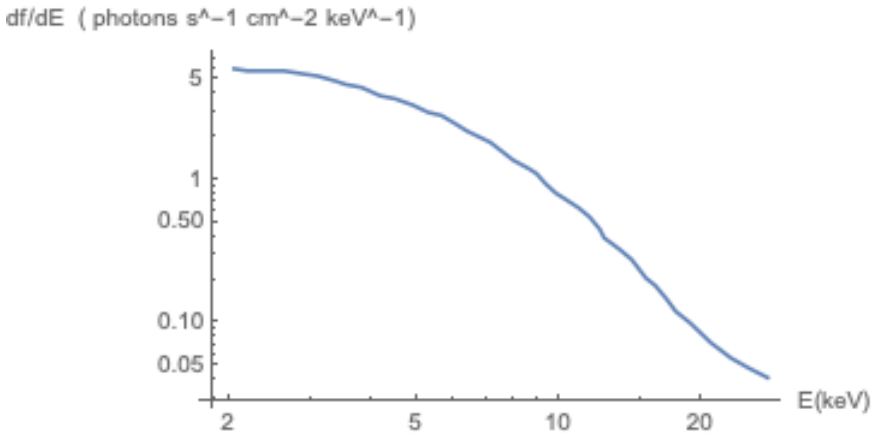

Figure 4.8: Background X-ray flux from the GC produced from non DM sources. The energy bins are 3 eV wide. (109).

excited state χ_2 coupled to the effective Lagrangian:

$$\mathcal{L} = \frac{-i}{2}\bar{\chi_2}\sigma_{\mu\nu}\frac{(a+b\gamma_5)}{M}\chi_1 F^{\mu\nu}, \tag{4.13}$$

which describes the interaction of the two fermions χ_1 and χ_2 with the EM field tensor. The energy scale M supresses the couplings a and b. Moreover, χ_1 is a long-lived DM candidate, while χ_2 excited state is more massive than χ_1, which allows the decay $\chi_2 \to \chi_1\gamma$.

We are going to consider two possible scenarios where the new fermions generate distinct signals in an X-ray telescope. The first is a resonant scattering between photons and DM from a source (104). Meanwhile, the second hypothesis assumes that χ_1 scatters with a nucleus inside Earth, resulting in an excited state χ_2 that decays back into $\chi_1\gamma$ towards the detector. This was calculated for direct detection experiments in references (116; 117).

The first scenario is X-ray resonant scattering. We assume that photons can scatter with the fermion χ_1 through the resonant fermion χ_2, as illustrated by the diagram 4.9a. In reference (104), Profumo et al. propose a dark line spectrum from this process. They describe a dip in the incoming flux of photons localized at the resonant energy. The phenomena would happen because a small portion of the flux would be deflected away from its original path, as shown in figure 4.9b. On the other hand, this calculation was made considering the narrow FOV of the existing telescopes. For a large opening angle, there will also be the contribution of scattered photons into the detector generating an excess, which may be dislocated from the resonant

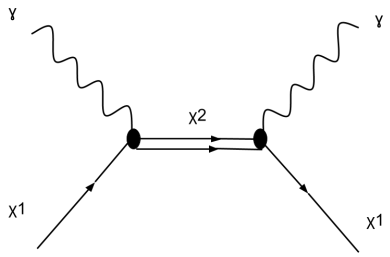

(a) $\gamma\chi_1$ scattering process.

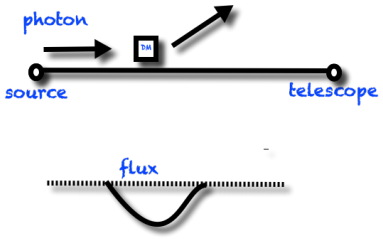

(b) Photons scattered out of the detector generating an absorption pattern.

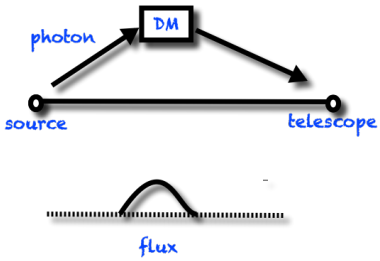

(c) Flux of incoming photons that will produce a resonance signal.

Figure 4.9: The figure (a) is a Feynman diagram representing the scattering process generated by the interaction of the effective Lagrangian in 4.13. The next two diagrams represent the two possible signals in the telescope. First, the incoming photons are deflected away, which produces an absorption line. Second, photons are scattered into the detector producing a resonance.

energy, as represented in figure 4.9c.

The scattered photon would be characterized by the resonant energy E_{res} in the center of mass (CM) frame, which is given by:

$$E_{res} = \frac{m_2^2 - m_1^2}{2m_1}, \tag{4.14}$$

where and $m_{1,2}$ is the $\chi_{1,2}$ mass. This allows a broad parameter space, which is determined by the detector energy scale and the ratio $R = \frac{m_1}{m_2}$, with $0 < R < 1$. For a typical CCD X-ray telescope reach, the energy range that can be detected is between 0.1 to 15 keV, which restricts the parameter space as shown in figure 4.10. However, cosmological bounds further restrict the parameter space. According to reference (104), the most stringent limits come from: red giants, Lyman-α forest

data, Super Nova events and BBN. Large scale structure formation from Lyman-α forest data implies that the smallest possible mass for DM restricts $m_1 \gtrsim 10$ keV (118). This bound restrict the parameter space in figure 4.10 to only values above the dashed green line, which corresponds approximately to $R > 0.5$.

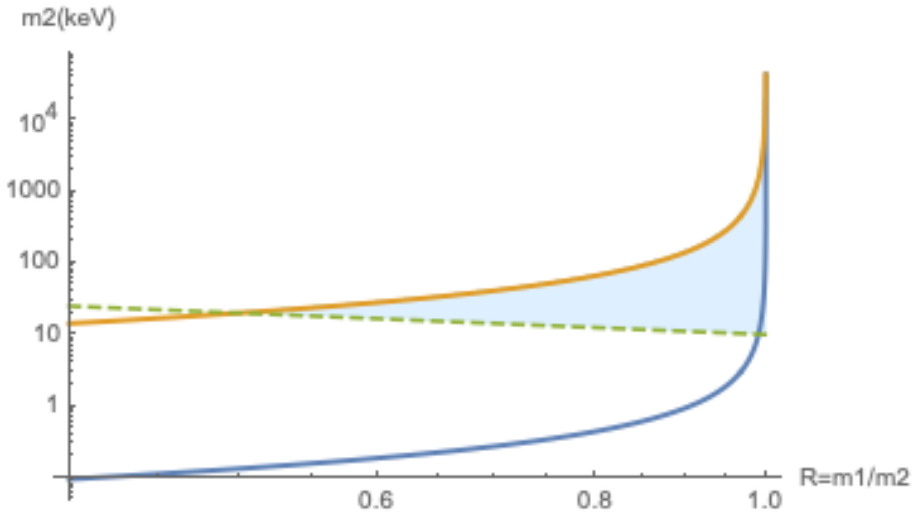

Figure 4.10: Parameter space m_2 in terms of $R = \frac{m_1}{m_2}$. The blue and orange full lines show the fermionic masses that can be probed by the detector's energy range at 0.1 and 15 keV respectevely. The dashed line corresponds to the Lyman-α bound of $m_1 > 10$ keV. Thus the shaded area corresponds to the allowed parameter space that will be probed by the skipper CCD telescope.

Moreover, the effective Lagrangian coupling in equation 4.13 must be highly supressed in order to respect the astrophysical constraints. For this purpose, we define the parameter $\tilde{M}$ as:

$$\tilde{M}^2 = \frac{\pi M^2}{|a|^2 + |b|^2}, \tag{4.15}$$

and the parameter $\eta = \frac{m_2}{\tilde{M}}$. One cosmological process to consider is to avoid excessive energy loss in stars.

Mainly $\chi_1\chi_2$ pair production in plasma decay can delay the helium ignition in low-mass red giants. It can be translated to the bound:

$$m_2 \lesssim \frac{2\omega_P}{(1+R)} \tag{4.16}$$

where the plasma frequency is $\omega_P \approx 8.6$ keV (119; 120) and

$$8 \times 10^{-31} \lesssim R\eta^2 \lesssim 2 \times 10^{-19}. \tag{4.17}$$

Furthermore, data from Super Nova SN 1987A event with core plasma frequency $\omega_P \approx 10$ MeV restrict $m_2 \lesssim 2\omega_P/(1+R)$ (120) and

$$2 \times 10^{-21} \lesssim R\eta^2 \lesssim 2 \times 10^{-17}. \tag{4.18}$$

Finally, BBN also restrict the parameter space since it is sensible to the number of degrees of freedom in the ealy universe. The fermions $\chi_{1,2}$ can contribute to the total energy density and expansion rate if they are in thermal equilibrium before the nucleosynthesis (119). This implies that $m_2 \lesssim 2(1MeV)/(1+R)$ and

$$R\eta^2 \lesssim 2 \times 10^{-20}. \tag{4.19}$$

To sum up, the lower bound is taken from supernova and upper bound from BBN:

$$2 \times 10^{-21} \lesssim R\eta^2 \lesssim 1.7 \times 10^{-20}. \tag{4.20}$$

Figure 4.11 shows the allowed parameter space. The horizontal lines are the bounds from supernova and BBN, while the diagonal lines correspond to $R = 0.5$, 0.9, and 0.99. Reference (104) also states that there are bounds from EW precision tests and accelerators, but cosmological bounds are more restrictive constraints to the parameter space.

4.4.1 Dark Line

Firstly, we are going to calculate the absorption patter in figure 4.9b. In this one-dimensional scenario, the incoming X-ray flux is deflected from its path, generating a dip on the total flux. This calculation is reproduced from reference (104). It is a reasonable assumption for narrow FOV telescopes, such as Chandra and XMM-Newton. However, the signal in the large FOV telescope has the contribution of X-rays that are scattered towards the detector.

Considering the possible parameter space, we have chosen 3 points to evaluate the X-ray incoming flux. Fixing the resonance energy at 15 keV, we choose to evaluate points A, B and C, which are described in table 4.3. It is possible to fix the fermion masses that respect the telescope sensitivity in figure 4.10. Meanwhile the scale $\tilde{M}$ must respect the cosmological bounds in equation 4.20, which is represented in figure 4.11

	R	m_1 (keV)	m_2 (keV)	$\tilde{M}$ (keV)
A	0.5	10	20	10^{10}
B	0.9	128	142	10^{12}
C	0.99	1477	1492	10^{13}

Table 4.3: Points A, B and C with $E_{res} = 15$ keV.

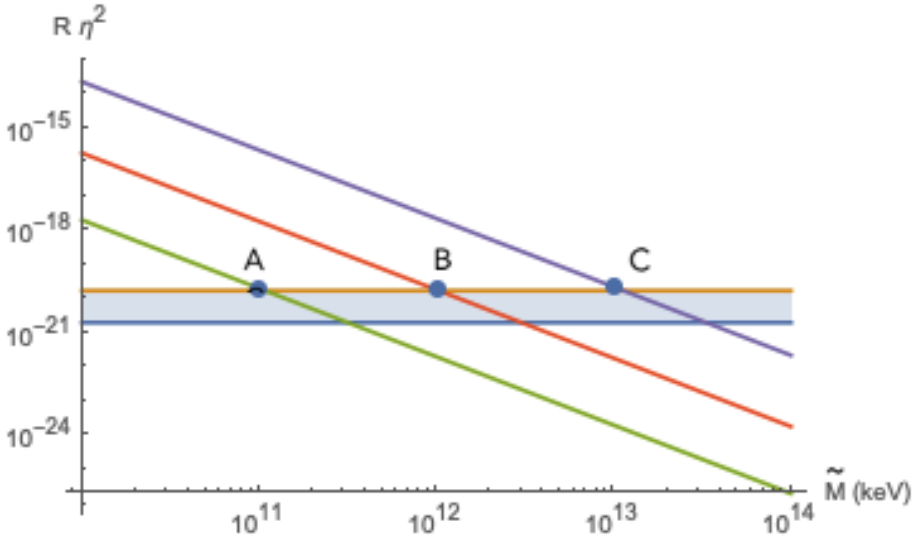

Figure 4.11: Parameters $R = m_1/m_2$ and $\eta = m_2/\tilde{M}$ in terms of the cutoff energy $\tilde{M}$. The shaded area corresponds to the allowed parameter space considering cosmological bounds. The horizontal lines are the most strict bounds from Super Nova and BBN in equation 4.20, while the diagonal lines corresponds evaluating points A, B and C without fixing $\tilde{M}$, which are chosen in the dots such that the scale is minimum.

The interaction of the two fermions with the photon is given by the dipole Lagrangian in equation 4.13. To calculate this process cross section, we assume a narrow resonance process in the diagram 4.9a, which is described as the Breit-Wiegner cross section in the CM frame:

$$\sigma_{\gamma\chi_1} = \frac{2\pi}{2p_{CM}^2} \frac{(m_2\Gamma_{\chi_2})^2}{(s-m_2^2)^2 + (m_2\Gamma_{\chi_2})^2}, \tag{4.21}$$

where p_{CM} is the photon momentum and m_2 is χ_2 mass. The decay width Γ_{χ_2} is given assuming that it decays is only to $\chi_1\gamma$ final state:

$$\Gamma_{\chi_2} = \frac{1}{\tilde{M}^2} \frac{(m_2^2 - m_1^2)^3}{m_2^3}. \tag{4.22}$$

Kinematically, the photon momentum p_{CM} is calculated as:

$$p_{CM}^2 = \frac{m_1^2 - s}{4s}, \tag{4.23}$$

where $s = m_1^2 + 2E_\gamma\sqrt{p^2 + m_1^2} - p\cos\theta$ with E_γ the incoming photon energy and p the DM initial momentum.

Another DM characteristic is that it is cold. Halo DM velocity is distributed from the order of 10 km/s until 1000 km/s. It is represented by the Maxwell-Boltzman distribution with a S_v velocity dispertion:

$$f(p) = \sqrt{\frac{2}{\pi}}\frac{p^2 e^{\frac{-p^2}{2a^2}}}{a^3}, \tag{4.24}$$

with $a = m_1 S_v$. Therefore we can use equations 4.21 to 4.24 and calculate the total cross section:

$$\sigma^{TOT} = \int dp f(p) \int_{-1}^{1} d(\cos\theta)\sigma_{\gamma\chi_1}, \tag{4.25}$$

where we integrated over all possible values of the momentum p, which is estimated as $p_{min} = m_1 10$ km/s until $p_{max} = m_1 10^4$ km/s. Figure 4.12 shows the total cross sections of each point in table 4.3, for $E_{res} =$ 15 keV and $R = 0.5$, 0.9 and 0.99.

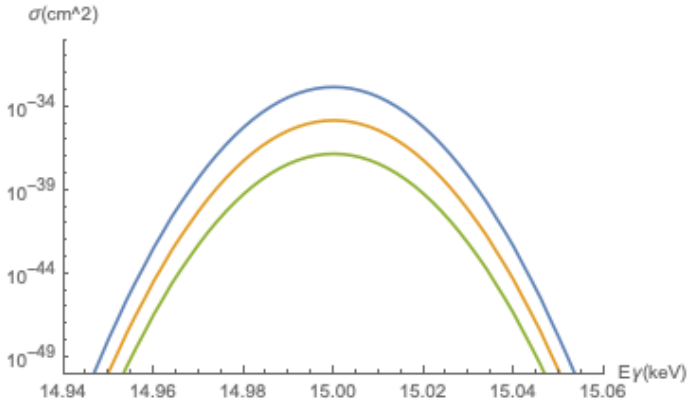

Figure 4.12: Total cross section for $E_{res} = 15$ keV. The colors green, orange and blue corresponds respectively to the points A, B, and C with $R = 0.5$, 0.9 and 0.99.

The signal may only be detected if the total cross section width is greater or comparable with the telescope energy resolution. According to reference (121), the cross section can be simplified as:

$$< \sigma >_{res} = \frac{3\pi^2}{2}\frac{\Gamma\, m_1}{E_{res}^3\, p}, \tag{4.26}$$

in the limit of $\Gamma \ll E_{res}$. Integrating in the Maxwell-Boltzman distribution of momenta p:

$$\sigma(E_\gamma = E_{res}) = \frac{3\pi^{3/2}}{\sqrt{2}}\frac{\Gamma}{E_{res}^3\sigma_v}, \tag{4.27}$$

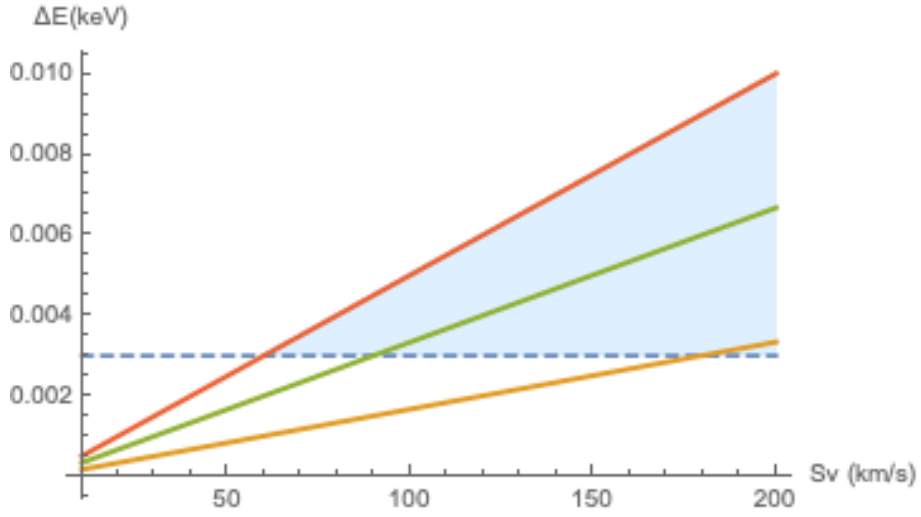

Figure 4.13: Energy width in terms of S_v average velocity, the full red, green, orange lines correspond to E_{res} = 5, 10 and 15 keV. For a skipper CCD with minimum $\Delta E \gtrsim 3$ eV, the detection is restricted to the shaded area.

where $p \simeq m_1 \sigma_v$.

The hipothesis of finding a narrow width signal, integrated over a Maxwell-Boltzmann distribution of velocities gives a well distributed cross-section. Thus the DM velocity distribution dictates the Doppler-broadened width. Therefore,it is a good approximation to parametrize the cross section as a Gaussian (121):

$$\sigma(E) = \sigma(E_{res}) exp\left[-\frac{(E - E_{res})^2}{2(\sigma_v E_{res})^2}\right] \tag{4.28}$$

Therefore, we can estimate the width to be proportional S_v is the DM escape velocity $\Delta E/E \propto S_v$, which must be comparable with the energy resolution of the detector. Figure 4.13 shows the energy width in terms of S_v for $E_{res} = 5$, 10 and 15 keV. Suppose the new skipper CCD can reach $\Delta E \sim 3$ eV, than the parameter space is restricted such $S_v > 60$ km/s at 15 keV, and limited to $E_{res} > 5$ keV.

Figure 4.14 shows the total flux of deflected incoming photons $\Delta Flux = \frac{d\phi}{dE_\gamma}$. It is normalized by an initial source flux F_0:

$$F_0 = \frac{d\phi_{source}}{dE\gamma} = \left(\frac{1 \text{ keV}}{E_\gamma}\right)^2 \frac{d\phi_0}{dE\gamma}. \tag{4.29}$$

This result is obtained by integrating the initial flux with the probability of interaction

$$P = 1 - e^{-\sigma n l} \tag{4.30}$$

where σ is the total cross section given by equation 4.25,the DM number density is $n = \rho/m_1$, and l is the line of sight distance. In this case, we assume an isotropic DM density of $\rho_0 = 0.34$ GeV/cm^3. Besides, we used the main velocity in the galactic halo as $S_v \sim 120$ km/s (122).

The resultant absorption pattern is the total flux subtracted with $\Delta Flux/F_0$. However, $\Delta Flux/F_0$ is much smaller than the initial flux for this energy range $F_0 \sim 4\,10^{-3} d\phi_0/dE$ to be represented in a single figure. Although the signal will have a width large enough for the energy resolution of the skipper CCD, the absorption pattern flux is at most a fraction on order 10^{-9} of the source F_0, which gives the number of incoming photons.

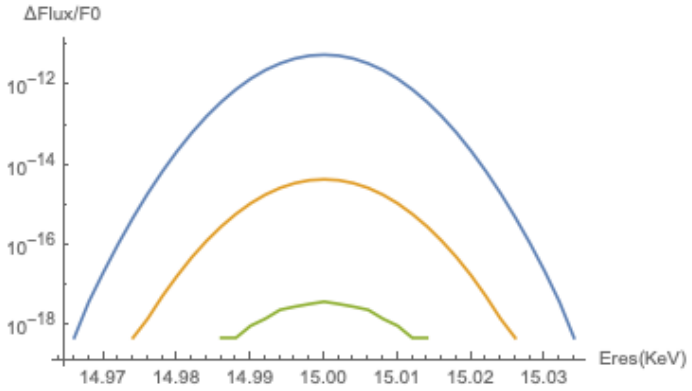

Figure 4.14: Flux of deflected incoming photons. The colors green, orange and blue corresponds respectively to the points A, B, and C with $R = 0.5$, 0.9 and 0.99.

We have observed that the narrow cross-section gains a significant width after considering the velocity distribution. Figure 4.13 shows that the total width is directly proportional to the S_v. Therefore, we observe that to have a signal with the detector energy resolution; we should have the resonant energy $E_{res} > 5$ keV and $S_v > 60$ km/s. The total flux for $E_{res} = 15$ keV and $S_v > 60$ km/s is at most order 10^{-12} of the incoming source flux F_0. However, the number of incoming X-rays from the GC source at 15 keV $F_0 \sim 0.2$ photons per second per area per energy. Using a similar calculation from equation 4.9, to have a significant signal S=5 in 1 cm^2 detector, it would take order 10^14 s. Therefore, it is not possible to obtain a significant absorption signal with the new telescope, assuming an isotropic distribution of dark matter and pointing to the GC. The Coma cluster is also a possible source of X-rays. However, Chandra measurements are in the range of

(0.1–2.4) keV, which also escapes the detector energy resolution. On the other hand, reference (104) shows how this model can be probed in gamma rays telescopes.

4.4.2 Shifted resonances

We are now going to consider the second possible signature of the X-ray resonant scattering. This process consists of the scattering of photons towards the detector, as in figure 4.9c. In this case, X-ray photons are going to add a resonance pattern in the flux located at slightly smaller resonance energy.

This process is calculated analogously to the previous deflected pattern. The integrated flux in the detector rest frame is normalized to the same initial source flux F_0:

$$Flux = \int d^3p f(p) \int n\sigma \frac{d^2}{r^2} F_0 F(\alpha) \frac{1}{4\pi l^2} l^2 dl (2\pi) \sin\theta d\theta, \tag{4.31}$$

where n is the dark matter isotropic number density, σ is the cross section given by equation 4.21 and $f(p)$ is the Maxwell-Boltzman distribution in equation 4.24, d is the distance to the source, r is the infinitesimal volume coordinate, l is the line of sight, and θ is the opening angle. However, the Breit-Wiegner cross section in equation 4.21 is valid at the center of mass (CM) frame. Therefore, the function $F(\alpha)$ is the angular function that characterizes the boost to the frame of the telescope. We assume χ_2 is produced unpolarized and decay back to $\chi_1\gamma$ isotropically in its frame rest. Then the angular function $F(\alpha)$ is defined as the probability of interaction over the FOV of the telescope Ω_t:

$$F_\alpha = \frac{P_{int}}{d\Omega_t} = \frac{dN_\gamma}{N_\gamma d\Omega_\alpha}, \tag{4.32}$$

where α is the outgoing photon deflection angle in relation to the incoming direction. Since the number of photons N_γ must be conserved, we have:

$$\int F(\alpha) d\Omega_\alpha = 1, \tag{4.33}$$

Therefore, by comparing equation 4.33 for both CM and the telescope frame, one finds the relation:

$$F(\alpha_\chi) = F_{cm} \frac{d(\cos(\alpha_{cm}))}{d(\cos(\alpha_\chi))}, \tag{4.34}$$

which is normalized to a constant $F_{cm} = 1/(4\pi)$ at the CM frame. Here, α_{cm,χ_1} is the deflected angle of the outgoing photon at the CM and the detector rest frame respectively. Furthermore, β is the relative velocity between the two frames given by the Lorentz transformation. Figure 4.15 represents the boost from CM to the χ_1 frame rest. For the outgoing photon, the boost is taken in the z direction, such that it will affect the z component of the photon momentum. However, the parallel direction x should be invariant:

$$E = \gamma(E_{cm} - \beta p_{cm}), \tag{4.35}$$

$$P_z = \gamma(p_{z,cm} - \beta E_{cm}), \tag{4.36}$$

$$P_x = P_{x,cm}, \tag{4.37}$$

with $\gamma = 1/\sqrt{1-\beta^2}$ and

$$\gamma = \frac{m_1 + E_{in}}{m_2}. \tag{4.38}$$

Therefore, the relation between the two outgoing angles $\alpha_{CM,\chi}$ is obtained by calculating:

$$\cos(\alpha_\chi) = \frac{P_z}{E_{out}}, \tag{4.39}$$

Replacing equation 4.37 in the last one, we obtain:

$$\cos(\alpha_\chi) = \frac{\beta + \cos(\alpha_{cm})}{1 + \beta\cos(\alpha_{cm})}. \tag{4.40}$$

From equation 4.34 the final angular function is:

$$F(\alpha_\chi) = \frac{1}{4\pi}\frac{1-\beta^2}{1-\beta\cos(\alpha_\chi)}. \tag{4.41}$$

Moreover, the total flux in equation 4.31 can be calculated in terms of the line of sight and the opening angle θ_t, which has a geometrical relation with

$$\alpha_\chi = \arctan\left(\frac{d\,\sin(\theta)}{d\,\cos(\theta) - r}\right) \tag{4.42}$$

where d is the distance to the source and r the postion of the infinitesimal volume. We are going to integrate the flux over the line of sight, then the function r in terms of l, θ_t is given by the cosine law:

$$r = \sqrt{l^2 + d^2 - 2d\,l\cos\theta_t} \tag{4.43}$$

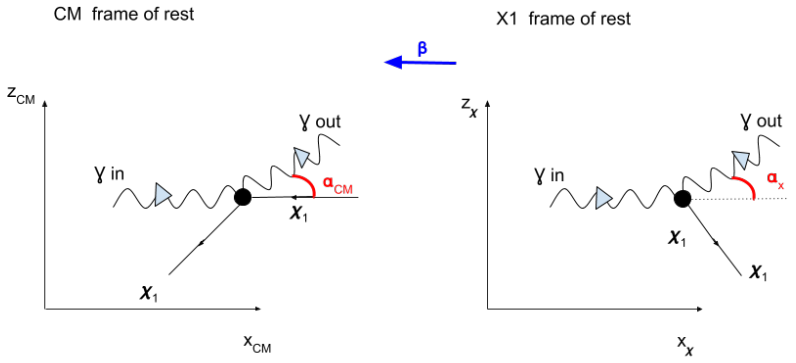

Figure 4.15: Scheme of the boost from CM to χ_1 rest frame

To sum up, we obtained the integrated flux in equation 4.31 with the Breit-Wiegner cross section in equation 4.21 boosted with the angular function 4.41. The crucial difference between this calculation and the previous absorption flux is that it does not simply depend on the incoming resonance E_{res} in equation 4.14 but on the outgoing photon energy. The kinematical energy conservation gives the incoming photon energy E_{in} in terms of the outcoming photon energy E_{out} and the angle α_χ as:

$$E_{in} = \frac{m_1 E_{out}}{m_1 - E_{out} + E_{out}\cos(\alpha_\chi)}. \tag{4.44}$$

Replacing equations 4.42 in 4.44 it is possible to calculate this energy in terms of the opening angle and line of sight:

$$E_{in} = \frac{E_{out} m_1}{-E_{out} + m1 + E_{out}\sqrt{1 - \frac{d^2 \sin\theta_t^2}{d^2 + l^2 - 2dl\cos\theta_t}}} \tag{4.45}$$

Our numerical evaluations showed that the flux is more intense around low values of θ_t, where $E_{in} \sim E_{out}$. Therefore, the width could be approximately ΔE with the second order taylor expansion of E_{in} for $\theta_t \to 0$:

$$E_{in} \approx E_{out} + \frac{d^2 E_{out}^2 \theta_t^2}{2(d-l)^2 m_1}, \tag{4.46}$$

$$\Delta E \approx \frac{d^2 E_{out}^2 \theta_t^2}{2(d-l)^2 m_1}. \tag{4.47}$$

Figure 4.16 shows the estimated energy width in terms of the mass m_1. The shaded area delimits the parameter space by taking into

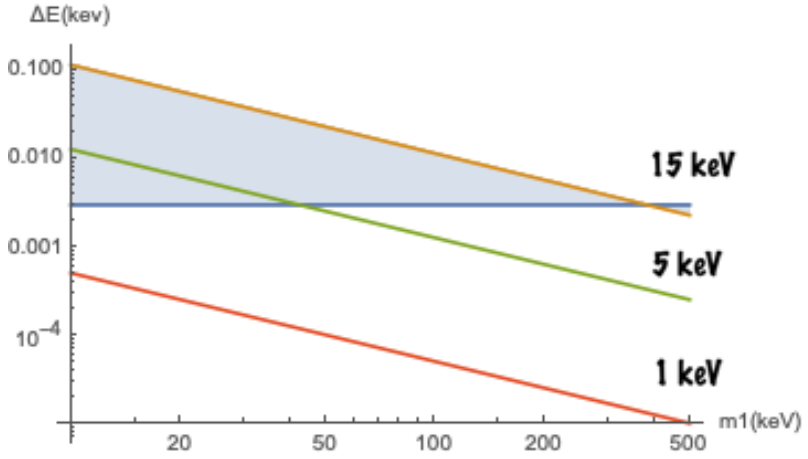

Figure 4.16: Estimated width ΔE in terms of the mass m_1 fixing $E_{res} = 1$, 5 and 15 keV, which correspond respectively to the red, green and orange lines. The horizontal line represents the detector treshold energy of 3 eV. The shaded area shows the parameter space that will be constrained by the experiment.

account the detector threshold energy of 3 eV, and the energy range from 1 to 15 keV. Therefore, in order to represent the allowed parameter space, we have chosen to calculate the flux in two specific points D and F with resonance energy of 5 and 15 keV, respectively, which are detailed in table 4.4. The choice of the points also respects the cosmological bounds in equation 4.20, as shown in figure 4.17 The complexity of the incoming energy in terms of the outgoing in equation 4.45 makes the numerical calculation hard when integrating the total flux. It will be interesting to treat this numerical problem more carefully when performing a full analysis or simulation of the data.

	E_{res} (keV)	R	m_1 (keV)	m_2 (keV)	$\tilde{M}(keV)$
D	5	0.9	42	47	5×10^{11}
F	15	0.5	10	20	2×10^{11}

Table 4.4: Chosen points D and F from parameter space to represent possible X-ray signals. In particular, $\tilde{M}$ values are chosen to obey the bounds in equation 4.20

Figure 4.18 shows the flux of photons arriving in a telescope located in Earth orbit at a distance of 8 kpc from a source with isotropic dark matter density distribution of $\rho = 0.34$ GeV/cm^3. As in the previous case, we divide the incoming flux by the source flux described in equation 4.29, which is represented by a blue horizontal line in both plots. The first plot was calculated in a set with $E_{res} = 5$ keV, $R = 0.9$, $m_1 = 42$ keV, while the second $E_{res} = 15$ keV, $R = 0.5$,

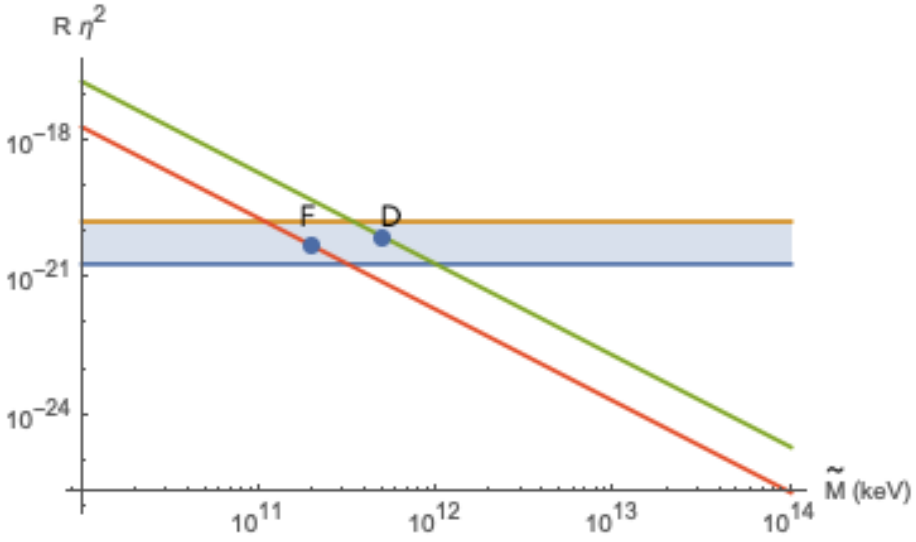

Figure 4.17: Parameters $R = m_1/m_2$ and $\eta = m_2/\tilde{M}$ in terms of the cutoff energy $\tilde{M}$. The shaded area corresponds to the allowed parameter space considering cosmological bounds. The horizontal lines are the most strict bounds from Super Nova and BBN in equation 4.20, while the diagonal lines corresponds evaluating points D and F without fixing $\tilde{M}$, which are chosen in the dots.

$m_1 = 10$ keV. Both of them show income photons flux 2 to 3 orders of magnitude greater than the source and displaced in a smaller energy range than the initial $E_{res} = 5$, 15 keV. However, the boost performed shows that the scattering angle is not isotropic, and the distribution of the estimated flux can vary one order of magnitude in each energy bin. The dispersion of the result with $E_{res} = 5$ keV shows a primary peak at $E_\gamma = 4.995$ with a order 0.01 keV width as predicted in the estimation of figure 4.16. Meanwhile the other flux spreads under the $E_{res} = 15$ keV with a maximum in $E_\gamma = 14.8$ keV and approximately width of 1.5 keV slightly larger than the previous estimation of 0.1 keV.

Assuming a source at the GC with a flux of 0.2 photons per second per area per energy. We may use equation 4.9 to estimate the time of exposure of 1 cm^2 detector with 3 eV threshold energy. For the resulting flux at 15 keV, the maximum is obtained at 0.1 times the source flux. It would be necessary 4×10^5 seconds, about five days for a five sigma significance. On the other hand, the 5 keV resonance would have the maximum flux at approximately the same order of magnitude from the source: $F_0 = 4$ photons per area per time per energy. It would take 2080 seconds to have a significant signal. Therefore, the telescope

would be sensitive to the incoming resonant excess, which is slightly shifted from its original resonance energy anisotropically in order 0.1 keV below the CM resonant energy.

4.5 Further research

Other scenarios would produce a signal in the X-ray telescope. This project will include the analysis of luminous DM (116; 117), axion detection using Earth magnetic field (106), and mirror stars (107; 108). All of them can produce X-ray emissions and probe the particle nature of DM in the telescope.

The scattering of Dark Matter particles with nuclei inside the Earth. Reference (116) proposes that the same EM dipole effective lagrangian in equation 4.13 can generate X-ray photons coming from Earth. Figure 4.19 schematizes the reaction. In this case, the fermion χ_1 scatters inelastically with a nucleus within the planet producing the excited state χ_2, which decays back into $\chi_1\gamma$ after traveling towards the detector. However, we are going to consider only the probability of χ_2 decaying only outside the Earth atmosphere, since X-rays are attenuated as they pass through matter.

This model is particular, which is to consider that the initial DM flux should vary in time and latitude (123). Assuming the DM wind comes from the direction of Cygnus, the incoming flux should vary because of the Sun motion relative to the galaxy, as shown in figure 4.20; the anisotropic rock overburden, and also anisotropic dark matter scattering angle. Furthermore, the daily rotation of the Earth causes sidereal-daily modulation of the signal. The DM signal will be evident if the daily modulation is measured, which should be able to separate it from the background. Therefore, the next step in this work is to calculate the signal produced at the skipper CCD telescope. It would be interesting if it can capture the modulated signal when pointing to the Earth.

Furthermore, other possible models would produce a signal if the telescope points towards Earth. It involves axion detection using Earth magnetic field (106). Although it is a weak strength, when integrated over the total volume, it can give a significant signal.

The final scenario is of mirror stars (107; 108). The hidden sector

model Twin Higgs (30) was discussed as a neutral naturalness scenario in chapter 2. It includes either a complete or partial copy of the SM is, which connects back to the usual SM only through Higgs portals. A hidden sector can also motivate DM models since it is possible to build hidden hadrons and atoms (31; 33; 32), and it is cosmologically viable (34). Particularly, there is a hypothesis of mirror stars, which are supposed to be a star with an SM matter nugget and the surrounding made of dark sector particles. The mixing between the SM photon and dark photon can generate an X-ray emission. (107; 108). A future calculation will analyze this scenario to estimate its signal in the skipper CCD telescope.

4.6 Conclusions

This ongoing project analyses possible scenarios in DM to estimate the new telescope sensitivity to each of them. We presented the results for the sterile neutrino decay and the resonant scattering of a fermionic DM with light. Several X-ray telescopes use CCD technology for imaging and spectroscopy, such as Chandra and XMM-Newton. An improved version of the detector called skipper CCD lowers the electronic noise significantly. It uses floating readout gates that allow measuring multiple and independent events. It is the most sensitive microcalorimeter operating above the liquid nitrogen temperature. Furthermore, the most competitive telescopes have a narrow FOV for precise astrophysics measurements. However, for indirect DM searches, it is interesting to build a new telescope with a large opening angle. Since DM interactions with light are feeble, the broad FOV allows the detector to analyze a larger volume in space and increase the number of events (109).

Both X-ray telescopes XMM-Newton and Chandra have measured a 3.5 keV line at three sigma significance. One of the most acceptable model to fit this possible signal is the relic neutrino decay. In this scenario, we suppose the 7 keV sterile neutrino decays to a photon and an active neutrino. Besides, we assumed that the NFW profile gives the DM number density. In this case, the new skipper CCD satellite with a $\theta = 20^o$ opening angle would only need five minutes to have a significant signal when pointing directly to the GC. This

experiment is sensitive to the model where DM is composed of 7 keV sterile neutrinos. Furthermore, it will improve the sensitivity to x-ray, probing the 3.5 keV line existence.

The second scenario considers the resonant scattering off DM. The interaction is given by an EM dipole effective lagrangian. This process may generate two different signals: the usual resonant excess and an absorption line (104). The latter comes from X-rays that were supposed to arrive at the detector but were deflected from its path. However, the total flux estimated for the energy range of (0.1 - 15) keV is not comparable to the X-ray source. If considering the Coma Cluster source, the absorption line will escape the detector energy resolution while the estimated flux from the GC varies between 10^{-18} to 10^{-9} of the background. Reference (104) shows how this scenario can be probed in gamma rays telescopes with narrow FOV. On the other hand, the broad opening angle adds contributions from resonant X-rays scattered towards the telescope. They have a much more significant effect, where we considered two example cases with 5 and 15 keV resonant energies. The isotropic distribution of DM can produce flux in the same order of the source for 5 keV resonance, and the 15 keV case can be ten times larger than the source flux. The GC background is of 4 and 0.2 photons per second per area per energy considering the 5 and 15 keV resonance cases. Then it would take at least 2080 or 4×10^5 seconds to have a significant signal in each case. Furthermore, this scenario signature is characterized to be shifted from the usual resonant energy. The CM rest frame produces a well-distributed dispersion in the flux around $E_{res} = \frac{m_2^2 - m_1^2}{2m_1}$. The telescope rest frame distributes the data anisotropically, and the maximum flux reached was found in order 0.1 keV below the CM resonant energy.

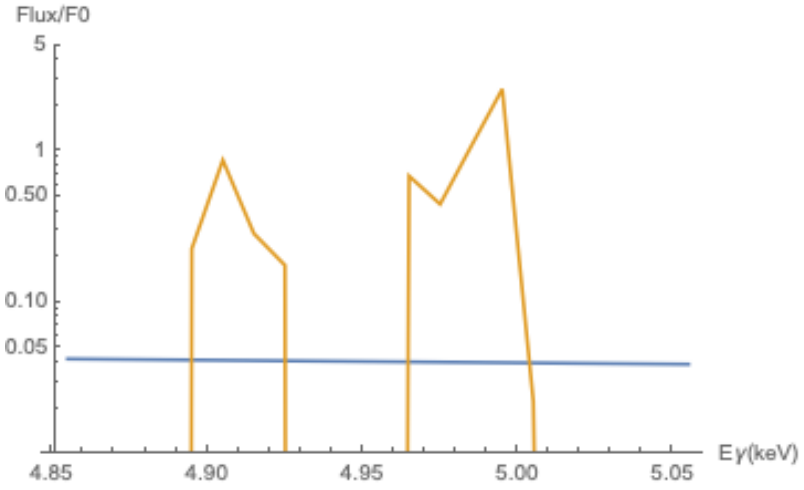

(a) Results for point D, where $E_{res} = 5$ keV, $R = 0.9$, $m_1 = 42$ keV

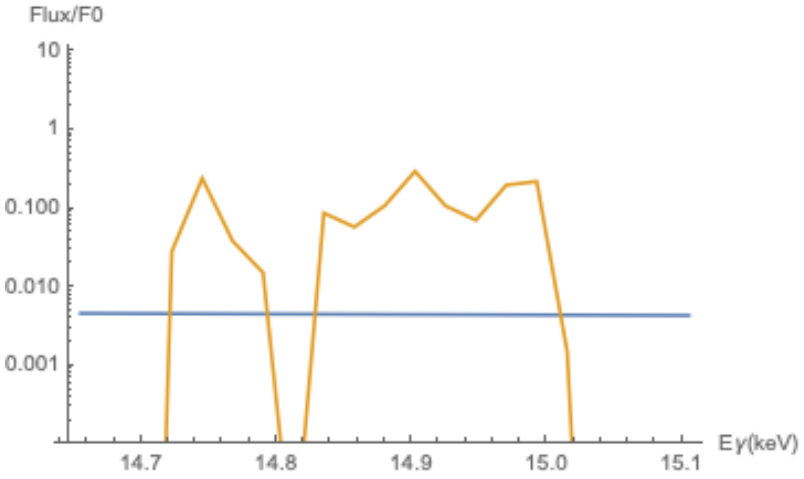

(b) Results for point F, where $E_{res} = 15$ keV, $R = 0.5$, $m_1 = 10$ keV

Figure 4.18: Normalized flux obtained from the resonant scatering towartds the detector. Assuming both points in table 4.4. The blue horizontal line in both plots represents the source flux F_0 in equation 4.29

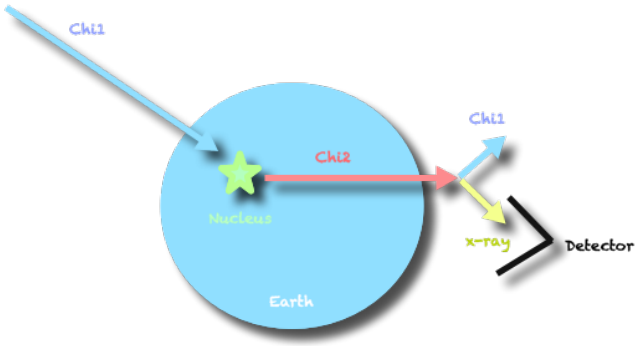

Figure 4.19: Scheme of incoming χ_1 flux scattering with a nuclei in Earth, which produces the χ_2 excited state. The later will travel outside the planet and decay back into $\chi_1\gamma$ which can be detected in an X-ray telescope.

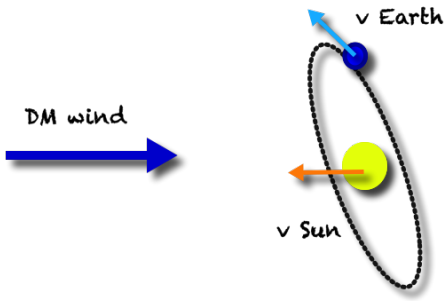

Figure 4.20: Representation of the daily modulation velocity calculation. Supposing the DM wind comes from Cygnus direction, the detection in Earth should be calculated summing the velocity with the translation movements of the planet and solar system with respect to the galaxy.

5
Conclusions

This thesis concerns the sensitivity of two different detectors to new physics. The first part shows the distribution of displaced vertices from hidden glue in the LHC, where we model the Fragmentation Function (FF) of glueballs in the Folded Supersymmetry (F-SUSY) scenario. It is a Neutral Natural (NN) realization, proposed to solve the LHP. The second part of the thesis regards DM indirect searches using a new X-ray telescope. X-ray signals constrain several DM models, including sterile neutrino decays, resonant scatterings, DM scattering within Earth, axions, and mirror stars. Curiously, the last scenario is a NN realization, where the star has SM nugget and the surrounding composed of the hidden sector particles described by the mirror Twin Higgs.

5.1 Displaced vertices at the LHC

The Hierarchy Problem (HP) has motivated most of the LHC searches for new physics. The first line of the chart in figure 5.1 shows the main BSM theories candidates to solve the HP. They present top partners that have been searched at the LHC through strong direct production. Mainly, the supersymmetric particle is the scalar stop, while composite Higgs and extra dimensions search for different fermionic states. However, stringent bounds pushed new physics to a high energy scale, giving place to the Little Hierarchy Problem (LHP). An alternative is to search for colorless top partners from a Hidden sector. NN models are presented as a solution to the LHP; it extends the SM with a new $SU(3)$ group. In this case, the top partners cannot be strongly

produced because they would be charged only under the new group.

NN includes distinct scenarios such as F-SUSY, Quirky Little Higgs, and Twin Higgs. They are organized in figure 5.1 in accordance to SM gauge charge and spin (46). F-SUSY phenomenology includes direct EW production of scalar f-stops, while Quirky Little Higgs similarly generates the fermionic colorless top partners. The Twin Higgs model includes a copy of the SM gauge group that only interacts with the usual through Higgs portals. Moreover, there is a hypothetical model with scalar singlets, which is represented with an interrogation mark(46). It does not exist an explicit theory with an SM-singlet scalar top partner. However, only a few channels would allow its discovery, which only includes Higgs-portal observables. Figure 5.1 also shows that the hidden glueballs are present in all NN phenomenology. The Twin Higgs phenomenology includes exotic Higgs decays to the glueballs. Meanwhile, pure glue objects can be produced from the direct EW production of colorless top quark partners in F-SUSY and Quirky Little Higgs. Displaced vertices in from the hidden glue characterize the NN models uniquely. We have studied the f-squark production in the LHC and modeled the hadronization of hidden glueballs.

In this work, we obtained the distribution of displaced vertices in the F-SUSY scenario. This signature arrives from the EW production of f-squarks at the LHC. After the pair of f-squarks arises, they annihilate each other to hidden gluons, which hadronizes to glueballs. We modeled the FF of hidden gluon to glueball to estimate their average multiplicity. As a result, figure 3.7 shows the multiplicity of displaced vertices along the LHC detector length. We observe that this signature is extremely sensitive to the glueball mass $M_{\tilde{G}}$. For instance, when $M_{\tilde{G}} = 15$ GeV, most of the vertices are in the last part of the detector or beyond, which can be identified with significant missing energy events. However, when increasing the mass by 5 and 10 GeV, we observe a more substantial fraction of the events distributed over the detector lengths. Therefore, it is possible to obtain multi-vertex events at any part of the detector, possibly in more than one element at the same time.

It is challenging to analyze data in search of multiple displaced vertices in different segments of LHC detectors. However, there is

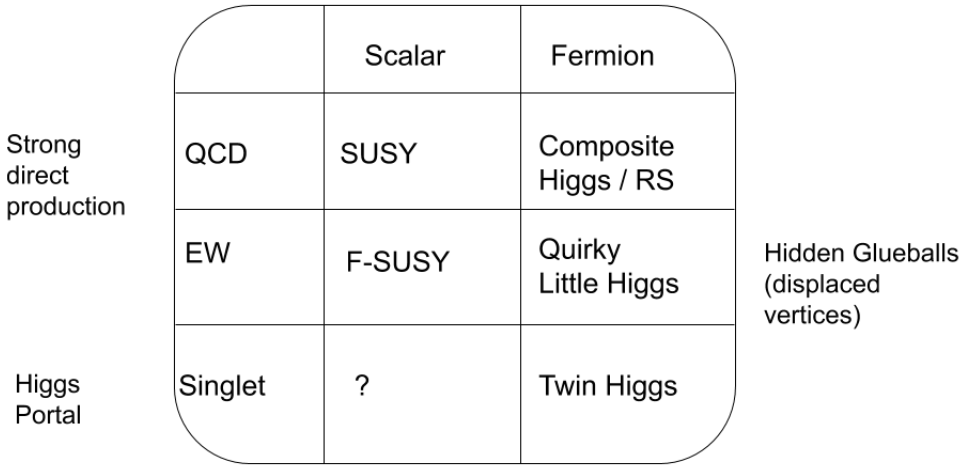

Figure 5.1: The chart organizes the theories candidates to solve the HP according to the top partner's spin and gauge interaction (46). LHC bounds restricted the strong production of new physics from SUSY, composite Higgs, and extra dimensions. However, NN models escape these bounds presenting colorless top partners. F-SUSY and Quirky Little Higgs particles can be electroweakly produced in the collider, while Twin Higgs phenomenology includes Higgs portals. A hypothetical scalar singlet model is represented as an interrogation mark. All NN models may present colorless glueballs. However, only F-SUSY and Quirky Little Higgs are characterized by the hidden glue displaced vertices. Twin Higgs phenomenology includes mirror glueballs in exotic Higgs decays.

an effort to search for long-lived particles in the LHC (69), including the proposal of a new detector called MATHUSLA (124) that would cover a more considerable distance over 100 m. However, the EW neutral current production of f-squarks escape currently displaced vertices bounds because the cross sections producing these events are below a 1fb. It is necessary to consider large luminosities to see the new physics above background. Therefore, NN exotic phenomenology will be sensitive at future colliders such as the high luminosity HL-LHC, FCC-hh, LHeC, and FCC-eh (125). Future research will analyze HL-LHC detectors simulations with better modeling of the glueballs resulting from soft f-gluon radiation in the event after f-squark annihilation (126). Furthermore, future research depends on the parton shower Monte Carlo simulation that can fix the average multiplicity at a specific energy.

5.2 Indirect searches with a new X-ray telescope

The proposal of a new telescope with a skipper CCD and broad FOV is relevant for indirect DM searches. It would be launched in a satellite in Earth's orbit, which is a relatively low-cost experiment in high energy physics. We have calculated the sensitivity of the new X-ray detector in two different scenarios: sterile neutrino decays and resonant scattering.

Several X-ray telescopes use CCD technology for imaging and spectroscopy, such as Chandra and XMM-Newton. However, there is now an improved version of the detector called skipper CCD with significantly low electronic noise. Its floating readout gates allow multiple and independent events measurements. It is the most sensitive microcalorimeter operating above the liquid nitrogen temperature. Furthermore, the most competitive telescopes have a narrow FOV for precise astrophysical measurements. However, indirect DM searches require a broad opening angle because of its weak interactions with light. The large FOV allows the detector to analyze a large volume in space and increase the number of events (109).

The first scenario we analyzed is the sterile neutrino decay, which is motivated by the 3.5 keV excess. Both X-ray telescopes XMM-Newton and Chandra have measured a 3.5 keV line at 3 sigma signif-

icance. One of the most acceptable model to fit this possible signal is the relic neutrino decay. In this scenario, we suppose the 7 keV sterile neutrino decays to a photon and an active neutrino. We also assumed that the NFW profile gives the DM number density. In this case, the new skipper CCD satellite with a 20^o opening angle would only need five minutes to have a significant signal when pointing directly to the Galactic Center (GC). Therefore, the experiment will be sensitive to the model where DM is composed of 7 keV sterile neutrinos. Furthermore, it will improve the sensitivity to x-ray, probing the 3.5 keV line existence.

The second scenario considers the resonant scattering off DM. The electromagnetic dipole effective lagrangian may generate two different signals: the usual resonant excess and an absorption line (104). The latter comes from X-rays that were supposed to arrive at the detector but were deflected from its path. However, the total flux estimated for the energy range of (0.1 - 15) keV is not comparable to the X-ray source. If considering the Coma Cluster source, the absorption line will escape the detector energy resolution while the estimated flux from the GC varies between 10^{-18} to 10^{-9} of the background. Although the X-ray telescope is not sensitive to this search, reference (104) shows how this scenario can be probed in gamma rays telescopes with narrow FOV.

On the other hand, the broad opening angle adds contributions from resonant X-rays scattered towards the telescope. They have a much more significant effect, where we considered two example cases with 5 and 15 keV resonant energies. The isotropic distribution of DM can produce flux in the same order of the source for 5 keV resonance, and the 15 keV case can be ten times larger than the source flux. The GC background is of 4 and 0.2 photons per second per area per energy, considering both resonance cases. Then it would take at least 2080 or 4×10^5 seconds to have a significant signal in each case. Furthermore, The CM rest frame produces a well-distributed dispersion in the flux around $E_{res} = \frac{m_2^2 - m_1^2}{2m_1}$. However, in the telescope rest frame, the scattering angle is not isotropic; the results were found to have an excess distributed in energies slightly lower than E_{res}. Thus this scenario signature is characterized to be shifted from the usual resonant energy.

We conclude that the new telescope can probe the two scenarios above. The sterile neutrino would need only 5 minutes of exposure time to have a significant signal, while an excess from resonant scatterings may take 7 to 35 minutes, depending on the fermionic masses. Future research will include the analysis of fermionic DM scattering through Earth, axion searches using Earth's magnetic field, and mirror star searches. However, these results also depend on assumptions on the DM density profiles. Therefore, measurements from the new telescope would give us information not only about the particle nature of DM but also probe DM characteristics such as its mass density distribution.

Appendices

A

Supersymmetry

The Hierarchy Problem (HP) is a hint for new physics at TeV scale. Many theories are candidates as solutions, protecting the Higgs mass from radiative corrections. The two most commons solutions of the HP are supersymmetric extensions and composite Higgs models. In supersymmetry (SUSY) the Higgs is an elementary scalar, there is a global symmetry imposing a transformation between fermions and bosons that generates superpartners to the SM particles. SUSY solves the HP in a natural way and the Higgs mass is automatically protected when included counterterms corrections from scalar superpartners. In composite Higgs models, the Higgs is a pseudo Nambu-Goldstone boson from the spontaneous breaking of a global symmetry, analogous to the pion in QCD.

However, bounds on LHC have been pushing the scale of new physics to a few TeV scale, which is higher than expected, generating a small fine tuning. Colorless Top Partners models are presented to avoid the Little Hierarchy Problem (LHP). This class of theories contains SM plus an extra color group linked with a parity symmetry. New particles won't interact strongly with SM, which explains why they have not been found, yet they still can lay between EW and TeV scale. This work will treat the phenomenology of F-SUSY, a Colorless Top Partner model daughter from supersymmetric theories. This chapter explains some concepts well stablished from SUSY, necessary to understand the F-SUSY scenario.

A.1 Supersymmetry

Supersymmetric extensions of the SM can be used to solve the HP. For a review one may read references (127) and (128). The minimal supersymmetric standard model (MSSM) describes all SM particles plus their superpartners. All fermions have a scalar partner, which are called sfermions of sleptons and squarks. The supersymmetric partners are represented with a tilde eg: $\tilde{e}_L$, $\tilde{e}_R$ a are selectrons, superpartners of left and right handed electrons respectively. Gauge bosons transform in an adjoint representation, its conjugated state is the same as the boson, so their fermionic partners must have equal left-right representations. In the MSSM, gauge bosons will also have gauginos fermionic partners: SU(3) gluinos, $SU(2) \times U(1)$ winos and binos before EWSB, then after there are zino and photino.

Higgs supermultiplets have two copies in a supersymmetric theory. This is because only one Higgsino will not cancell anomalies. Also, since the superpotential must be holomorphic, the Higgs chiral superfield cannot be complex conjugate to give masses to down and up type fermions. Therefore we need both Higgs H_u and H_d. So there are two supermultiplets with $Y = \pm\frac{1}{2}$. : H_u with $Y = \frac{1}{2}$, couples to the up quark in the yukawa interaction, and have electric charges (H_u^+, H_u^0), $T_3 = (\frac{1}{2}, -\frac{1}{2})$; H_d with $Y = -\frac{1}{2}$, couples to the down quark in the yukawa interaction, and have electric charges (H_d^0, H_d^-), $T_3 = (\frac{1}{2}, -\frac{1}{2})$.

Superpartners have the same couplings and masses as the SM particles. However, since the selectron particle has not been detected, this indicates that SUSY must be broken as a mechanism to generate masses for the superpartners. In the MSSM, the symmetry is softly broken by adding a term to the lagrangian:

$$\mathcal{L}_{SUSY} + \mathcal{L}_{soft}. \tag{A.1}$$

The soft term generates a mass m_{soft} that contributes to the higgs mass quantum corrections as:

$$m_H^2 = m_{soft}^2 \frac{\lambda}{16\pi^2} ln \frac{\Lambda_{UV}}{m_{soft}}, \tag{A.2}$$

where λ is schematic for dimensionless couplings to the Higgs. This means that the Higgs mass is sensitive to the MSSM simmetry breaking scale. Since the LHC has found a light Higgs, this scale cannot

be too high. However, the LHC has not found any supersymmetric partner, so the MSSM itself became fine tuned.

A.1.1 Algebra

SUSY is an extention of Poincaré group. It describes any particle plus its superpartner with different spin. SUSY is represented by the algebra operators Q_S, $Q_S^\dagger$:

$$Q_S|fermion\rangle = |boson\rangle \tag{A.3}$$
$$Q_S|boson\rangle = |fermion\rangle, \tag{A.4}$$

where Q_S, $Q_S^\dagger$ have spin $\frac{1}{2}$. Note that SUSY is a simmetry in the space-time. It obeys the algebra of commutators:

$$\{Q_S, Q_S^\dagger\} = P^\mu, \tag{A.5}$$
$$\{Q_S, Q_S\} = \{Q_S^\dagger, Q_S^\dagger\} = 0 \text{ and} \tag{A.6}$$
$$[P^\mu, Q_S] = [P^\mu, Q_S^\dagger], = 0 \tag{A.7}$$

where P^μ is the particle's quadrimomentum, curly braces represent anti-commutators and squared brackets are commutators. The supersymmetric irreducible representation can be described as a supermultiplet containing both bosonic and fermionic states. If $|\Omega\rangle$, $|\Omega'\rangle$ are states with different spin, member of a same supermultiplet, then both states can be written in terms of Q_S, $Q_S^\dagger$ operators, its eigenvalues are propotional to P^2, so both particle and superpartner have the same masses. Q_S, $Q_S^\dagger$ commute with gauge generators, which means that both states also carry the same coupling, such as electric charge, isospin and color.

Another important formalism used in supersymmetric theories is the Weyl fermion representation. Writing a Dirac spinor Ψ_D as:

$$\Psi_D = \begin{pmatrix} \xi_\alpha \\ \chi_{\dot{\alpha}}^\dagger \end{pmatrix}, \tag{A.8}$$

the left-handed Weyl spinor corresponds to ξ_α , while $\chi_{\dot{\alpha}}^\dagger$ is the right handed Weyl spinor indicated by a dotted index $\dot{\alpha}$. A Weyl representation explicitates the helicity of each state, which is easily observed

due to the projection of the dirac spinor. Note that the hermitian conjugate of a left handed Weyl fermion is a right handed Weyl spinor and vice versa.

The number of bosons must be the same as the number of fermions. It is straightforward to demonstrate it if one observes the operator $(-1)^{2s}$, where s is spin eigenvalue, so that it takes the value of $+1$ for bosons and -1 for fermions. The completeness relation $\sum_i |i\rangle\langle i| = 1$, then results in:

$$\sum_i \langle i|(-1)^{2s} P^\mu |i\rangle = 0. \tag{A.9}$$

Since this sum is proportional to number of bosons minus number of fermions, then they must be equal.

The simplest supermultiplet is called chiral supermultiplet, composed by a Weyl fermion, which has two helicities ($n_F = 2$), and two real scalars ($n_B = 2$). For a spin 1 boson ($n_B = 2$), it must have one fermionic superpartner ($n_F = 2$).

SUSY are characterized by the number (N) of supercharges Q_S. *N=1* SUSY corresponds to one charge operator Q_S, *N=2* correspond to two of them and so on. In subsection A.1.4 shows that a five dimensional supersymmetric theory corresponds to a *N=2* SUSY spectrum in terms of four dimensional fields.

A.1.2 Wess-Zumino Model

The simplest non interacting supersimmetric model describes a chiral supermultiplet, with a single left handed two component Weyl fermion ψ and its superpartner complex scalar ϕ. The lagrangian can be separated with a fermionic and a scalar term:

$$\mathcal{L} = \mathcal{L}_{scalar} + \mathcal{L}_{fermion}. \tag{A.10}$$

This is a Wess-Zumino Lagrangian, written as:

$$\mathcal{L}_{scalar} = \partial^\mu \phi^* \partial_\mu \phi, \tag{A.11}$$

And

$$\mathcal{L}_{fermion} = i\psi^\dagger \bar{\sigma}^\mu \partial_\mu \psi. \tag{A.12}$$

It must be invariant under supersymmetric transformations, transforming the scalar field in the fermionic and vice versa.

$$\delta\phi = \epsilon\psi, \qquad \delta\phi^* = \epsilon^\dagger\psi^\dagger, \tag{A.13}$$

$$\delta\psi_\alpha = -i(\sigma^\mu\epsilon^\dagger)_\alpha\partial_\mu\phi, \quad \delta\psi^\dagger_{\dot{\alpha}} = i(\epsilon\sigma^\mu)_{\dot{\alpha}}\partial_\mu\phi^*, \tag{A.14}$$

where ϵ is two component Weyl fermion infinitesimal parameter. However, the lagrangian in equations (A.11) and (A.12) summed is not invariant under the supersymmetric transformations above. In order to close the algebra off-shell, one must introduce an auxiliary field F,

$$\mathcal{L}_{auxiliar} = F^*F. \tag{A.15}$$

The dimensions of F is mass squared, and its SUSY transformation rules are:

$$\delta F = -i\epsilon^\dagger\bar{\sigma}^\mu\partial_\mu\psi, \quad \delta F^* = i\partial_\mu\psi^\dagger\bar{\sigma}^\mu\epsilon. \tag{A.16}$$

The auxiliary field motion equation is $F = F^* = 0$, so the lagrangian has 4 degrees of freedom on-shell, two from the scalar field plus another two from fermion. However off-shell fermions fields ψ have four degrees of freedom, thus the auxiliary field F with two degrees of freedom is used to conserve the number of bosons summed with the two ψ scalar fields. Therefore, the non interacting supersymmetric lagrangian for a collection of chiral supermultiplets is

$$\mathcal{L}_{free} = -\partial^\mu\phi^{*i}\partial_\mu\phi_i + i\psi^{\dagger^i}\bar{\sigma}^\mu\partial_\mu\psi_i + F^{*i}F_i. \tag{A.17}$$

Interactions in the lagrangian may be introduced in the most general way as:

$$\mathcal{L}_{int} = \left(-\frac{1}{2}W^{ij}\psi^i\psi_j + W^iF_i + x^{ij}F_iF_j\right) + \text{c.c.} - U, \tag{A.18}$$

where W^{ij}, W^i, x^{ij} and U are polynomials in the scalar fields, besides c.c. stands for complex conjugate. However, the terms U and x^{ij} are not invariant under supersymmetric transformations, so they cannot exist in $\mathcal{L}_{int}$. Thus the final interaction lagrangian must be:

$$\mathcal{L}_{int} = \left(-\frac{1}{2}W^{ij}\psi^i\psi_j + W^iF_i\right) + c.c., \tag{A.19}$$

The term W^{ij} is a polynomial of scalar fields with dimension of mass. It can be written in terms of the matrix mass term M^{ij} and a yukawa coupling y^{ijk} between the scalar and two fermions:

$$W^{ij} = M^{ij} + y^{ijk}\phi_k. \tag{A.20}$$

Defining the superpotential as W:

$$W^{ij} = \frac{\delta^2}{\delta\phi_i\delta\phi_j}W, \tag{A.21}$$

then the superpotential is the object:

$$W = \frac{1}{2}M^{ij}\phi_i\phi_j + y^{ijk}\phi_i\phi_j\phi_k. \tag{A.22}$$

The term W^i is defined from the superpotential as:

$$W^i = \frac{\delta}{\delta\phi_i}W = \frac{1}{2}M^{ij}\phi_j + y^{ijk}\phi_j\phi^k. \tag{A.23}$$

It is possible now to write supersymmetric interactions of the chiral supermultiplet. For a more detailed description one may read references (127) and (128).

A.1.3 Supersymmetric Gauge Theory

A gauge supermultiplet is composed of a massless gauge boson A^a_μ and a two component Weyl fermion gaugino λ^a, where a is the number of generator in the adjoint representation of the gauge group. The gauge transformation is written as:

$$A^a_\mu \to A^a_\mu + \partial_\mu\Lambda^a + gf^{abc}A^b_\mu\Lambda^c, \tag{A.24}$$

$$\lambda^a \to \lambda^a + gf^{abc}\lambda^a\Lambda^c. \tag{A.25}$$

Analogous to the auxiliary field F introduced in the free lagrangian, for a gauge lagrangian to be invariant under gauge transformations, there must be a real bosonic auxiliary field D^a. It must satisfy the equation of motion $(D^a)^* = D^a$ and has dimensions of $mass^2$. Thus the gauge lagrangian is written as:

$$\mathcal{L}_{gauge} = -\frac{1}{4}F^{a\mu\nu}F^a_{\mu\nu} + i\lambda^{\dagger a}\bar{\sigma}^\mu\Delta_\mu\lambda^a + \frac{1}{2}D^aD_a, \tag{A.26}$$

where the Yang-Mills strength tensor is:

$$F^a_{\mu\nu} = \partial^\mu A^a_\nu - \partial_\nu A^a_\mu + g f^{abc} A^b_\mu A^c_\nu. \tag{A.27}$$

The covariant derivative of the gaugino field is:

$$\Delta_\mu \lambda^a = \partial_\mu \lambda^a + g f^{abc} A^b_\mu \lambda^c \tag{A.28}$$

A.1.4 Extended SUSY

The minimal supersymmetric SM is a four dimensional supersymmetric theory that can be constructed with one operator Q_S ($N = 1$). In four dimmensions, the maximum extension of a supersymmetric model is $N = 4$, with 16 conserved supercharges. Section 61 of Shifman's book (129) describes extended SUSY for $N = 2$ and $N = 4$. It is interesting for this work to understand the extension of $N = 2$ SUSY because it will be described in five dimensions, to achieve the same spectrum of a four dimensional $N = 1$ theory.

First, lets consider massive particles in $N = 2$ SUSY extension. Suppose they are at a rest referential such as $P_\mu = (m, 0, 0, 0)$. They are going to be written in a SO(3) spin representation. Suppose that a state $|j\ jz\rangle$ with spin j and $(2j + 1)$ quantum numbers j_z. The extended superalgebra is:

$$\{Q^I_{S\alpha}, (Q^J_{S\beta})^\dagger\} = 2m\delta_{\{\alpha\beta\}}\delta^{\{IJ\}} \tag{A.29}$$

$$\{Q^I_{S\alpha}, Q^J_{S\beta}\} = 0, \tag{A.30}$$

where I, J is equal to 1 or 2.

Suppose the massive particle is at a state $|j\ jz\rangle$, assuming that $Q^I_{S\alpha}|j\ jz\rangle = 0$. It it possible to construct $2^{2N}(2j + 1)$ states from 4 annihilation and 4 creation operators. If the initial state $|j\ jz\rangle$ has spin 0, then 2^{2N} states will exist with spin either 0, $\frac{1}{2}$ or 1.

The massless states will be described in a referential such $P_\mu = (E, 0, 0, E)$. In this case, the algebra is described as:

$$\{Q^1_{S\alpha}, (Q^2_{S\beta})^\dagger\} = 4E\delta^{\{IJ\}} \begin{bmatrix} 1 & 0 \\ 0 & 0 \end{bmatrix}, \tag{A.31}$$

with $I, J = 1, 2$. In this case, a state $|b\rangle$ with helicity λ will generate 2^{2N} states from creation and annihilation operators. One can construct the state $(Q^1_S)^\dagger|b\rangle$ with $\lambda + \frac{1}{2}$ and $(Q^1_S)^\dagger(Q^2_S)^\dagger|b\rangle$ with $\lambda + 1$.

However, CPT transformations impose that only $\lambda = -\frac{1}{2}$ may exist. Thus the spectrum is composed of one massless hypermultiplet

$$\lambda = (-\frac{1}{2}, 0, 0, \frac{1}{2}), \tag{A.32}$$

and two supermultiplets

$$\lambda = (0, \frac{1}{2}, \frac{1}{2}, 1) \tag{A.33}$$

$$\lambda = (-1, -\frac{1}{2}, -\frac{1}{2}, 0). \tag{A.34}$$

This gives the matter content of the extended N=2 SUSY. In chapter 2, we use this description to describe the UV completion of the F-SUSY scenario. In this case, the theory is derived from a supersymmetrical model in an extra dimension. The 5D matter content of the N=1 SUSY is equivalent to the one in the 4D N=2 model. Therefore, when describing the physics in the UV theory, we used the N=2 language.

B
Quantum Chromodynamics

Neutral naturalness (NN) models extend the SM with a copy of the strong sector. The new physics behaves like QCD, however they are not charged under the SM $SU(3)_C$. Chapter 3 shows the NN phenomenology of hidden glueballs from a Folded Supersymmetry scenario. The EW production of f-squarks in the LHC generates highly displaced vertices in the detector. We calculate the distribution of displaced vertices by modeling the Fragmentation Function (FF) of hidden gluons to glueballs.

The FF gives the hadronization of a parton to a hadron at a given energy. In QCD, FF are measured in a certain energy than evolved to higher energies in a DGLAP evolution. This process is usually described in the Mellin space. In this appendix, we show the Mellin transformation in the first section, then perform numerical calculations to evaluate the DGLAP evolution of gluons to glueballs FF.

B.0.1 Mellin Transform

Mellin transform's definition is given by:

$$F(x) = \int_0^\infty z^x f(z) \frac{dz}{z}, \tag{B.1}$$

denoting F(x) the Mellin transform of a function f(z), where x is a complex number (130).

The convolution of n functions in x space transforms in such a way

that the integrals become a product.

$$F(x) = \int f_1\left(\frac{z_1}{z_2}\right) f_2\left(\frac{z_2}{z_3}\right) \dots f_{n-1}\left(\frac{z_{n-1}}{z_n}\right) f_n(z_n) \frac{dz_1}{z_1}\frac{dz_2}{z_2}\dots\frac{dz_n}{z_n}, \tag{B.2}$$

so that we have

$$F(x) = F_1(x)F_2(x)\dots F_n(x). \tag{B.3}$$

The Mellin inverse transformation can be written as:

$$f(z) = \frac{1}{2i\pi}\int_C z^{-x}F(x)dx. \tag{B.4}$$

To proof the inversion form, we are going to find the relation between Mellin and Fourier transformation. Once this is done, it is straightforward to find Mellin's inverse. First, the relation between a Mellin and Laplace transformation is easily obtained through the variable change

$$z = e^{-u}, \;\; du = -e^{-u}dz, \tag{B.5}$$

such that

$$F(x) = \int_{-\infty}^{+\infty} f(e^{-u})e^{-ux}du. \tag{B.6}$$

Thus the Mellin transform described in equation (B.1) in terms of u and t variables is equivalent to a Laplace transformation of $f(e^{-u})$ with respect to x.

$$\text{Mellin}[f(z), x] = \text{Laplace}[f(e^{-u}), x]. \tag{B.7}$$

Also, taking another variable change $x = c + 2i\pi\beta$, one can find the relation between Mellin and Fourier transform.

$$F(x) = \int_{-\infty}^{+\infty} f(e^{-u})e^{-uc}e^{-2i\pi\beta u}du, \tag{B.8}$$

$$Mellin[f(z), x] = Fourrier[f(e^{-u}), \beta]. \tag{B.9}$$

It is clear that the inverse Fourrier transform of a funcion $\hat{\text{f}}(\beta)$ to $\tilde{\text{f}}(u)$ is given by:

$$\tilde{\text{f}}(u) = \int_{-\infty}^{+\infty} \hat{\text{f}}(\beta)e^{2i\pi\beta u}d\beta. \tag{B.10}$$

So the inversion of equation (B.8) from $f(z) = f(e^{-ut})$ to $F(x) = F(c + 2i\pi\beta$ will respect equation (B.10),

$$f(e^{-u})e^{-uc} = \int_{-\infty}^{+\infty} F(c + 2i\pi\beta)e^{2i\pi\beta u}d\beta. \tag{B.11}$$

Going back to the original x an z variables, since $x = c + 2i\pi\beta$ and $e^{-u} = z$,

$$f(z) = z^{-c}\int_{-\infty}^{+\infty} \hat{\mathrm{f}}(c + 2i\pi\beta)z^{2i\pi\beta}d\beta, \tag{B.12}$$

one can find Mellin's inversion formula by construction.

$$f(z) = \frac{1}{2i\pi}\int_{c-\infty}^{c+\infty} \hat{\mathrm{f}}(x)z^{-x}dx. \tag{B.13}$$

Thus the inversion formula can be interpreted as an integral in the contour C, with Re(x)=c, through all the imaginary line. This contour is represented in figure B.1, where the line R(s) lies on the right to the poles.

B.0.2 DGLAP evolution in x-space

The DGLAP evolution of a FF must be obtained by the differential equation in (3.23). The solution of this evolution is easily found in Mellin space, taking the transformation in equation (B.1) of the $D(z)$ into $D_x(x)$. The product between the splitting and FF on the right side of equation (3.23) is obtained by the convolution of two functions in terms of Mellin moments:

$$F(x) = \int_0^1 z^x f^{(1)}(z)f^{(2)}(x/z)\frac{dz}{z}. \tag{B.14}$$

Note that the definition of a Mellin transform the integration limit goes to infinity instead of 1. Since FF are similar to a probability, they are not defined for values greater than 1. So from now on all transforms are taken in this limit.

In terms of Mellin moments the differential equation becomes simply

$$\frac{\partial D_x(x,t)}{\partial t} = \frac{\alpha(t)}{2\pi}P(x)D_x(x,t), \tag{B.15}$$

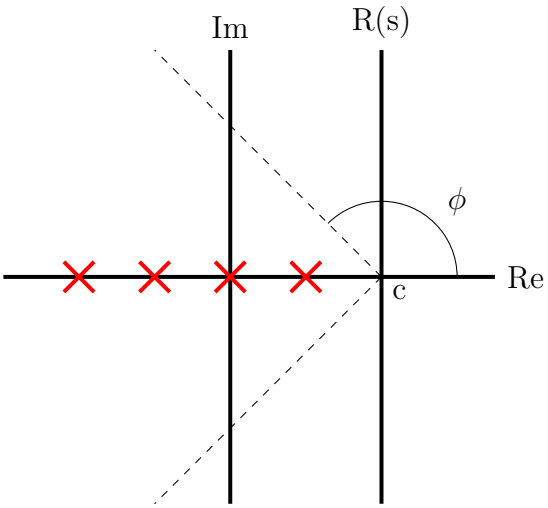

Figure B.1: Contour taken at R(s), with c lying on the right of the function poles.

with a solution:

$$D_x(x,t) = e^{P(x)\psi(t)} D_0(x), \tag{B.16}$$

where $D_0(x)$ is the Mellin transform of the FF at the initial energy scale. The function $\psi(t)$ represents the energy dependence in this evolution, it can be obtained replacing (B.16) into (B.15).

$$\psi(t) = \int \frac{\alpha(t)}{2\pi} dt. \tag{B.17}$$

Thus, we found the solution of an evolved FF in Mellin space, with the input function and calculating the dependence with the energy scale. The next step is to take the inversion formula (B.4):

$$D(z,\mu) = \frac{1}{2i\pi} \int_C D_x(x,\mu) z^{-x} dx, \tag{B.18}$$

where C is the contour chosen to be a vertical line in the complex plane R(s) = c, c a real number that lies in the right of all poles. This integral is then taken from $c - i\infty$ to $c + i\infty$. The constant c must be chosen such that the integral I below is convergent (131).

$$I = \int_0^1 dx x^{c-1} D_x(x) \tag{B.19}$$

Figure B.1 represents the contour taken in the inverse Mellin transform. The crosses are poles of the functions, so the contour R(s) lies on the right of all of them. From Cauchy's theorem, one may readjust

this contour by an angle ϕ as long as it is not too close to the divergencies, such as shown by the dashed line in the picture. Numerically, it should be interesting to choose an angle so the integral (B.18) converges faster. These calculations have been made numerically with the QCD-PEGASUS fortran package (132). In this work I have not used this package, but recalculated the inverse Mellin transform using this reference's parameters.

Bibliography

[1] M. Peskin and D. Schroeder, *An Introduction to Quantum Field Theory*Advanced book classics (Addison-Wesley Publishing Company, 1995).

[2] J. Donoghue, E. Golowich, and B. Holstein, *Dynamics of the Standard Model*Cambridge Monographs on Particle Physics, Nuclear Physics and Cosmology (Cambridge University Press, 1994).

[3] Particle Data Group, K. A. Olive *et al.*, Chin. Phys. **C38**, 090001 (2014).

[4] S. Glashow, Nucl.Phys. **22**, 579 (1961).

[5] S. Weinberg, Phys. Rev. Lett. **19**, 1264 (1967).

[6] Particle Data Group, M. Tanabashi *et al.*, Phys. Rev. D **98**, 030001 (2018).

[7] J. B. e. a. P. D. Group), Leptons, PR D86, 010001 (2012) and 2013 partial update for the 2014 edition.

[8] C. collaboration, Run 2 Summary plots – 13 TeV, `https://twiki.cern.ch/twiki/bin/view/CMSPublic/PhysicsResultsSUS#Run_2_Summary_plots_13_TeV_2016`, 2018, [Online; accessed 22-March-2019].

[9] G. Bertone, D. Hooper, and J. Silk, Phys. Rept. **405**, 279 (2005), hep-ph/0404175.

[10] T. Lin, (2019), 1904.07915.

[11] V. C. Rubin, W. K. Ford Jr, and N. Thonnard, The Astrophysical Journal **225**, L107 (1978).

[12] N. A. Bahcall, Proceedings of the National Academy of Sciences **114**, 2099 (2017).

[13] D. Clowe, A. Gonzalez, and M. Markevitch, The Astrophysical Journal **604**, 596–603 (2004).

[14] M. Markevitch *et al.*, Astrophys. J. **606**, 819 (2004), astro-ph/0309303.

[15] E. W. Kolb and M. S. Turner*The Early Universe* Vol. 69 (, 1990).

[16] Planck, N. Aghanim *et al.*, (2018), 1807.06209.

[17] S. Kumar, R. C. Nunes, and S. K. Yadav, Phys. Rev. **D98**, 043521 (2018), 1803.10229.

[18] C. Alcock *et al.*, The Astrophysical Journal **542**, 281–307 (2000).

[19] P. Tisserand *et al.*, Astronomy Astrophysics **469**, 387–404 (2007).

[20] L. Wyrzykowski *et al.*, Monthly Notices of the Royal Astronomical Society **416**, 2949 (2011), https://academic.oup.com/mnras/article-pdf/416/4/2949/2982628/mnras0416-2949.pdf.

[21] G. Burdman and G. Lichtenstein, JHEP **08**, 146 (2018), 1807.03801.

[22] D. A. Schwartz, Review of Scientific Instruments **85**, 061101 (2014).

[23] X.-N. C. S. T. with contributions from the entire XMM-Newton Science Operations Centre Team, Issue 2.16 (ESA: XMM-Newton SOC). (2018).

[24] SENSEI, J. Tiffenberg *et al.*, Phys. Rev. Lett. **119**, 131802 (2017), 1706.00028.

[25] G. L. Roni Harnik and Y. Zhang.

[26] G. Burdman, Z. Chacko, H.-S. Goh, and R. Harnik, JHEP **02**, 009 (2007), hep-ph/0609152.

[27] J. Scherk and J. H. Schwarz, Phys. Lett. **B82**, 60 (1979).

[28] J. Scherk and J. H. Schwarz, Nucl. Phys. **B153**, 61 (1979).

[29] M. J. Strassler and K. M. Zurek, Physics Letters B **651**, 374–379 (2007).

[30] Z. Chacko, H.-S. Goh, and R. Harnik, Phys. Rev. Lett. **96**, 231802 (2006), hep-ph/0506256.

[31] J. Terning, C. B. Verhaaren, and K. Zora, Physical Review D **99** (2019).

[32] I. García García, R. Lasenby, and J. March-Russell, Physical Review D **92** (2015).

[33] H.-C. Cheng, L. Li, and R. Zheng, Journal of High Energy Physics **2018** (2018).

[34] Z. Chacko, D. Curtin, M. Geller, and Y. Tsai, Journal of High Energy Physics **2018** (2018).

[35] R. Barbieri, L. J. Hall, and K. Harigaya, JHEP **11**, 172 (2016), 1609.05589.

[36] N. Craig, S. Knapen, and P. Longhi, Physical Review Letters **114** (2015).

[37] H. Cai, H.-C. Cheng, and J. Terning, Journal of High Energy Physics **2009**, 045–045 (2009).

[38] L.-X. Xu, J.-H. Yu, and S. hua Zhu, Minimal neutral naturalness model, 2018, 1810.01882.

[39] T. Cohen, N. Craig, G. F. Giudice, and M. Mccullough, JHEP **05**, 091 (2018), 1803.03647.

[40] L.-X. Xu, J.-H. Yu, and S. hua Zhu, Holographic completion of minimal neutral naturalness model and deconstruction, 2019, 1905.12796.

[41] Z. Chacko, M. A. Luty, and E. Pontón, Journal of High Energy Physics **2000**, 036–036 (2000).

[42] E. PONTÓN, The Dark Secrets of the Terascale , 283–374 (2013).

[43] T. Cohen, N. Craig, H. K. Lou, and D. Pinner, JHEP **03**, 196 (2016), 1508.05396.

[44] I. Antoniadis, S. Dimopoulos, A. Pomarol, and M. Quiros, Nucl. Phys. **B544**, 503 (1999), hep-ph/9810410.

[45] A. Delgado, A. Pomarol, and M. Quiros, Phys. Rev. **D60**, 095008 (1999), hep-ph/9812489.

[46] D. Curtin and C. B. Verhaaren, JHEP **12**, 072 (2015), 1506.06141.

[47] G. Burdman, Z. Chacko, H.-S. Goh, R. Harnik, and C. A. Krenke, Phys.Rev. **D78**, 075028 (2008), 0805.4667.

[48] J. Kang and M. A. Luty, Journal of High Energy Physics **2009**, 065–065 (2009).

[49] R. Harnik and T. Wizansky, Physical Review D **80** (2009).

[50] G. Aad *et al.*, Physics Letters B **738**, 428–447 (2014).

[51] G. Burdman, Z. Chacko, R. Harnik, L. de Lima, and C. B. Verhaaren, Phys. Rev. **D91**, 055007 (2015), 1411.3310.

[52] R. M. Capdevilla, R. Harnik, and A. Martin, (2019), 1912.08234.

[53] J. Juknevich, D. Melnikov, and M. Strassler, Journal of High Energy Physics **2009**, 055–055 (2009).

[54] N. Craig, A. Katz, M. Strassler, and R. Sundrum, JHEP **07**, 105 (2015), 1501.05310.

[55] D. Carmi, A. Falkowski, E. Kuflik, and T. Volansky, Journal of High Energy Physics **2012** (2012).

[56] H. B. Meyer, Journal of High Energy Physics **2009**, 071–071 (2009).

[57] G. Burdman, N. Fonseca, and G. Lichtenstein, Phys. Rev. **D88**, 116006 (2013), 1308.5988.

[58] Y. Chen *et al.*, Physical Review D **73** (2006).

[59] H. Georgi and Y. Nakai, Physical Review D **94** (2016).

[60] V. Barger and R. Phillips, *Collider Physics*Advanced book program (Addison-Wesley Publishing Company, 1997).

[61] O. Biebel, D. de Florian, D. Milstead, and A. Vogt, 17. FRAGMENTATION FUNCTIONS IN e+e−, ep AND pp COLLISIONS.

[62] G. Altarelli and G. Parisi, Nuclear Physics B **126**, 298 (1977).

[63] A. Larkoski, S. Marzani, J. Thaler, A. Tripathee, and W. Xue, Physical Review Letters **119** (2017).

[64] R. K. Ellis, W. J. Stirling, and B. R. Webber, Camb. Monogr. Part. Phys. Nucl. Phys. Cosmol. **8**, 1 (1996).

[65] S. Albino, Rev. Mod. Phys. **82**, 2489 (2010), 0810.4255.

[66] M. Ciafaloni, D. Colferai, G. P. Salam, and A. M. Stasto, Phys. Lett. **B587**, 87 (2004), hep-ph/0311325.

[67] P. Roy and K. Sridhar, JHEP **07**, 013 (1999), hep-ph/9902400.

[68] P. Chiappetta, M. Greco, J. P. Guillet, S. Rolli, and M. Werlen, Nucl. Phys. **B412**, 3 (1994), hep-ph/9301254.

[69] J. Alimena *et al.*, Searching for long-lived particles beyond the standard model at the large hadron collider, 2019, 1903.04497.

[70] M. Aaboud *et al.*, The European Physical Journal C **79** (2019).

[71] G. Aad *et al.*, Physical Review D **92** (2015).

[72] G. Aad *et al.*, Physics Letters B **743**, 15–34 (2015).

[73] M. Aaboud *et al.*, Physical Review D **97** (2018).

[74] G. Aad *et al.*, Physical Review D **92** (2015).

[75] A. Sirunyan *et al.*, Physics Letters B **780**, 432–454 (2018).

[76] A. Sirunyan *et al.*, Physical Review D **99** (2019).

[77] V. Khachatryan *et al.*, Physical Review D **91** (2015).

[78] A. Sirunyan *et al.*, Physical Review D **98** (2018).

[79] R. Aaij *et al.*, The European Physical Journal C **77** (2017).

[80] R. Aaij *et al.*, The European Physical Journal C **76** (2016).

[81] C. Damerell, Nuclear Instruments and Methods in Physics Research Section A: Accelerators, Spectrometers, Detectors and Associated Equipment **226**, 26 (1984).

[82] G. F. Amelio, M. F. Tompsett, and G. E. Smith, Bell System Technical Journal **49**, 593 (1970), https://onlinelibrary.wiley.com/doi/pdf/10.1002/j.1538-7305.1970.tb01791.x.

[83] W. S. Boyle and G. E. Smith, Bell System Technical Journal **49**, 587 (1970), https://onlinelibrary.wiley.com/doi/pdf/10.1002/j.1538-7305.1970.tb01790.x.

[84] J. R. Janesick*Scientific charge-coupled devices* Vol. 83 (SPIE press, 2001).

[85] K. P. Singh, Resonance **10**, 8 (2005).

[86] M. C. I. T. Chandra X-ray Center Chandra Project Science, The Chandra Proposers' Observatory Guide , in *The Chandra Proposers' Observatory Guide* , 2019.

[87] J. R. Janesick *et al.*, New advancements in charge-coupled device technology: subelectron noise and 4096 x 4096 pixel CCDs, in *Charge-Coupled Devices and Solid State Optical Sensors*, edited by M. M. Blouke Vol. 1242, pp. 223 – 237, International Society for Optics and Photonics, SPIE, 1990.

[88] C. E. Chandler, R. A. Bredthauer, J. R. Janesick, and J. A. Westphal, Sub-electron noise charge-coupled devices, in *Charge-Coupled Devices and Solid State Optical Sensors*, edited by M. M. Blouke Vol. 1242, pp. 238 – 251, International Society for Optics and Photonics, SPIE, 1990.

[89] G. Fernández Moroni *et al.*, Experimental Astronomy **34**, 43–64 (2012).

[90] SENSEI, O. Abramoff *et al.*, Phys. Rev. Lett. **122**, 161801 (2019), 1901.10478.

[91] L. Strüder *et al.*, **365**, L18 (2001).

[92] Turner, M. J. L. *et al.*, A&A **365**, L27 (2001).

[93] R. L. Kelley *et al.*, Publications of the Astronomical Society of Japan **59**, S77 (2007).

[94] D. N. Burrows *et al.*, Space Sci. Rev. **120**, 165 (2005), astro-ph/0508071.

[95] T. Takahashi, K. Mitsuda, and R. K. et al., The ASTRO-H X-ray astronomy satellite, in *Space Telescopes and Instrumentation 2014: Ultraviolet to Gamma Ray*, edited by T. Takahashi, J.-W. A. den Herder, and M. Bautz Vol. 9144, pp. 640 – 663, International Society for Optics and Photonics, SPIE, 2014.

[96] T. R. Slatyer, Tasi lectures on indirect detection of dark matter, 2017, 1710.05137.

[97] E. Bulbul *et al.*, The Astrophysical Journal **789**, 13 (2014).

[98] A. Boyarsky, O. Ruchayskiy, D. Iakubovskyi, and J. Franse, Physical Review Letters **113** (2014).

[99] T. Jeltema and S. Profumo, Monthly Notices of the Royal Astronomical Society **450**, 2143–2152 (2015).

[100] S. Dodelson and L. M. Widrow, Physical Review Letters **72**, 17–20 (1994).

[101] A. Dighe, S. Pastor, and A. Smirnov, The physics of relic neutrinos, 1998, hep-ph/9812244.

[102] A. Merle and A. Schneider, Physics Letters B **749**, 283–288 (2015).

[103] F. A. Aharonian *et al.*, The Astrophysical Journal **837**, L15 (2017).

[104] S. Profumo and K. Sigurdson, Phys. Rev. **D75**, 023521 (2007), astro-ph/0611129.

[105] D. J. Marsh, Physics Reports **643**, 1–79 (2016).

[106] R. Yamamoto, N. Y. Yamasaki, K. Mitsuda, and M. Takada, A search for a contribution from axion-like particles to the x-ray diffuse background utilizing the earth's magnetic field, 2019, 1906.04429.

[107] D. Curtin and J. Setford, (2019), 1909.04071.

[108] D. Curtin and J. Setford, (2019), 1909.04072.

[109] XQC, E. Figueroa-Feliciano *et al.*, Astrophys. J. **814**, 82 (2015), 1506.05519.

[110] P. B. Pal and L. Wolfenstein, Phys. Rev. **D25**, 766 (1982).

[111] J. F. Navarro, C. S. Frenk, and S. D. M. White, Astrophys. J. **462**, 563 (1996), astro-ph/9508025.

[112] L. Pieri, J. Lavalle, G. Bertone, and E. Branchini, Phys. Rev. **D83**, 023518 (2011), 0908.0195.

[113] L. Rinchiuso *et al.*, Phys. Rev. **D98**, 123014 (2018), 1808.04388.

[114] H. Uchiyama, M. Nobukawa, T. Go tsuru, and K. koyama, Publications of the Astronomical Society of Japan **65**, 19 (2013).

[115] A. Kushino *et al.*, Publ. Astron. Soc. Jap. **54**, 327 (2002), astro-ph/0204224.

[116] B. Feldstein, P. W. Graham, and S. Rajendran, Phys. Rev. **D82**, 075019 (2010), 1008.1988.

[117] J. Eby, P. J. Fox, R. Harnik, and G. D. Kribs, (2019), 1904.09994.

[118] M. Viel, J. Lesgourgues, M. G. Haehnelt, S. Matarrese, and A. Riotto, Physical Review Letters **97** (2006).

[119] S. Davidson, B. Campbell, and D. Bailey, Phys. Rev. D **43**, 2314 (1991).

[120] G. Raffelt, *Stars as Laboratories for Fundamental Physics: The Astrophysics of Neutrinos, Axions, and Other Weakly Interacting Particles*Theoretical Astrophysics (University of Chicago Press, 1996).

[121] G. D. Kribs, T. S. Roy, J. Terning, and K. M. Zurek, Physical Review D **81** (2010).

[122] G. Battaglia *et al.*, Monthly Notices of the Royal Astronomical Society **364**, 433–442 (2005).

[123] C. McCabe, JCAP **1402**, 027 (2014), 1312.1355.

[124] D. Curtin *et al.*, Reports on Progress in Physics **82**, 116201 (2019).

[125] M. L. Mangano, Proceedings of Theoretical Advanced Study Institute Summer School 2018 "Theory in an Era of Data" — PoS(TASI2018) (2019).

[126] G. L. Gustavo Burdman.

[127] S. P. Martin, FERMILAB-PUB (1997), hep-ph/9709356, [Adv. Ser. Direct. High Energy Phys.18,1(1998)].

[128] J. Terning, *Modern Supersymmetry: Dynamics and Duality*International Series of Monogr (OUP Oxford, 2006).

[129] M. Shifman, *Advanced Topics in Quantum Field Theory: A Lecture Course* (Cambridge University Press, 2012).

[130] A. Poularikas, *The Transforms and Applications Handbook*Electrical Engineering Handbook (CRC-Press, 2000).

[131] R. Courant and D. Hilbert, *Methods of Mathematical Physics*, Wiley classics library No. v. 1 (Interscience, 1966).

[132] A. Vogt, Comput. Phys. Commun. **170**, 65 (2005), hep-ph/0408244.